UNIVERSITA' DEGLI STUDI DI MODENA E REGGIO EMILIA
DIPARTIMENTO DI INGEGNERIA 'ENZO FERRARI'

PhD SCHOOL

INDUSTRIAL AND ENVIROMENTAL ENGINEERING
INGEGNERIA INDUSTRIALE E DEL TERRITORIO

XXXIV CYCLE

APPLICATION OF MODELLING TECHNIQUES FOR THE VIRTUAL DEVELOPMENT OF HIGH PERFORMANCE TAILORED HYBRID SYSTEMS AND THEIR COMPONENTS

Advisors:
Prof. Stefano Fontanesi
Dr. Alessandro d'Adamo

Candidate:
Francesco Pulvirenti

PhD School Director:
Prof. Alberto Muscio

Ad Alice, Daniela e Giulio

Abstract

Despite the increasingly stringent legislations, hybrid powertrains will retain a relevant market share in the upcoming years, thus the optimization of their powertrain systems will be of paramount importance. In this context, modelling techniques for the virtual development of high performance hybrid systems is crucial in order to achieve the best trade-off between reducing tailpipe emissions and reaching best in class levels of vehicle performance.

In HEVs, the presence of different energy sources increases powertrain complexity. At each time instant, the choice of the power-split depends on the objective of the hybridization. The design of this powertrain control strategy represents a typical optimal control problem. The first part of the research focused on the development, of a methodology based on optimal control theory to maximize fuel economy and minimize lap time in sport driving conditions. The analysis considered a P1-P4 HEV as a test case. Dynamic Programming (DP) is used to assess the maximum powertrain capabilities relying on simplified vehicle models. The information collected from the DP, in both scenarios, is used to create policy maps depending on the main states of the powertrain, which are given as inputs to high fidelity models (plant model) used for the final assessment of the proposed control strategy. Therefore, the results can be used as a benchmark for developing real-time implementable control strategies: possibility to learn from the optimal solution. In addition, such a benchmark enables a fair comparison among different component variants, which are of paramount importance during the vehicle concept phase, because it will help to correctly assign their specifications (i.e. power, battery size, gear ratio etc.).

A second topic involves the after-treatment operation at engine cold start. This is a key area for achieving a significant reduction in tailpipe emissions. In fact, a typical three-way catalyst (TWC) loses its effectiveness below a brick temperature of roughly 500-600 K, nearly nullifying pollutant conversion at the cold start. In order to properly simulate these aspects and investigate new possible solutions, a brand new 3D CFD methodology has been developed in the Open FOAM framework. It includes the whole exhaust system until the first TWC brick, complex multi-physics, mass/heat transfer, chemical reactions and flow through porous media. The study focuses on the light-off process, enabling optimization of new hardware; the burner showed a good potential combined with a pre-heating strategy in order to have enough TWC temperature, thus efficiency for pollutant conversion, before the engine start.

A third topic moves inside the engine heart, to the understanding of pollutant formation, both particulate and gaseous emissions, by means of 3D CFD in-cylinder simulations. From a numerical standpoint, a simplified approach is dedicated to gaseous emissions, while a more detailed and customized one is reserved for soot modeling. The present study is a novelty in providing guidelines for a fair comparison between the experimental and the numerical dataset, via a dedicated post-processing of the simulation outcomes. This enables design of new parts and new combustion chambers layouts, leading to less emissions at the end of the combustion process.

Lastly, the engine oil tank is investigated with a new 3D CFD approach based on Eulerian Multi-Phase (EMP). Its advantage is that it accounts for the interaction between liquid and gaseous phases, modeling mist and foam formation and its subsequent separation. From the emissions point of view, the correct prediction of these phenomena is crucial for the HC and soot emissions contribution due to blow-by recirculation.

This dissertation presents therefore several virtual design methodologies aimed at reaching the above-mentioned goal: designing the best sport car by optimizing its components as part of a holistic system (Fig.1).

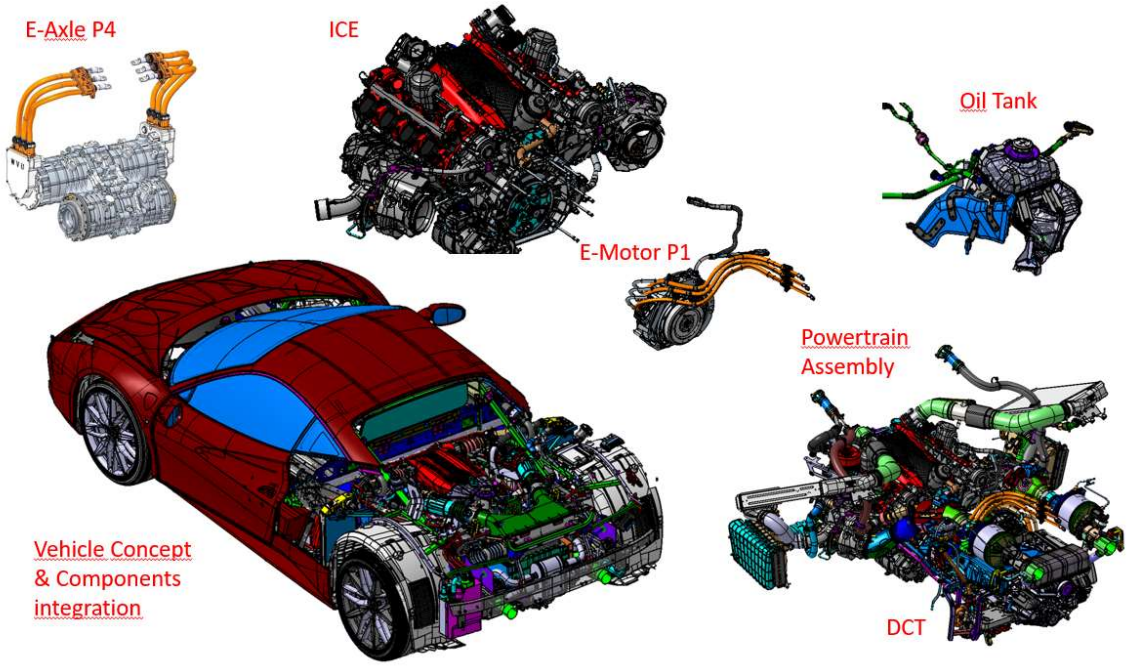

Fig.1: Powertrain components as part of a holistic system

Nonostante le crescenti limitazioni normative, nei prossimi anni i propulsori ibridi manterranno una quota di mercato rilevante. L'ottimizzazione dei loro sottosistemi appare quindi fondamentale. In questo contesto, tecniche di modellazione virtuale di sistemi ibridi permettono di ottenere il miglior compromesso tra la riduzione delle emissioni dallo scarico ed il raggiungimento dei target prestazionali veicolo.

Nei veicoli ibridi (HEVs), la presenza di diverse sorgenti di energia aumenta la complessità del gruppo propulsore: la scelta ottimale della suddivisione di potenza dipende dall'obiettivo dell'ibridizzazione. La progettazione di una strategia di controllo del gruppo propulsore rappresenta dunque un tipico problema di controllo ottimale.

La prima parte della ricerca riguarda lo sviluppo di una metodologia basata sulla teoria del controllo ottimale per minimizzare consumo e tempo sul giro in condizioni di guida sportiva. L'analisi considera un P1-P4 HEV come architettura di riferimento. La Programmazione Dinamica (DP) viene utilizzata per valutare le capacità massime del powertrain basandosi su modelli di veicoli semplificati. Le informazioni raccolte dalla DP, in entrambi gli obiettivi, vengono utilizzate per creare le mappe a seconda dei principali

stati del powertrain, che vengono fornite come input a modelli più dettagliati per la valutazione finale della strategia di controllo proposta. I risultati possono fungere da riferimento per lo sviluppo di strategie di controllo implementabili in tempo reale, nonché consentire un confronto equo tra diverse varianti di componenti e architetture, utile nella fase di impostazione veicolo.

Il secondo tema di ricerca riguarda lo studio del sistema di post-trattamento nella fase di avviamento a freddo del motore, che rappresenta un'area chiave per ottenere una significativa riduzione delle emissioni dallo scarico. Infatti, un tipico catalizzatore a tre vie (TWC) perde la sua efficacia al di sotto di una temperatura delle matrici di circa 500-600 K, inficiando la conversione degli inquinanti all'avvio a freddo. Al fine di simulare correttamente questi aspetti e studiare nuove possibili soluzioni, è stata sviluppata una metodologia CFD 3D in Open FOAM che comprende l'intero sistema di scarico fino al primo brick del TWC e modelli multi-fisici complessi. Lo studio si concentra sull'utilizzo di un burner che, combinato con una strategia di preriscaldamento, mira a raggiungere una temperatura TWC sufficiente per innescare in maniera efficace la conversione.

Il terzo tema di ricerca trattato si focalizza sul processo di combustione per la comprensione della formazione di inquinanti, sia di particolato che di emissioni gassose mediante simulazioni 3D CFD interno cilindro. Un approccio semplificato è stato dedicato alle emissioni gassose, mentre uno più dettagliato è riservato alla modellazione del particolato.

La metodologia sviluppata ha permesso un equo confronto tra il set di dati sperimentale e numerico, fornendo linee guida progettuali per il design dei componenti al fine di minimizzare le emissioni.

L'ultimo tema di ricerca riguarda il serbatoio dell'olio motore che viene studiato con un nuovo approccio CFD basato su Eulerian Multi-Phase (EMP), che tiene conto dell'interazione tra fasi liquide e gassose, modellando la formazione di nebbia e schiuma e la successiva separazione. Dal punto di vista delle emissioni, la corretta previsione di questi fenomeni è cruciale per il contributo delle emissioni di HC e particolato dovuto al ricircolo blow-by.

Questa tesi presenta dunque diverse metodologie di analisi virtuale volte a raggiungere l'obiettivo sopra menzionato: progettare la migliore auto sportiva ottimizzando i suoi componenti come parte di un sistema olistico (Fig.1).

Table of Contents

Chapter 3

Modeling soot and gaseous emissions in 3D-CFD in-cylinder simulations of spark-ignition engines: a methodology to correlate numerical results and experimental data

Chapter 4

A new methodology development to assess oil tank sloshing of a High-Performance Car under racetrack maneuvers

Final Remarks

References

General Introduction and Motivations

At the present time there is no doubt - the current emissions legislations for the automotive sector are going towards a more restrictive worldwide scenario, with a further limitation of the admitted pollutant and greenhouse emissions. An official proposal for future European emissions legislation is expected in early 2022. This is known as "Euro 7''. It is anticipated to feature drastically reduced limits and this is particularly challenging for high performance vehicles.

Despite the growing BEV (Battery Electric Vehicle) market, in 2030, hybrid powertrains are foreseen to have the highest market share (Fig.2). This means optimizing the powertrain system is still of paramount importance to succeed.

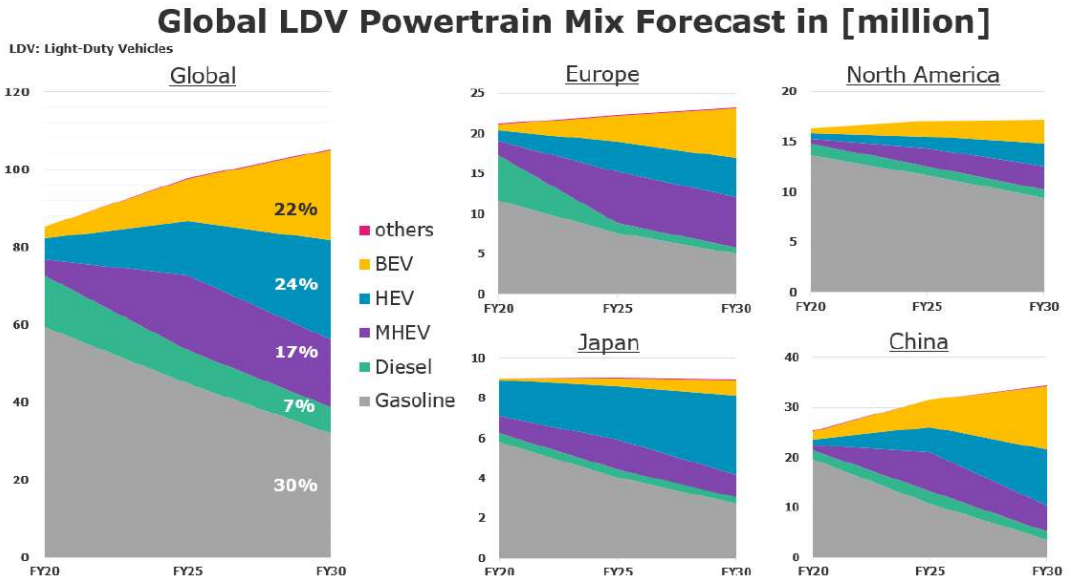

Fig.2: Predicted evolution of market share of various powertrain types [42nd Intern. Vienna Motor Symposium, Denso's Paper]. HEV = Hybrid Electric Vehicle, MHEV= Mild Hybrid Electric Vehicle

The primary development objective of Ferrari's road cars is to be fast and fun to drive. These are fundamental values of Ferrari's DNA. In terms of powertrain objectives these translate to fast transient response and high power output. There are also strong links between the powertrain concept and outstanding vehicle dynamics; this is both because the powertrain concept and control link to the vehicle performance in terms of high acceleration capability (power-split between the front and rear axle) and a robust powertrain lubrication system design (max acceleration allowable). The main objectives of the powertrain optimization are depicted in Fig.3.

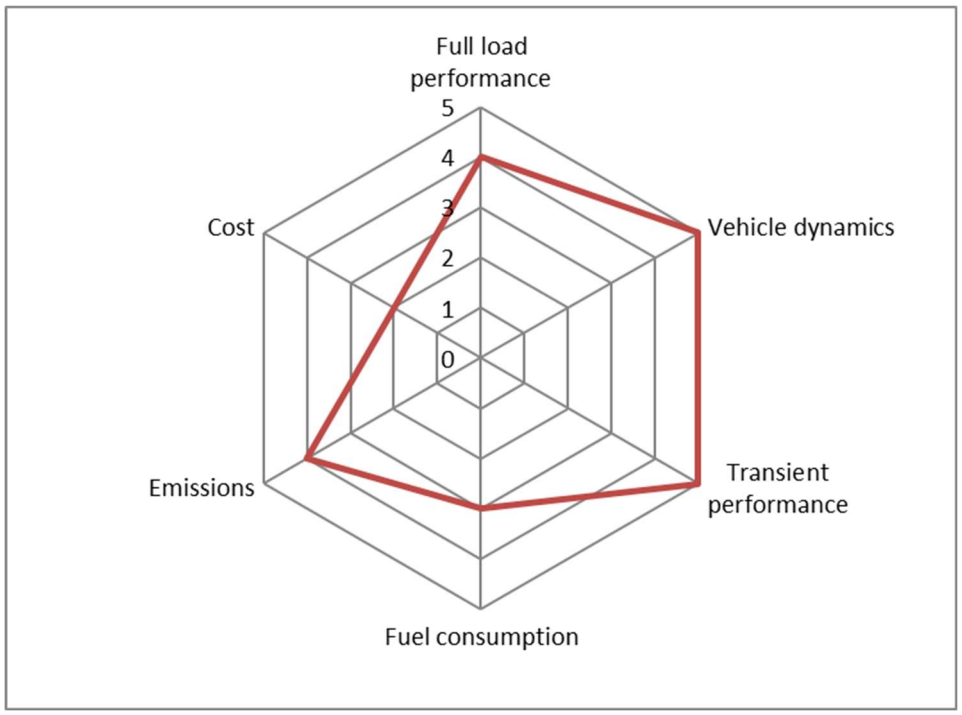

Fig.3: Vehicle and Powertrain objectives

Ferrari is famous for its luxury sports cars and in 2019 announced the SF90 Stradale road car, as shown in Fig.4, which is its first Plug-in Hybrid Electric Vehicle (PHEV), featuring a combined power output of 1000 CV from a 780CV V8 Internal Combustion Engine (ICE) of 3990 CC swept volume and three electric motors.

Fig.4: SF90 Stradale

This car, with its complex P1- P4 architecture, is an optimal example of integration where the main challenge, as can be imagined, was to find the best trade-off between size, weight, performance of the powertrain components and their integration with chassis, whilst always guaranteeing emissions compliance.

In this context, the key role of virtual analysis to address the design decisions becomes very clear, since the vehicle concept phase is a fundamental part of the product development process.

Furthermore, virtual simulations are also a very important enabler of cost and development time reductions, which can be estimated as around 30% (Source: Simulia from an OEM survey).

The author has been responsible for Ferrari's Simulation & Know How Powertrain Department since 2012, In this period it has become increasingly clear the great importance of investing in simulation methodology development. This enables key benefits such as wider examination of possible design options, multi-physics optimization and better understanding of complex interlinked phenomena during problem solving activities.

For all the reasons listed above, this thesis represents a significant contribution because the methodologies developed on seemingly disparate topics (optimization of powertrain architectures, emission reduction and oil tank sloshing), are actually correlated by the fact that together they constitute a fundamental support when starting from a blank sheet of paper and needing to fight millimeter after millimeter to design the components that lead to an optimum overall car design.

This is the common thread with which to read the various chapters of this work, each of which has a dedicated introduction in order to better frame the theme from a methodological point of view and its challenge.

The first chapter concerns the development of a model for the optimization of the vehicle architecture and its power sources. The application of dynamic programming techniques (DP) is proposed for the definition of the best solutions that allow to achieve the double objective: minimization of lap time for a given track and minimization of fuel consumption for a regulated cycle such as the WLTC (Worldwide Harmonized Light Duty Test Cycle). The study uses as a reference model an architecture similar to that described for the SF 90 Stradale car, with a rear-mounted turbo V8 engine assembled with a P1 type electric motor and a P4 type electric front axle.

The second chapter regards a virtual assessment of an After-Treatment-System (ATS) equipped with a burner to speed up the light-off of the catalyst during engine cold start. The study focuses on the after-treatment system of a high-performance SI (Spark Ignition) gasoline V12 naturally aspirated engine, in order to investigate the behavior of the system during the cold start phase. This engine architecture was simulated for alignment with the experimental program. As the investigation was principally on the after treatment system and not the engine itself, the proposed methodology is generally applicable also to turbocharged engines, such as those used in the other chapters of this thesis.

The third chapter moves to a novel approach for modeling soot and gaseous emissions in 3D-CFD in-cylinder simulations of spark-ignition engines. Here an extensive comparison between numerical results and experimental data was performed. The engine under study was a V8 turbocharged engine with a multi-purpose fully instrumented exhaust manifold in order to record all the engine out relevant emissions in multiple locations. Among the engine experimental data, a subset describing a SOI (Start Of Injection) variation was chosen as the validation case for the CFD results. The core activity is twofold:

firstly a modeling methodology was developed for soot and gaseous emissions, secondly a relevant effort was made because a comparison against experiments is not straightforward. In fact, complex methods and instruments are usually adopted, whose characteristic outputs are sometimes far from typical simulations results. In other words, an ad-hoc post-processing of simulation outcomes was needed to make them comparable to experiments.

In the last chapter the author proposes a new methodology to assess oil tank sloshing of a high-performance car under racetrack maneuvers. The oil tank is not a trivial component as might be initially assumed. This is because multiple functions have to be addressed both from a vehicle and engine point of view. From a vehicle standpoint, oil tank weight (including oil and tank body mass) and its shape, have a direct impact on the car body dimensions and thus vehicle performance.

From the engine point of view, an oil tank mission is to separate as much as possible the engine oil from the blow-by air, thus minimizing oil entry to the engine intake line. The separation task is even harder to achieve during the transient high acceleration maneuvers under which the oil tank is subject to in racetrack conditions. Once the oil enters in the intake line, it is well known its connection to HC (Hydro Carbon) emission release, due to the oil burning in the combustion chamber. This condition is detrimental for a modern engine, especially looking at the stricter emission regulations they are going to face in the near future time. The adoption of a model able to handle the separation between the phases, as well as possible foam formation, is of paramount importance. Besides the common Volume of Fluid method (VoF), which is not able to catch foam formation, a novel Eulerian Multi-Phase approach (EMP) has been developed and validated against a literature test case and overall experimental oil tank behavior observed during static and dynamic vehicle maneuver.

As a final remark, it is hoped that the disparate themes and methodologies presented give some idea of the real complexities of modern powertrain design and development and the many diverse challenges faced by a modern automotive company.

Chapter 1

Development of a model for the optimization of the vehicle architecture and its power sources

1.1 Introduction

Nowadays powertrain electrification represents one of the most promising solutions to reduce the carbon footprint of conventional vehicles and to move towards a more sustainable mobility. Focusing on high specific power engines, for which the technology innovation process is mainly driven by performance enhancement, an increasing level of electrification may allow the simultaneous achievements of the future targets on CO2 emissions and of a best-in-class fun-to-drive. As a matter of fact, during abrupt accelerations the electric machines can be used to support the engine, which on the contrary can be designed for the maximum power. Moreover, the presence of this energy reservoir may also enable the integration of new technologies such as, advanced turbocharging systems or electrically heated catalysts.

The coexistence of different energy paths generates a significant increase of the powertrain complexity that should be tackled not only during the design process but also during vehicle operation. Indeed, at each instant of time, the power needed by the vehicle for its motion can be provided by either one of the power actuators or by a combination of the two. The choice from among all the available power splits depends on the actual objective of the hybridization. This task is typically addressed by the so-called Energy Management System (EMS), which represents an additional control layer between the driver requests and the low-level controllers. The optimal design of this powertrain control strategy is crucial to maximize the hybridization potential and it represents a typical optimal control problem. Several methodologies are available in the scientific literature, which may differ in optimality, computational requirements and robustness. It is possible to identify three main categories:

- Global optimization strategies, in which the dynamic nature of the system is considered for optimization, and an optimal solution is found over a predefined driving cycle, that must be known “a priori”. For this reason, and for the high computational effort requested, this methodology can be used for benchmarking and could have the maximum effect if applied during the concept design phase of the vehicle, because it helps to address the choice in terms of powertrain layout and specifications. (Bianchi et al., 2010).
- Static optimization strategies, in which the problem of the energy management optimization is translated into the instantaneous minimization of a pre-defined cost function, taking into account both the engine fuel consumption and the use of the

electrical energy stored into the battery that is converted into an equivalent fuel consumption.

- Heuristic strategies, which are based on a set of rules, aiming to keep the internal combustion engine operating conditions within the region with highest efficiencies. These are the most common strategies since, thanks to their low computational requirements, they can be easily implemented in an engine control unit (ECU).

In this thesis work, the research focused on the development of a methodology based on optimal control theory to maximize fuel economy and minimize lap time in sport driving conditions. The analysis considered a rear-mounted turbo V8 engine assembled with a P1 type electric motor and a P4 type electric front axle as a test case. The Dynamic Programming (DP) method is used to assess the maximum powertrain capabilities relying on simplified vehicle models, called the *DP model,* which was implemented in the Python enviroment. The information collected from the DP, in both scenarios, is used to create policy maps depending on the main states of the powertrain, which are given as inputs to high fidelity models, called the *plant model,* which was implemented in the Amesim platform licensed by Siemens, used for the final assessment of the proposed control strategy. Optimal control (OC) was made in two steps as depicted in Fig.5.

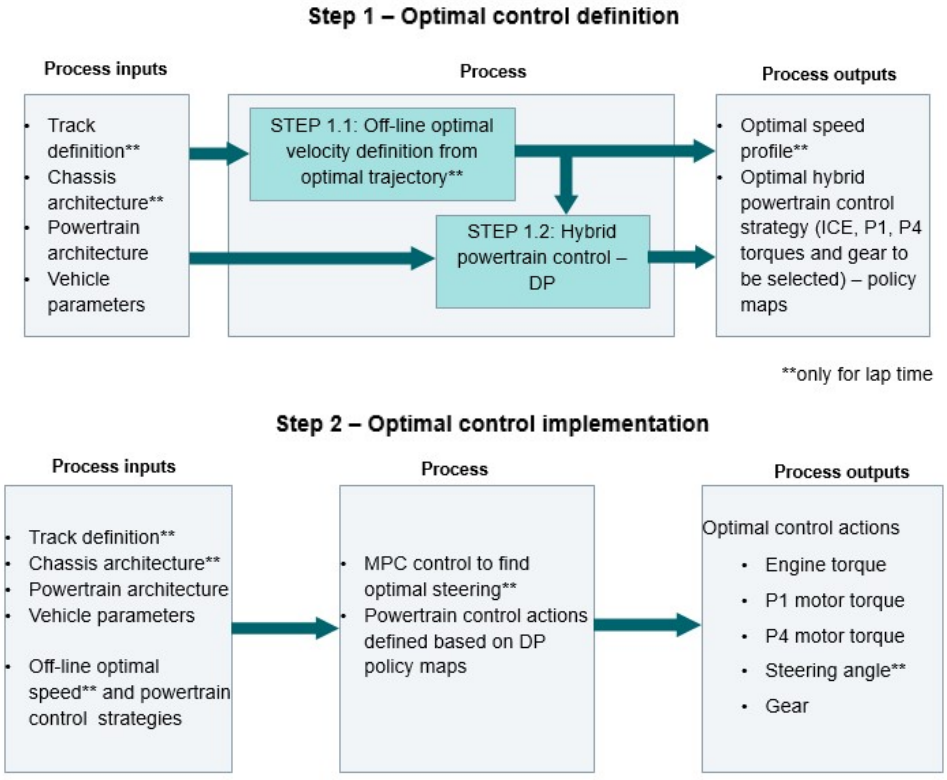

Fig.5: Optimal control workflow

Both models have been used to know how the powertrain will be used in the optimal way during different vehicle missions like charge depleting, charge sustaining and lap time optimization. Therefore, the results can be used as a benchmark for developing real-time

implementable control strategies with the possibility to learn from the optimal solution. In addition, such a benchmark enables a fair comparison among different component variants.

1.2 Dynamic programming background

Dynamic programming (DP) [1], [2], [3], [4] is a numerical method to solve problems in which a sequence of interrelated decisions have to be taken [5].

DP is the only optimal control method capable of providing the optimal solution to problems of any complexity level within the accuracy limitations imposed by the discretization of problem variables [6], e.g., controls and states. The DP algorithm is able to handle both continuous and discrete variables, making it suitable for a vast variety of control problems.

In order to solve a control problem through DP, it is necessary to define:

- Performance index
- State dynamics
- Set of admissible states
- Global (final) state constrains
- Initial states
- Set of admissible controls

The discretized performance index for the optimal control problem starting at the initial state x_0:

$$\Psi_{0,\mathrm{N}} = \mathrm{L_N}(\mathrm{x_N}) + \sum_{\mathrm{k=1}}^{\mathrm{N-1}} \mathrm{L_k}(\mathrm{x_k}, \mathrm{u_k}) \qquad (1)$$

where,

k indicates the computation step k.

N indicates the final step.

x_k are the state variables.

u_k are the control variables.

L_k is the instantaneous cost function. Hence, $L_N(x_N)$ is the terminal cost which depends on the final state.

A discretized version of the state dynamics (embedded model of the system):

$$\mathrm{x_{k+1}} = \mathrm{x_k} + \mathrm{f_k}(\mathrm{x_k}, \mathrm{u_k}) \qquad (2)$$

with,

$$x_k \in X_k \quad (3)$$

$$u_k \in U_k \quad (0)$$

where X_k and U_k indicate the set of admissible states and controls at each step.

The global (final) state constraints are conditions that the final value of state variables should satisfy. A state variable should reach a predefined value $x_{req,N}$ at the final step. This can be enforced as a hard constraint $x_N = x_{req,N}$ or as a soft constraint introducing a penalty function into the performance index, which is usually a function of the difference $x_N - x_{req,N}$.

The method of DP is based on Bellman's principle of optimality [2]. According to this intuitively appealing concept:

> An optimal policy has the property that whatever the initial state and initial decision are, the remaining decisions must constitute an optimal policy with regard to the state resulting from the first decision.

This implies that from any step on a discretized optimal trajectory, the remaining trajectory is optimal for the corresponding problem initiated at that step (and corresponding system states) [1], [6]. The analytical proof, which is based on the induction principal, can be found in [5].

When implementing DP, the optimal solution is found proceeding backwards, i.e.: starting from the final step, the sequence of controls, which minimizes the sum of the costs from the current state to the end of the optimization horizon, is found at each step [7]. Note that the above statement implies that in order to select the first control action, the backward solution of the entire problem needs to be found [8], making DP a non-causal optimal control technique.

One of the main practical limitations to the implementation of DP is the computational burden involved, which increases linearly with the final time and exponentially with the dimension of the state vector. This is referred to in literature as the 'curse of dimensionality' [7].

1.2.1 Application of DP to the Energy Management Problem in HEV

In the context of Hybrid Electric Vehicles (HEVs), DP is a non-causal Energy Management Strategy (EMS), meaning that in order to find the optimal controls trajectory, the entire driving cycle must be known a priori.

Despite not being real-time implementable, DP yields the best available approximation of the optimal control policy for a certain HEV allowing to determine its maximum capabilities. Hence, the results obtained can be useful for:

- Optimizing the design of HEVs [9], [10].
- Designing of rule-based EMSs [11], [12].
- Generating benchmark solutions for real-time implementable EMSs [13-17].

In order to show how the principle of optimality can be used to determine the solution to an optimal control problem, an example is presented here (see [6] for more details). This will allow to illustrate the implementation of DP.

In practical terms, any DP problem requires 3 steps to be solved:

- Step 1: Compute arc costs.
- Step 2: Minimize cost-to-go.
- Step 3: Compute the optimal path.

Consider the following simplified HEV control problem:

- State variables and constraints: SOC is the only state variable and the set of admissible values at each step is discretized as $X = [0.6, 0.65, 0.7]$.
- Global state constraint: $x_N = 0.65$.
- Initial state: $x_0 = 0.65$.
- Control variables and constraints: Battery power is the only control variable, for simplicity, it is expressed in terms of SOC variation. Hence, the set of admissible values at each step is discretized as $U = [-0.1, -0.05, 0, +0.05, +0.1]$.
- State dynamics: As stated above, controls are given in terms of SOC variation, therefore $x_{k+1} = x_k + u_k$.
- Performance index: For simplicity, the arc cost $L_k(x_k, u_k)$ is already provided in Fig.1.

Step 1: Compute Arc costs

In the context of DP, the arc cost is the instantaneous cost incurred during a single computation step in choosing a certain control action. It must be calculated for all admissible states at each step, it is represented by the numbers in the arrows of Fig.6.

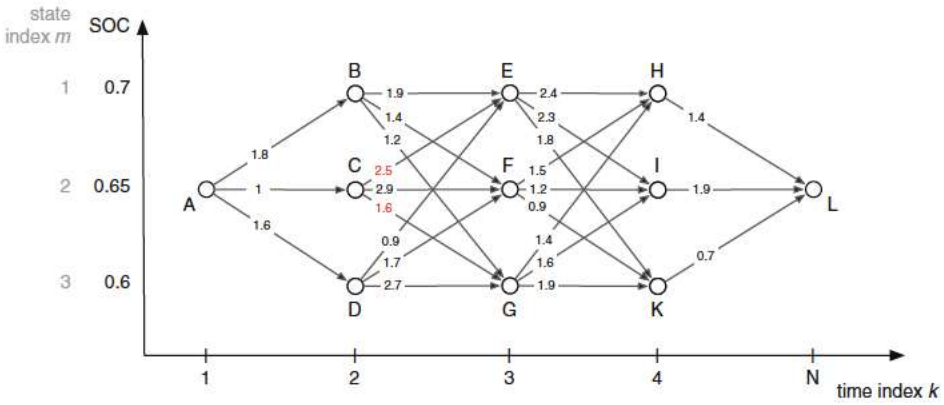

Fig.6: Arc costs [6].

Step 2: Minimize the Cost-to-go

Once all the arc costs have been computed, the cost-to-go, i.e., the total cost of going from one given state to the end of the optimization horizon, can be calculated, starting from the final point and going backwards. The values are reported in Fig.7.

In the proposed example, at step $k = 4$, the cost-to-go $Y_{x,k}$ from each node H, I, K corresponds to the arc cost because the following time instant is the end of the optimization. At $k = 3$ instead, there are several possibilities for each state, considering node E:

$$Y_{E,3}(u = 0) = 2.4 + 1.4 = 3.8$$
$$Y_{E,3}(u = -0.05) = 2.3 + 1.9 = 4.2$$
$$Y_{E,3}(u = -0.1) = 1.8 + 0.7 = 2.5$$

So clearly the optimal cost-to-go from node E is 2.5 and this value can be storage. Proceeding accordingly for the other admissible nodes at $k = 3$, the optimal cost-to-go matrix will result in:

$$Y_{x,k} = \begin{bmatrix} & B & 2.5 & 1.4 \\ A & C & 1.6 & 1.9 \\ & D & 2.6 & 0.7 \end{bmatrix}$$

Due to Bellman's optimality principle, the optimal path from a certain point in the optimal trajectory to the end is not affected by the choice at the previous step, hence, the optimal cost-to-go from B in step $k = 2$ can be computed based on the information obtained at $k = 3$:

$$Y_{B,2} = \min(1.9 + 2.5, 1.4 + 1.6, 1.2 + 2.6) = 3$$

Repeating the process for each admissible point in the state grid at each step, proceeding backwards, the optimum value of the total cost (the optimal cost-to-go from the initial state) can be obtained:

$$Y_{x,k} = \begin{bmatrix} & 3 & 2.5 & 1.4 \\ 4.8 & 4.1 & 1.6 & 1.9 \\ & 3.3 & 2.6 & 0.7 \end{bmatrix}$$

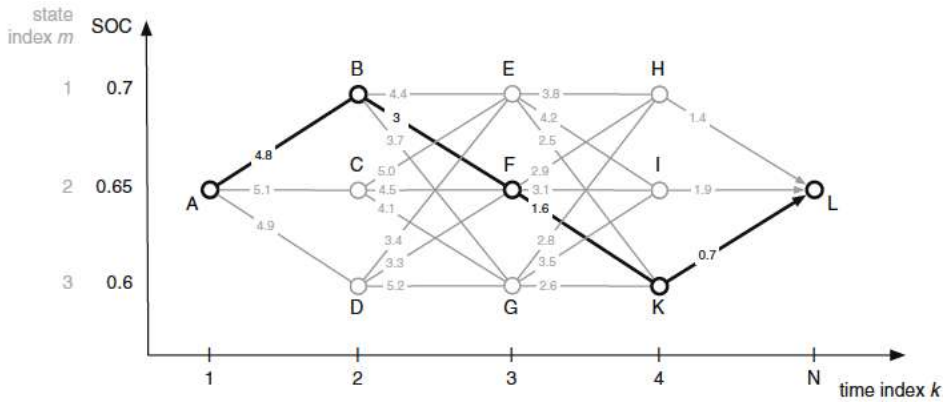

Fig.7: Cost-to-go [6].

Step 3: Compute the optimal path

The optimal path (trajectory of states and controls variables) is the one that minimizes the cost-to-go at each computation step (highlighted by the black line in Fig.2). Therefore, it can be obtained by inspection of the optimal cost-to-go matrix from which the optimal control trajectory can be extracted and then applied to the system (proceeding forward).

One final consideration to be made here is that the application of a given control may drive the system into a state, which does not exactly correspond to one of the discretized values of the state vector X_k. If this happens, the computation of the cost-to-go for each of the state grid values, which is necessary to find the solution, is done through interpolation [6].

The recurrence relation within the DP solution algorithm illustrated by the shown example is available in mathematical terms at [1], [7].

1.3 DP and Plant Models description and results

As stated before, one of the main drawbacks of DP is the burden of the calculations involved. The curse of dimensionality [7] implies an exponential growth of the computational effort with the number of system states. This translates into the necessity of reaching a compromise in terms of model fidelity: usually a higher model complexity means defining additional state variables.

To reach such a balance between accuracy and computational burden, the optimal control trace obtained with DP can be applied to a higher fidelity model, enabling a virtual validation of the system states predicted with the simplified DP model. This process allows understanding which simplifications can be made while maintaining an accurate description of the system dynamics of interest.

The methodology described above was applied to a Sport Car study case:

- Vehicle Powertrain: V8 ICE + P1 on the rear Axle and P4 on the front axle
- DP objective:
    - Case 1: Fuel consumption minimization
    - Case 2: Lap-time minimization

For both cases an overview is provided on how the optimal solution behaves.

The following outputs are analyzed in detail because they are useful for deriving online implementable strategies.

1) Operating modes analysis
    - Statistical information is automatically generated regarding for how long each operating mode is active.
    - Powertrain actuators (ICE, Electric Machines) operating points are analyzed in several planes to aid recognizing significant trends.
2) Gearshift analysis
    - Statistical information is automatically generated regarding the quantity of gearshift events and how long each gear is engaged.
    - Gearshift events are analyzed in several planes to aid recognition of significant trends.
3) ICE starts analysis
    - Statistical information is automatically generated regarding the quantity of ICE start events and engine operation instances.

In the detailed models, strategies have been tuned to avoid non-physical torque/speed profiles during gearshifts and ICE start events. This allows to better account for the total energy needed to perform such maneuvers, thus making the final energy consumption value and lap-time more reliable.

Gearshift simulation

Typical Dual Clutch Transmission (DCT) Powershifts are simulated through simplified controls integrated into the powertrain model. Instead of having quasi-instantaneous gearshifts, a more realistic simulation is performed (see example in Fig.8).

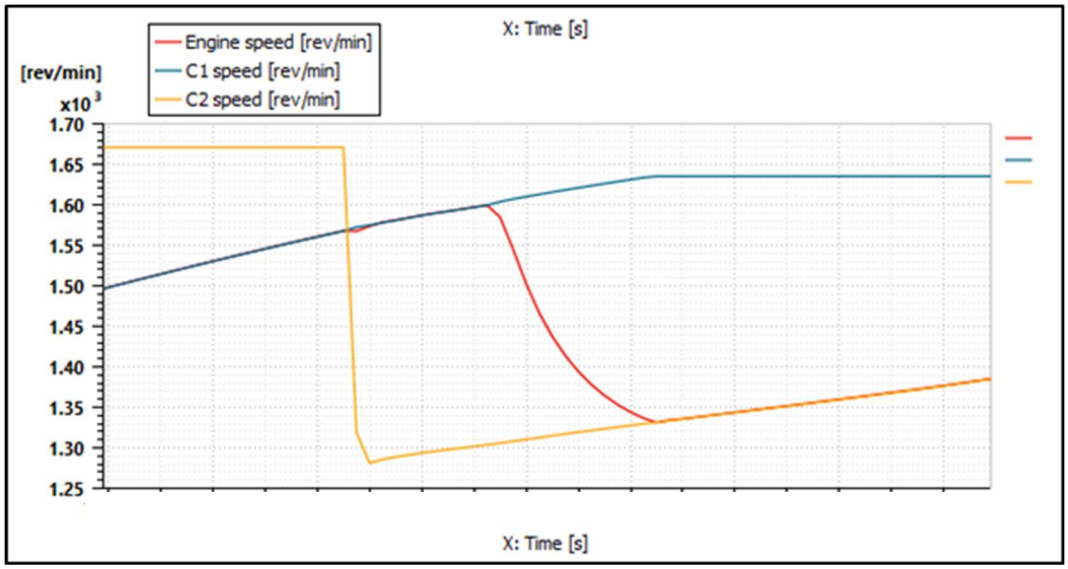

Fig.8: Example gearshift maneuver; C1= odd shaft, C2 = even shaft

ICE starts simulation

Simplified control of clutches and ICE/P1 torques have been integrated into the powertrain model to better simulate ICE starts (only for fuel consumption evaluation).

Controls and models have been tuned to obtain simulation results coherent with the dynamics being analyzed. In particular, preliminary results were carefully analyzed to ensure that physical limits on powertrain actuators are respected and control chattering was removed from the optimal strategies defined. Penalties and constraints have been introduced in both DP and plant models to eliminate chattering on the results as depicted in Fig.9 (i.e ICE on / off switch forbidden within four seconds).

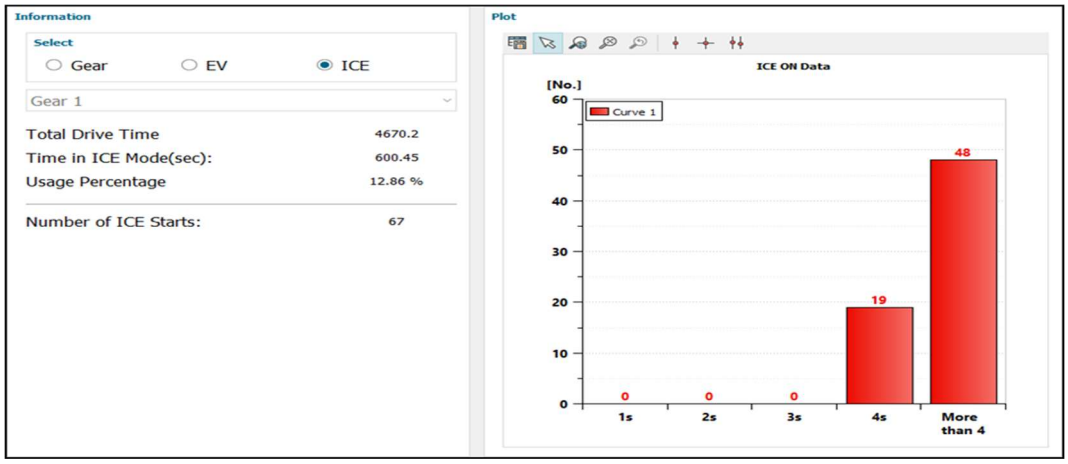

Fig.9: Example numbers of ICE switch as on for chattering analysis

1.3.1 Python simplified DP model for fuel consumption optimization

A simplified 1D vehicle model has been developed in Python.

The model of a single inertia computes the necessary torque at the wheels and the speed of each actuator for all the control inputs possible.

Then the model computes a cost function with defined penalties (targets) and unfeasible penalties to remove not achievable situations.

The DP control computes four variables:

1. ICE torque
2. Rear motor torque
3. Front axle torque
4. Gear engaged

Each variable is described by a 3D map function of: (cycle time, battery SOC, engaged gear)

- Selected Gear → range [0, 8] → If 0 → engine switch as off
- Torque repartition front/rear → range [0, 1]
- Rear torque repartition P1/Engine → range [-1, 1]
    - If 1=> Torque provided by P1
    - If 0 => Torque provided by engine
    - If -1 => Engine produces two times more torque than requested, P1 absorbs excessive torque during regenerative phase.
- Hydraulic brake is applied when requested braking/regenerative torque to electric machine is not reachable.

Policy maps are 3D tables function of [Time, Gear, SOC] (see Fig.10) of the variable control states suggested by DP. Controls will be modified during the simulation depending on the actual SOC.

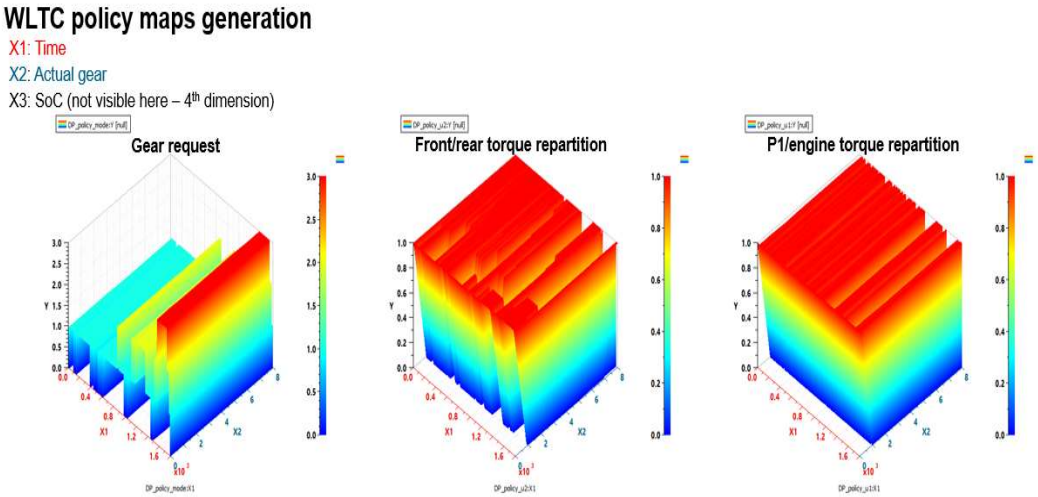

Fig.10: Policy maps example

1.3.2 Python simplified DP model control for Lap Time optimization

For Lap time optimization, a vehicle 2D model (Fig. 11) computes the necessary torque at the wheel and the speed of each actuator for all the control inputs taking into account vertical load on each axle, in order to compute maximum torque transmittable by the tires.

As well as it has been described in the previous section for fuel consumption model, the model used for Lap time computes a cost function with defined penalties (targets) and unfeasible penalties to remove not achievable situation.

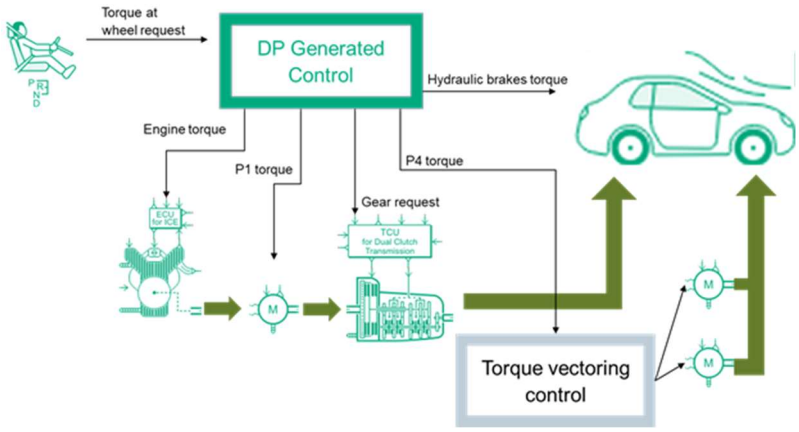

Fig.11: DP simplified model

The DP control variables are:

1. ICE torque
2. Rear motor torque
3. Front axle torque
4. Gear engaged

Each variable described by a 3D map function of vehicle displacement, battery SOC, engaged gear.

- Selected Gear. range [0, 8] → If 0 => engine switch off
- Torque repartition front/rear → range [0, 1]
- Rear torque repartition P1/Engine → range [-1, 1]
- If 1 => Torque provided by P1
- If 0 => Torque provided by engine
- If -1 =>Engine produce twice more torque as requested, P1 absorb excessive torque
- A new variable has been implemented for lap time simulation. A torque repartition between driveline and hydraulic brake torque → range [0, 1]

The DP algorithm needs to be fed with the velocity profile and the road slope to be followed during the cycle (one lap).

A Python script has been developed to generate these two maps from the XYZ coordinates of the track.

Lateral and longitudinal acceleration, max power and tires' friction coefficient are constraints that in combination with track profile are used to find the maximum speed from the optimal vehicle trajectory provided as input (Fig.12).

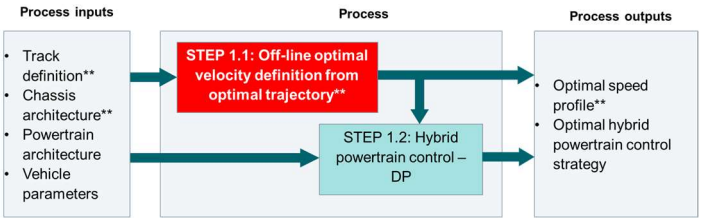

** only for lap time simulation.

Fig.12: Process workflow

1.3.3 Plant model for fuel consumption assessment and results

Model-based control strategies rely on a suitable mathematical model of the HEV powertrain of interest to provide a solution for the energy management problem. For a DP implementation aiming at minimizing the overall fuel consumption, the main modeling objective is to reproduce the most relevant energy flows in the HEV of interest. Hence, a low order dynamic model of the powertrain that considers the principal sources of energy dissipation present in the system is sufficient. These types of models are usually suitable for being embedded into the DP formulation. For the vehicle test case discussed here, the map-based plant model used is shown in Fig.13.

- **Longitudinal driver**: compute acc/brake pedals position in order to follow the predefined velocity cycle. [speed vs time]
- **Controls**: VCU manage torque repartition and gear selection.
- **Engine**: map based with BMEP for torque computation and fuel consumption map
- **DCT Gearbox**: Detailed DCT gearbox with TCU managing smooth gear shift
- **Motors & reducer**: use max torque maps and losses map.
- **Vehicle**: 0D inertia (1 point mass)
- **Battery**: voltage source with SoC computation. With external Losses

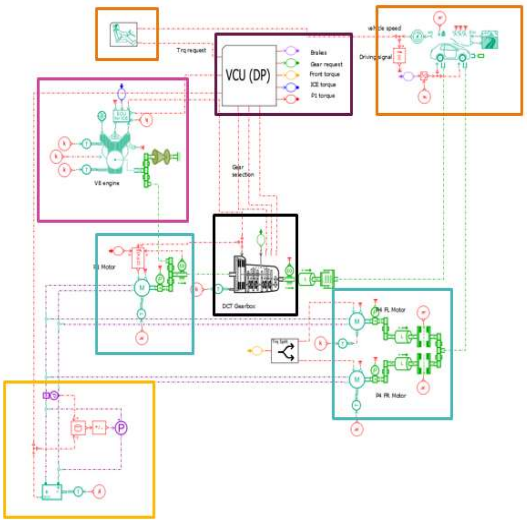

Fig.13: Plant model for fuel consumption assessment

A DCT model has four inertias which represent Flywheel, clutches, primary even and primary odd shafts as depicted in Fig.14.

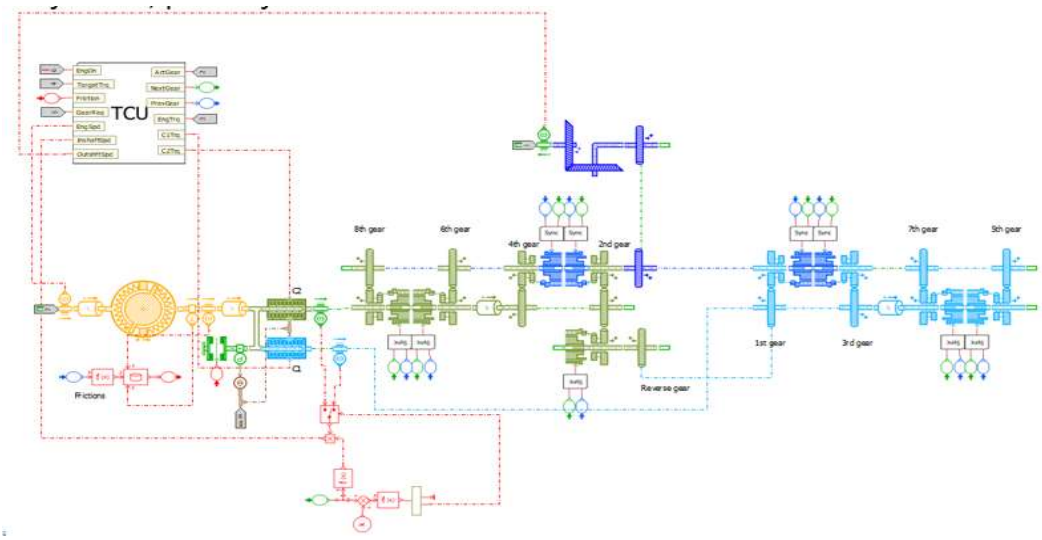

Fig.14: DCT model

The gear selection command works with integer value for gear selection. Transmission Control Unit (TCU) is acting on clutches, synchronizers and ICE to provide the desired torque**.** Different phases during gear selection are described in Fig.15 where C1 and C2 are describing the torque or speed in both primary odd and primary even shafts.

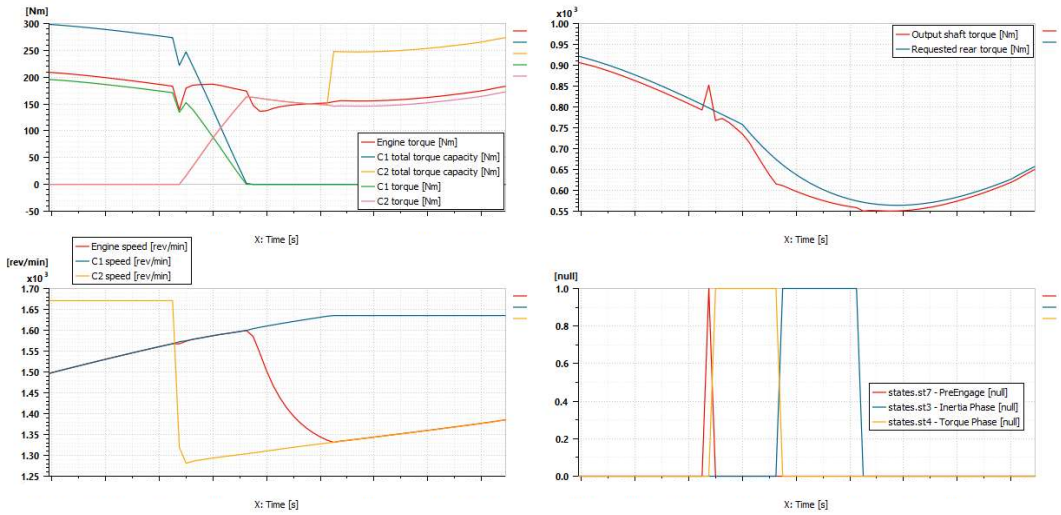

Fig.15: Gear selection phase

- Pre engagement phase: Synchronizer is engaged on the next shaft
- Torque phase: torque is shifted from one clutch to the other
- Inertia phase: Engine speed is controlled thanks to a Proportional-Integral (PI) to match the next shaft speed.

The order of the sequence inertia phase / torque phase depends on whether it is an upshift or a downshift, and if the powertrain is providing or absorbing torque.

The TCU also manages engine restart when required (Fig.16) :

- A constant torque from P1 is used to start the engine (until 1000 rpm).
- A PI controller defines the torque to reach the gearbox input shaft speed.

- Clutch is then closed to match requested torque, PI continue to control ICE speed for a certain time.
- Clutch is then fully closed with torque safety.

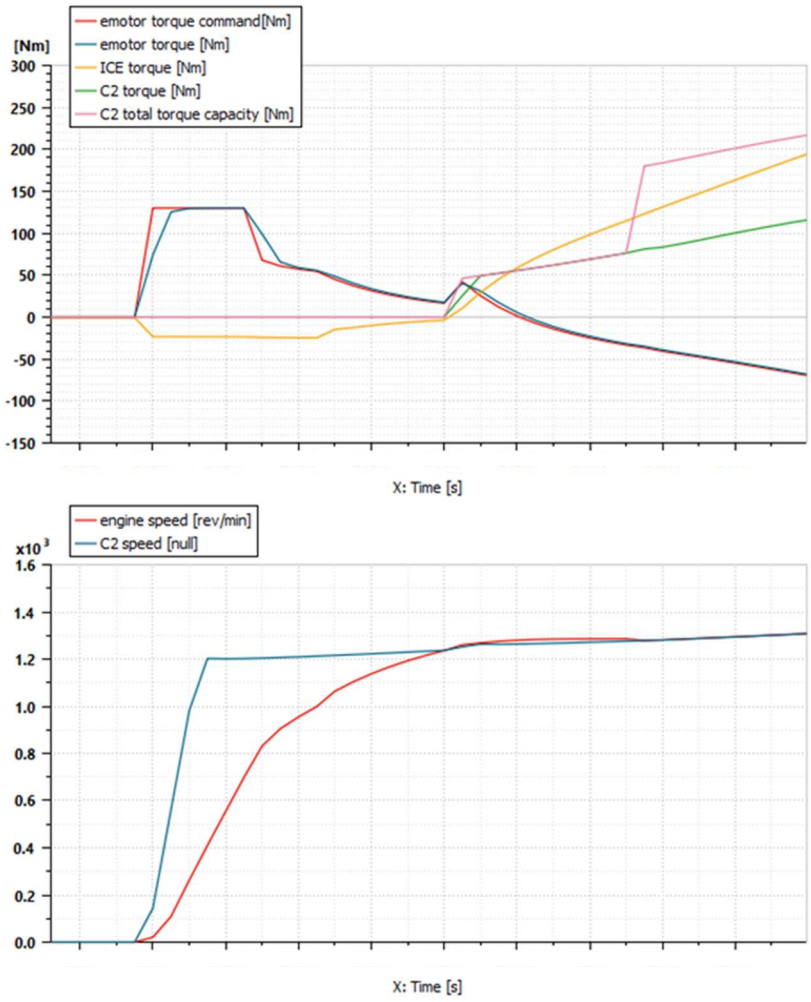

Fig.16: ICE start maneuver

As it can be seen in Fig.17, the embedded DP model prediction matches well that of the plant model used for the forward simulation to which DP control outputs are applied. Slight differences exist in the total fuel consumption due to a more complex simulation of gearshifts and ICE start maneuvers in the plant model, allowing to better account for their energy cost. Note that it is possible to integrate the energy consumption calculation of such maneuvers directly into the DP formulation as shown in [1].

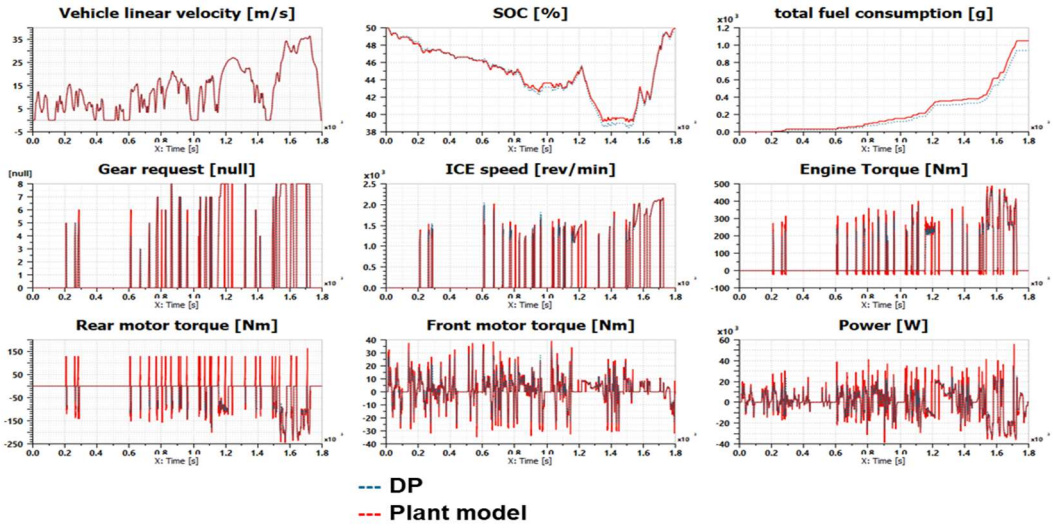

Fig.17: DP vs Plant model: Fuel consumption minimization

At this point, coming back to the main goal of this work, many simulations have been performed in order to find the best strategies in terms of fuel consumption optimization for different SOC levels assigned at the beginning and end of the WLTC cycle. This cycle was designed to represent average driving characteristics from all around the globe. Hence, it is composed of different speed phases: low, medium, high and extra-high. The presence of these driving portions make the cycle more representative of real driving conditions than the NEDC. Each WLTC repetition takes 1800 sec and only for the Charge – Depleting run, three repetitions have been simulated in order to use the maximum battery energy potential.

A) Charge-Depleting run
- Drive cycle: WLTC (3 repetitions)
- Initial SOC: 90%
- Final tgt SOC: Free
- SOC range: 30-90%

B) Charging run
- Drive cycle: WLTC (1 repetition)
- Initial SOC: 30%
- Final tgt SOC: 80% (0.5% tolerance)
- SOC range: 30-90%

C) Charge-Sustaining run
- Drive cycle: WLTC (1 repetition)
- Initial SOC: 50%
- Final tgt SOC: 50% (0.5% tolerance)
- SOC range: 30-90%

For Charge - Depleting run (Case A) at low and medium load within the first 1000 sec of the cycle, power requests below 20 kW are usually undertaken by P4.

P4 can handle all the braking torque. Therefore, friction brakes are never used.

P1 is used to startup the engine.

When the ICE is running, P4 is not used and P1 regenerates part of the ICE power delivery (Fig.18).

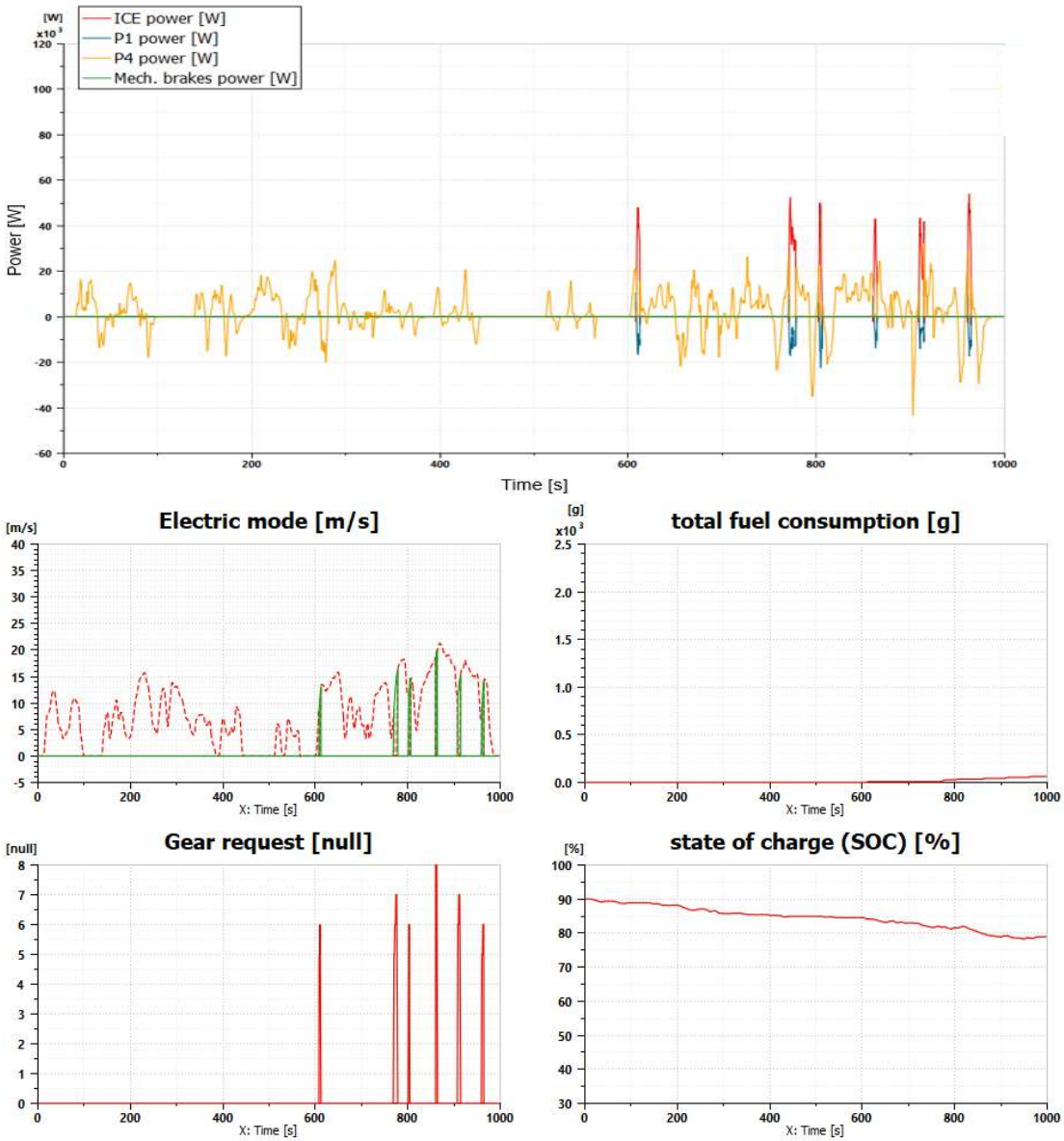

Fig.18: Charging Depleting WLTC low – medium load [0-1000 sec]

At high and extra high load, as observed within the last 800 sec of the third repetition of WLTC, the optimal solution shows a quasi-linear trend of SOC which matches what is expected from the available literature.

The controller exploits most of the available battery energy since the objective was only to minimize fuel-consumption.

P4 still behaves as mentioned before (Fig.19).

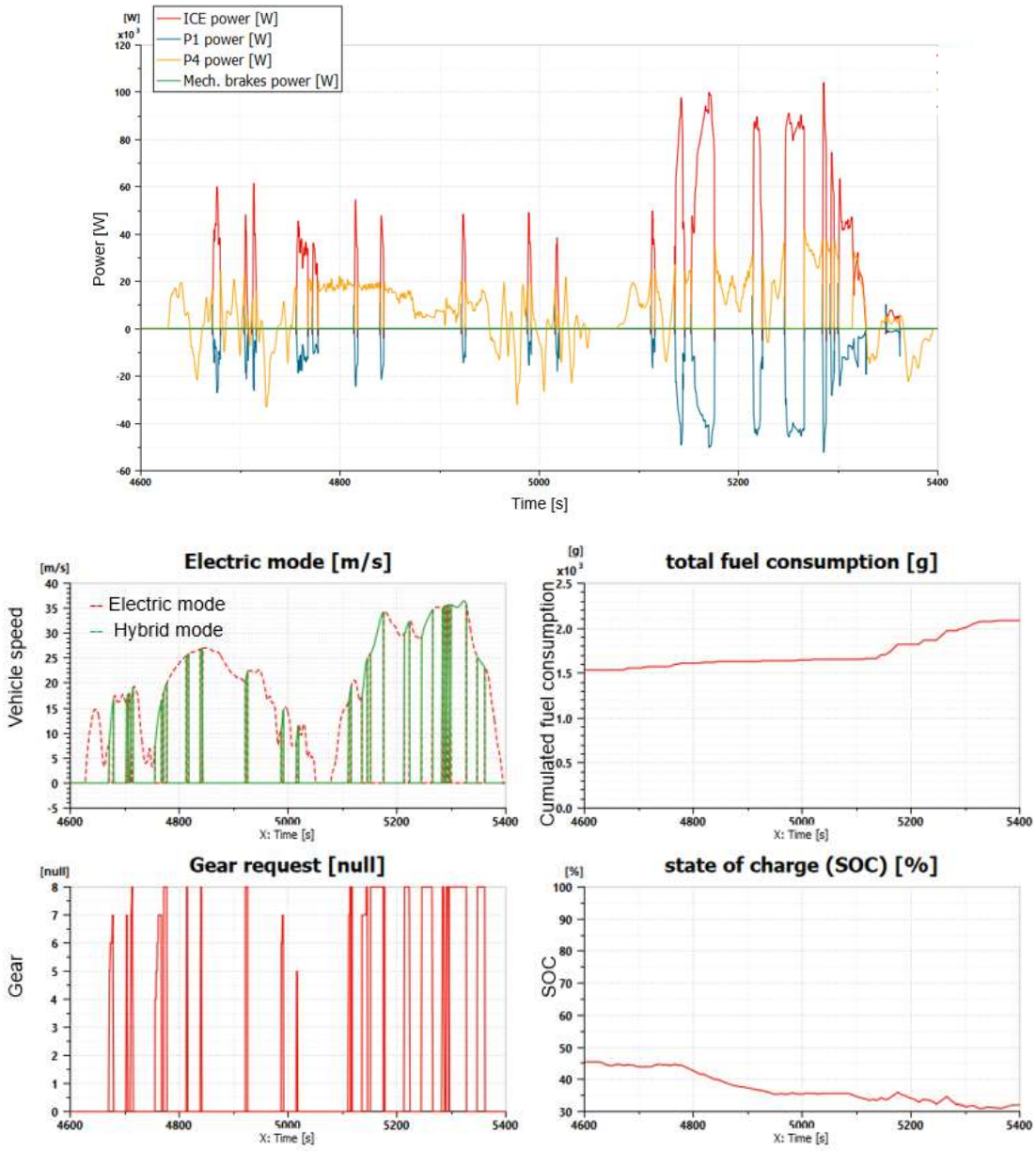

Fig.19: Charging Depleting WLTC high – extra high load [4600-5400 sec]

As it can be seen in the following plots, strategies suggest to use ICE to the lowest rpm possible all the time (Fig.20).

P1 is mostly used for engine crank (positive torque from 0 to 750 rpm) and regeneration mode (negative torque) which is exploited for both ICE on and off condition.

P4 is not forced to follow the ICE speed. It goes up to 15000 RPM and uses both positive and negative torque (Fig.21).

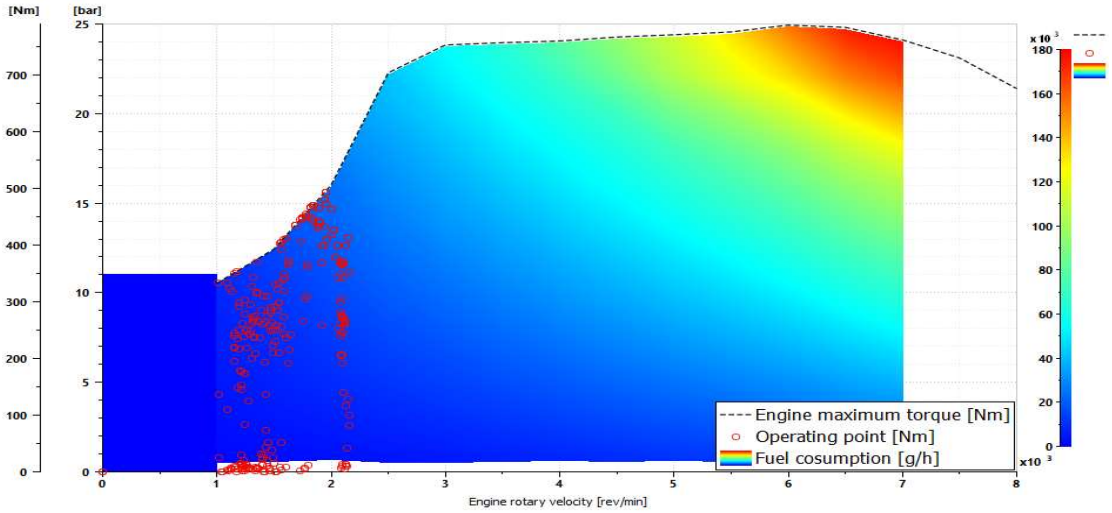

Fig.20: Charge Depleting run: ICE operating point

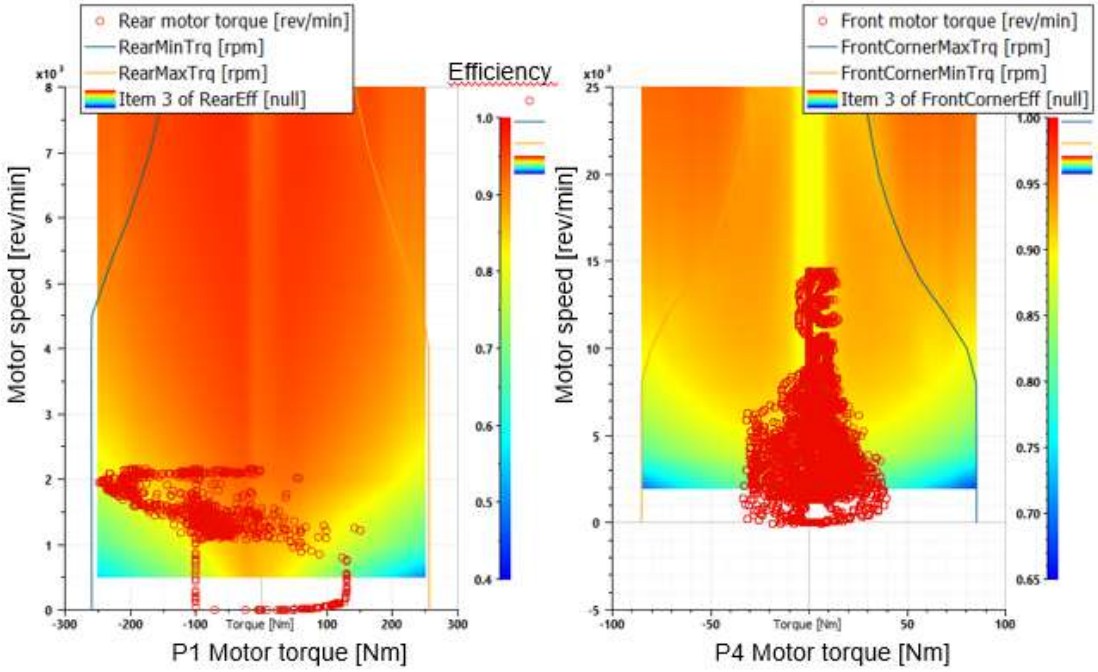

Fig.21: Charge Depleting run: P1 and P4 operating point

The optimal downshift / upshift patterns which are greatly related to the vehicle speed is showhn in Fig.21. The colour of each dot point represents the gear engaged. Gear = zero means ICE switch off.

Most of the upshifts happen from null (the engine is turned on from 5 to 35 m/s)

All the downshifts go to null. These results are useful to extract a DP inspired rule for optimal strategies.

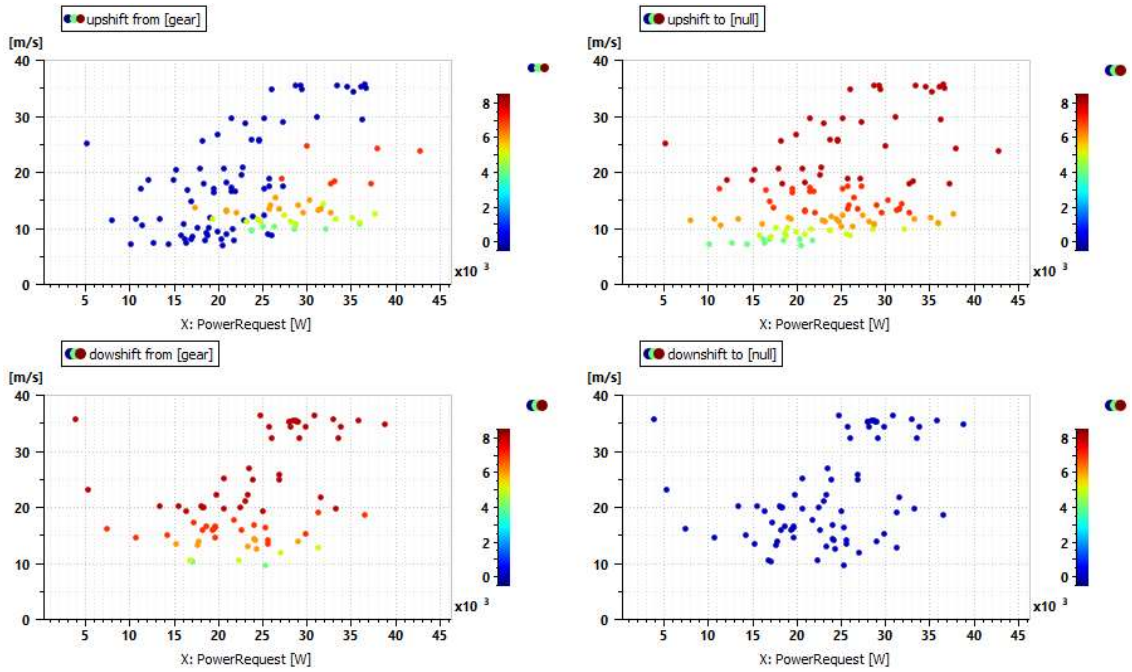

Fig.21: Charge Depleting run: Gear Shift event Vs Power request Vs vehicle speed

Tuning of the toolbox parameters and an appropriate selection of the cost function lead to an acceptable level of both gear shift and ICE crank chattering. No change of strategy takes place within three sec (Fig.22).

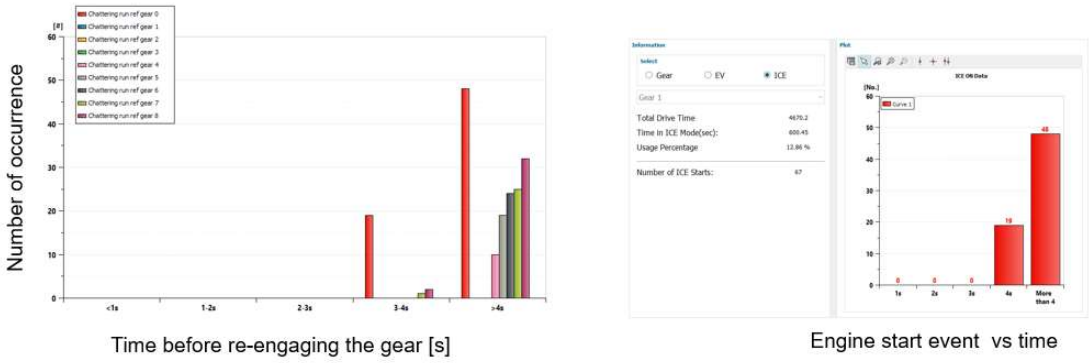

Fig.22: Charge Depleting run: Chattering analysis

From the mode analysis, we can see that all the EV drive is made thanks to P4 motor and gearbox in neutral. For the braking situation, P4 are used mainly whilst P1 is used for cranking and regeneration (Fig.23).

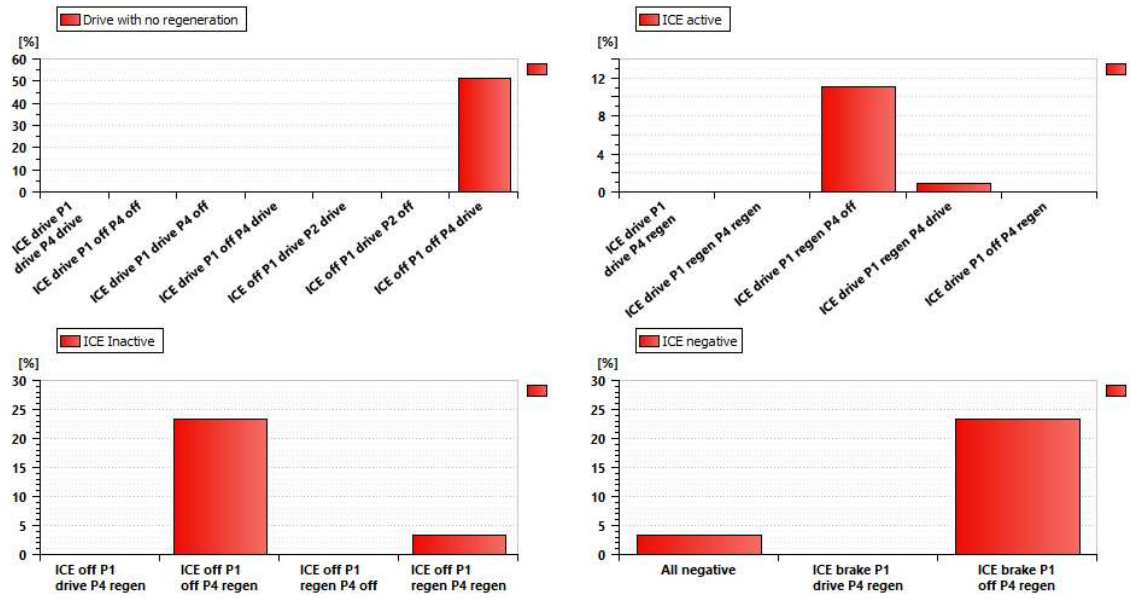

Fig.23: Charge Depleting run: Operating Mode analysis

For one repetition of WLTC, same analysis have been carried out for Charging run (Case B) and Charge – Sustaining run (Case C) and only a few of the most important outputs are shown below (from Fig.24 to Fig.33).

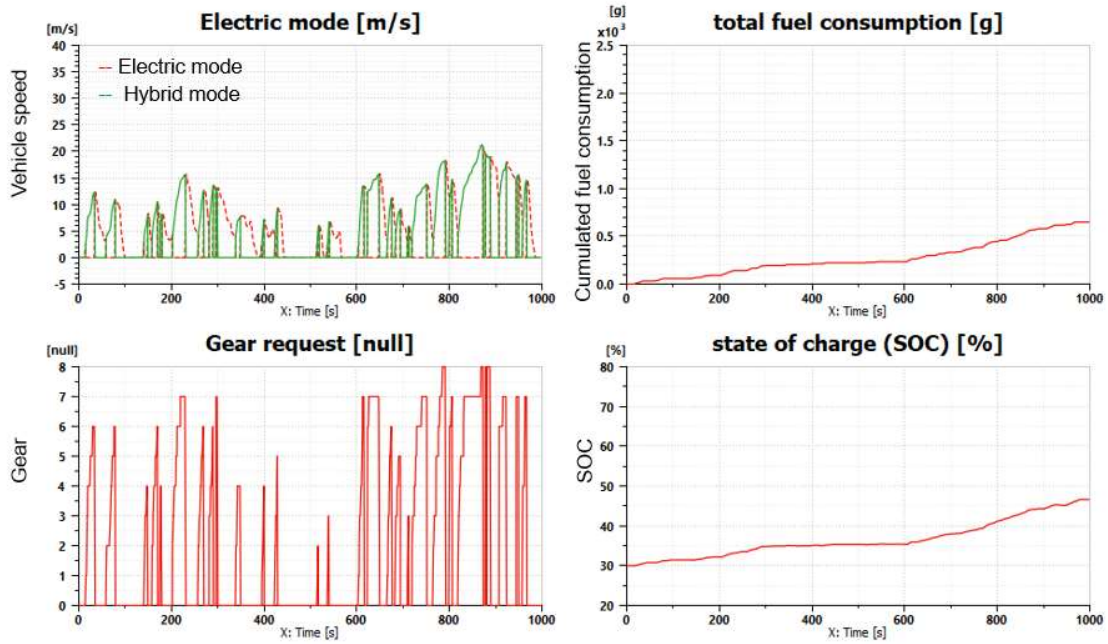

Fig.24: Charging Run WLTC low – medium load [0-1000 sec]

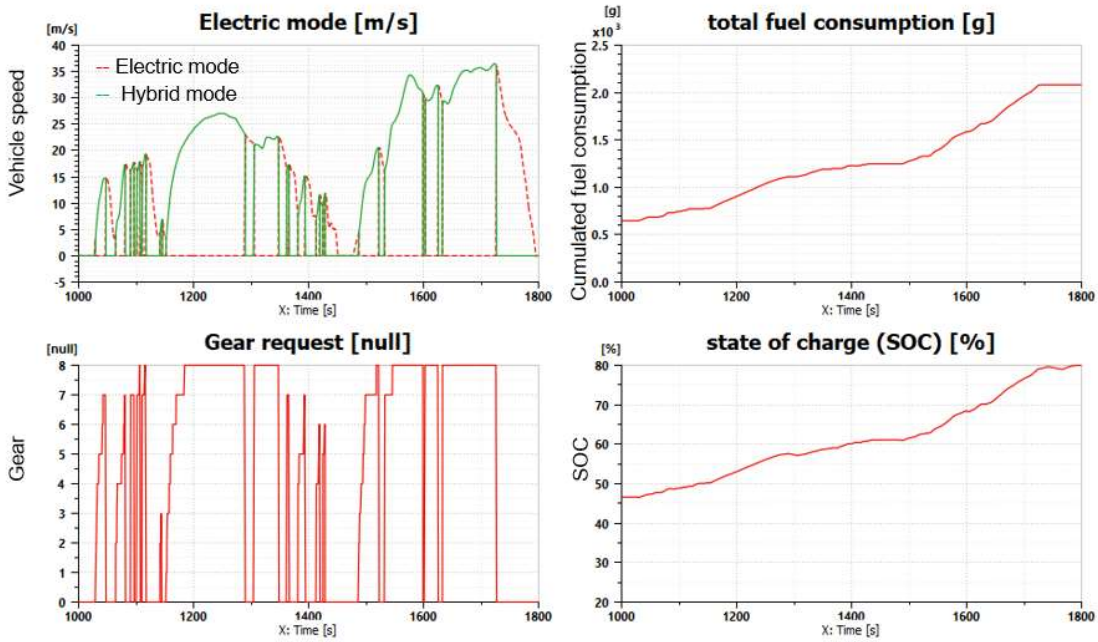

Fig.25: Charging Run WLTC high – extra high load [1000-1800 sec]

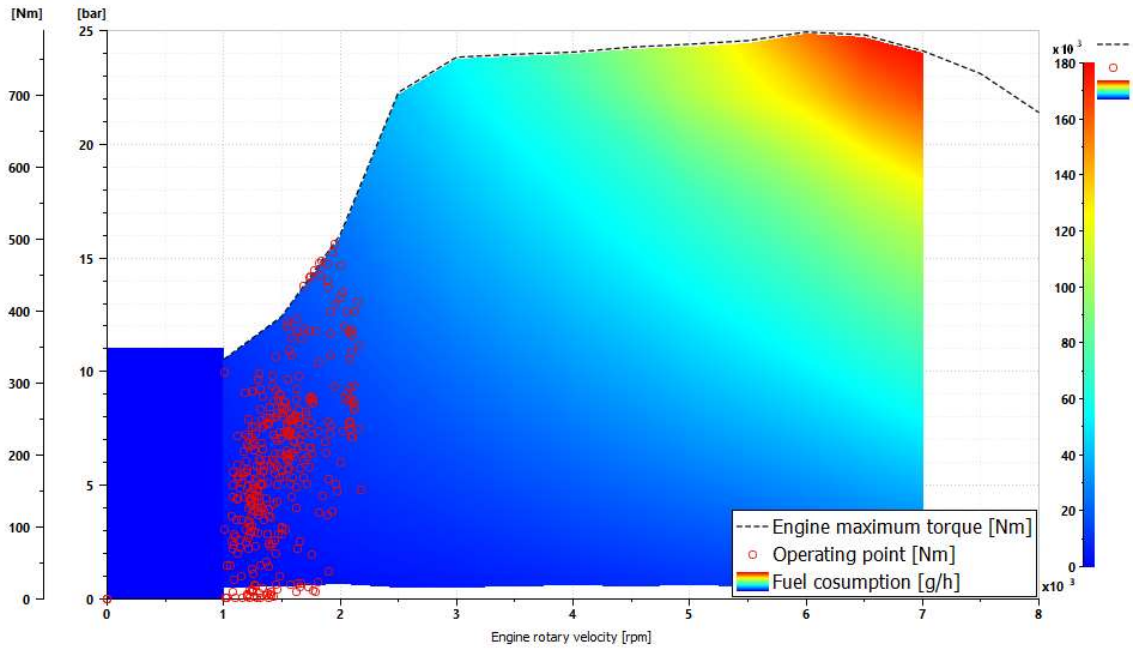

Fig.26: Charging Run: ICE operating point

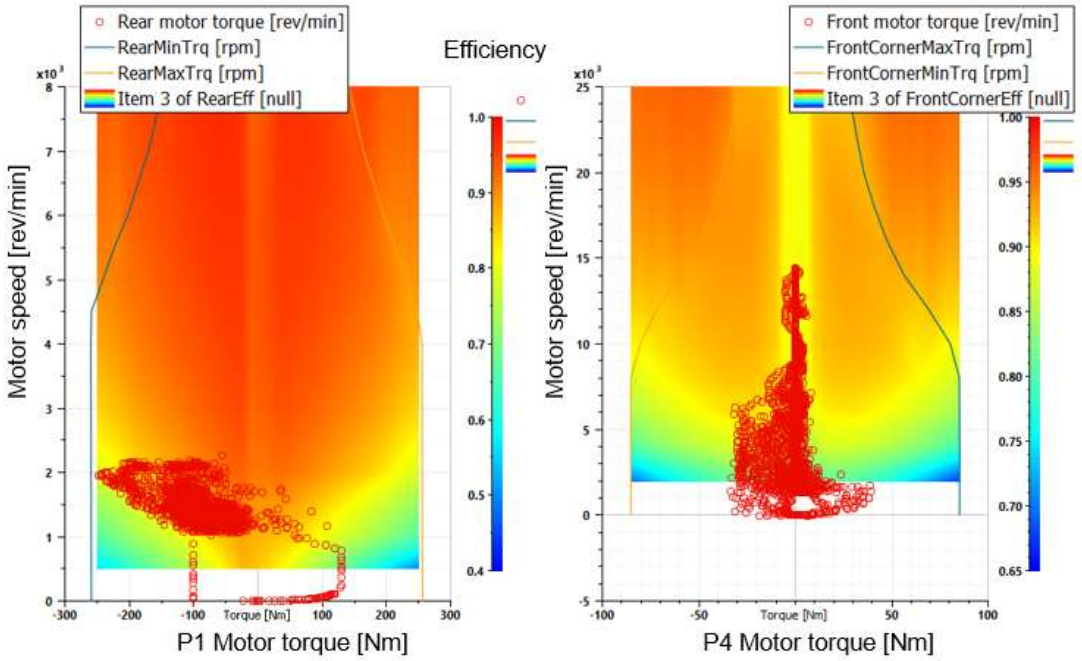

Fig.27: Charging run: P1 and P4 operating point

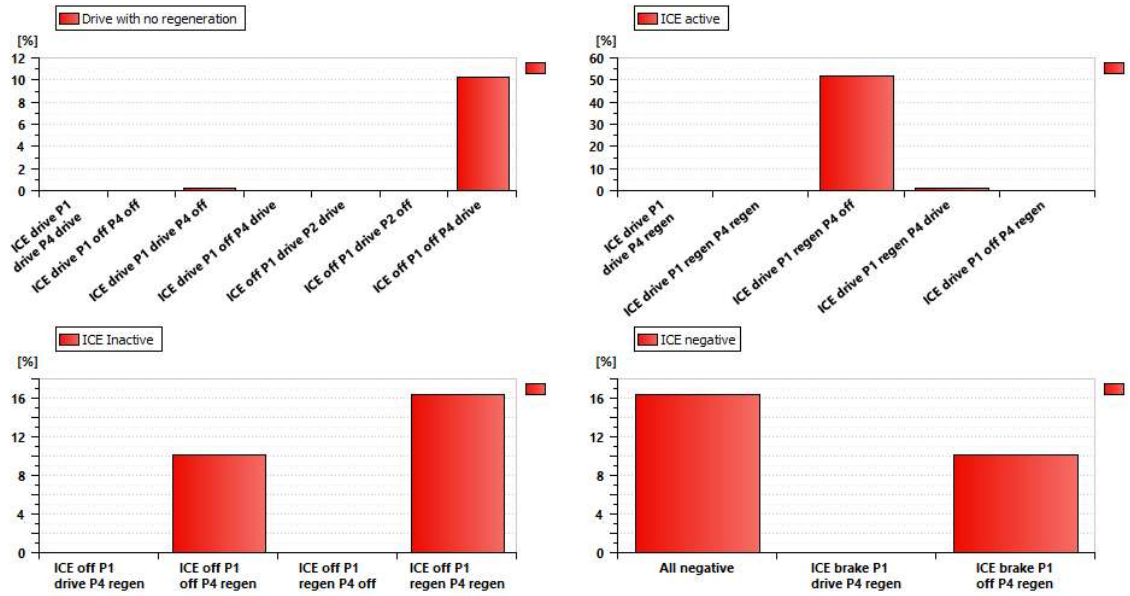

Fig.28: Charging run: Operating Mode analysis

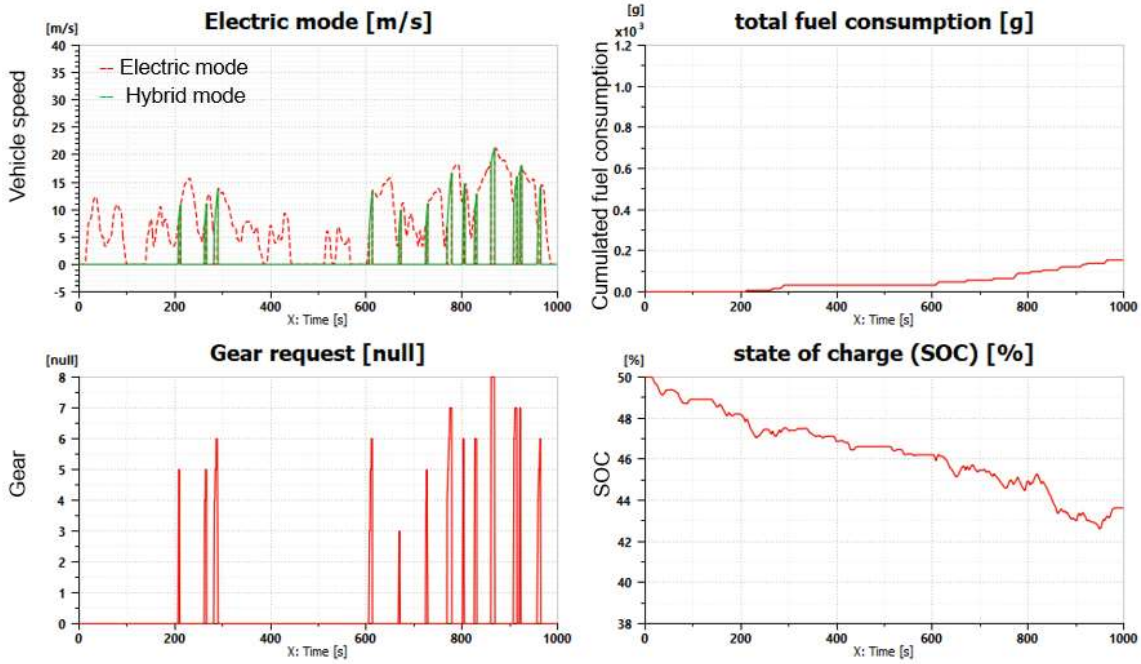

Fig.29: Charge Sustaining WLTC low – medium load [0-1000 sec]

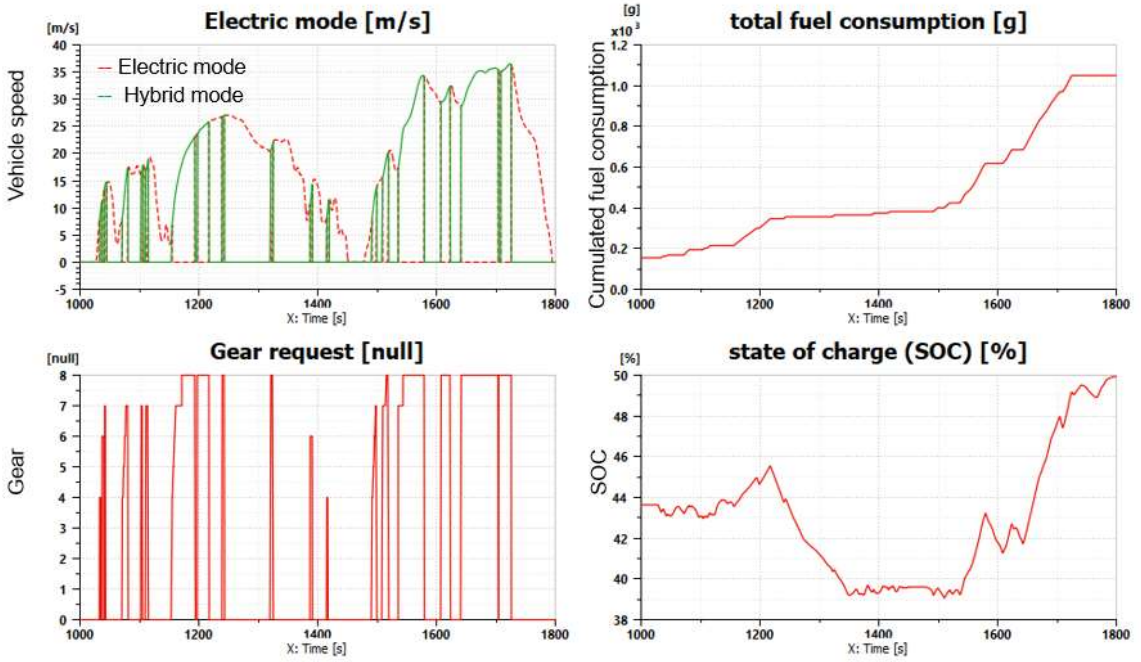

Fig.30: Charge Sustaining WLTC high – extra high load [1000-1800 sec]

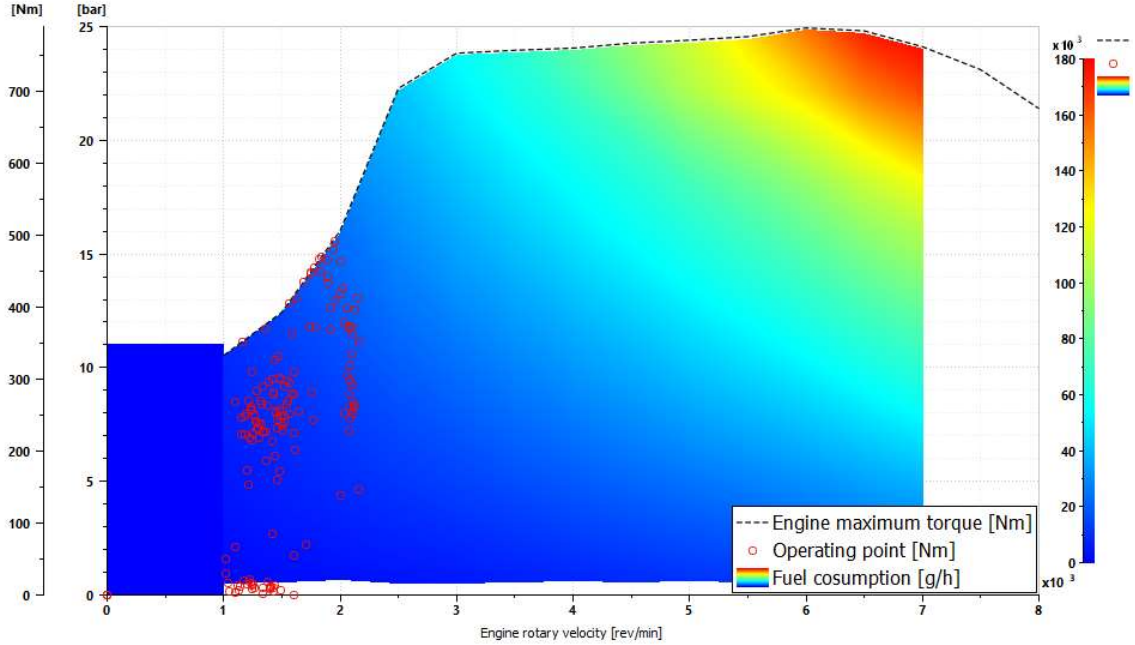

Fig.31: Charge Sustaining: ICE operating point

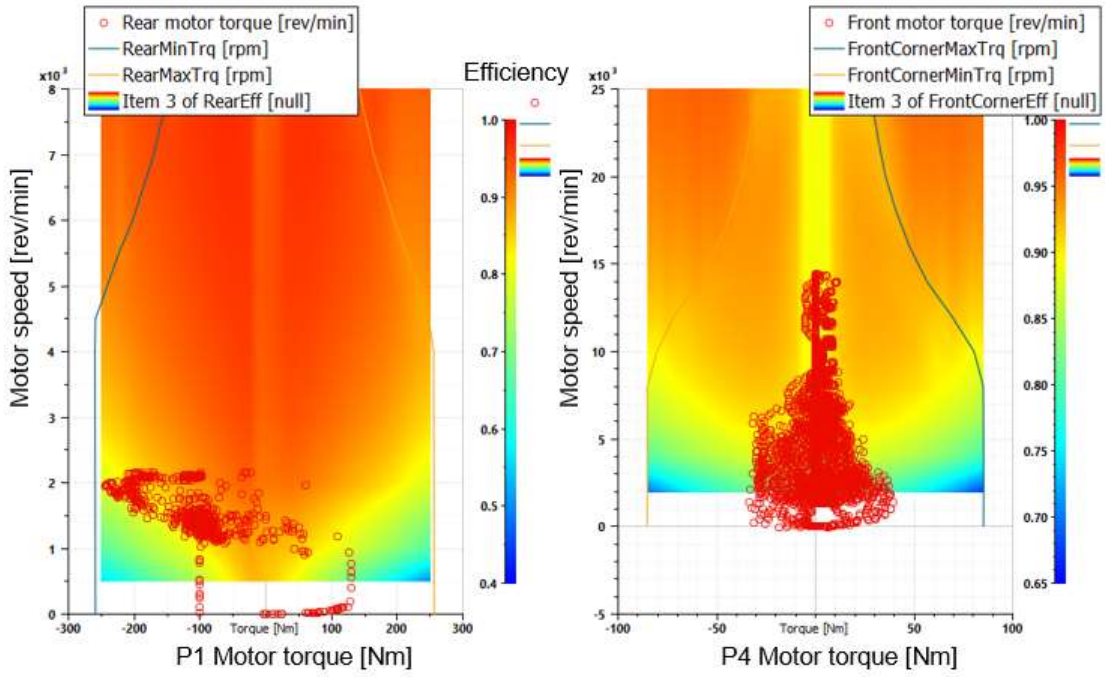

Fig.32: Charge Sustaining: P1 and P4 operating point

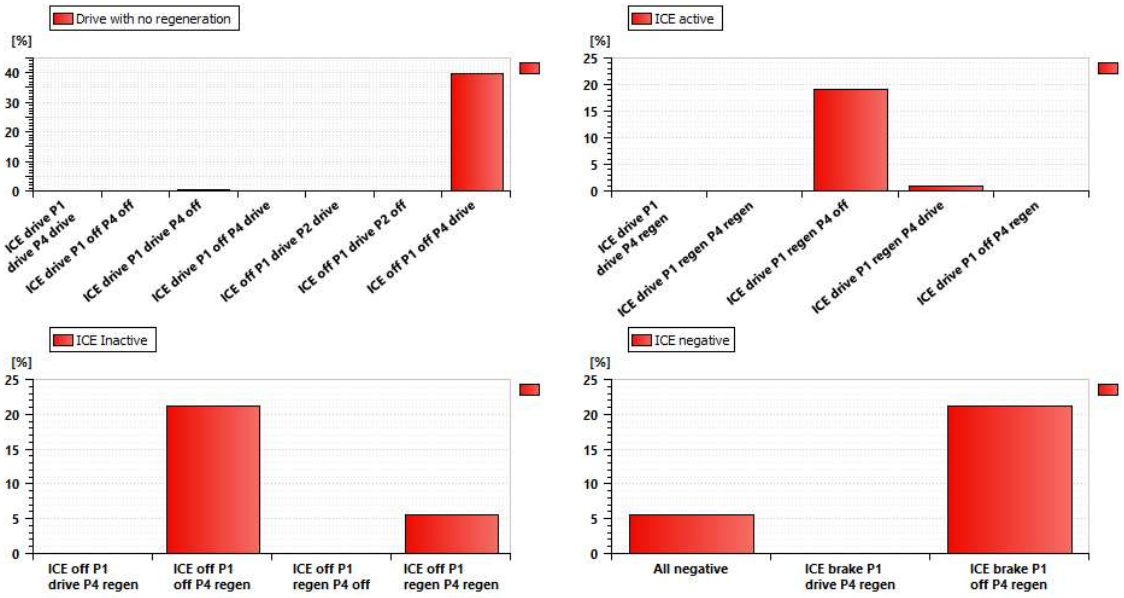

Fig.33: Charge Sustaining: Operating Mode analysis

1.3.4 Plant model for Lap time assessment and results

Differently from case 1, higher complexity models are needed for lap-time assessment since vehicle dynamics need to be taken into account. Therefore, the powertrain model is integrated with a more complete vehicle model, which include chassis, suspension and wheels simulator (Fig.34).

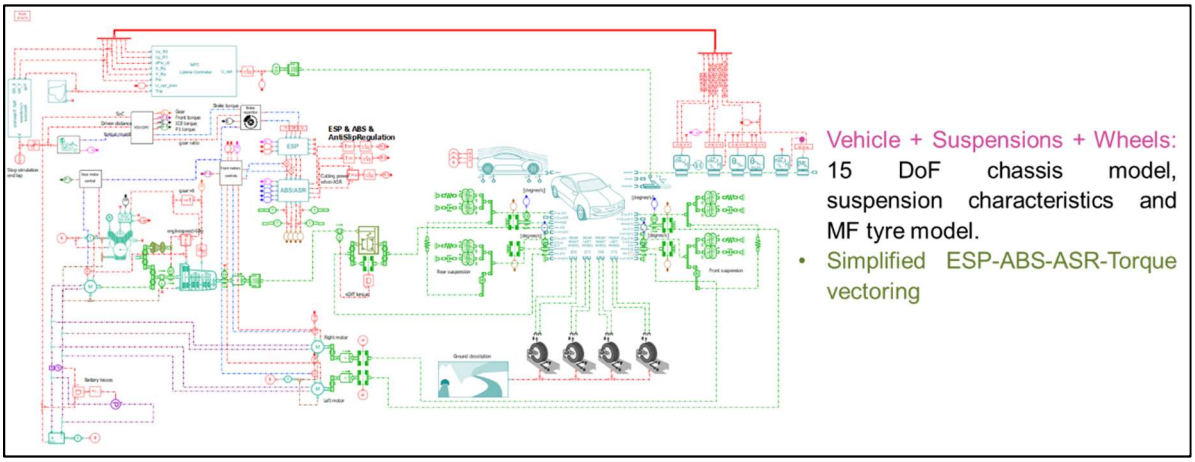

Fig.34: Plant model: Lap-time minimization.

In this case, it can be seen in Fig.35 that some differences arise between the DP embedded model estimates and the plant model, especially in terms of SOC.

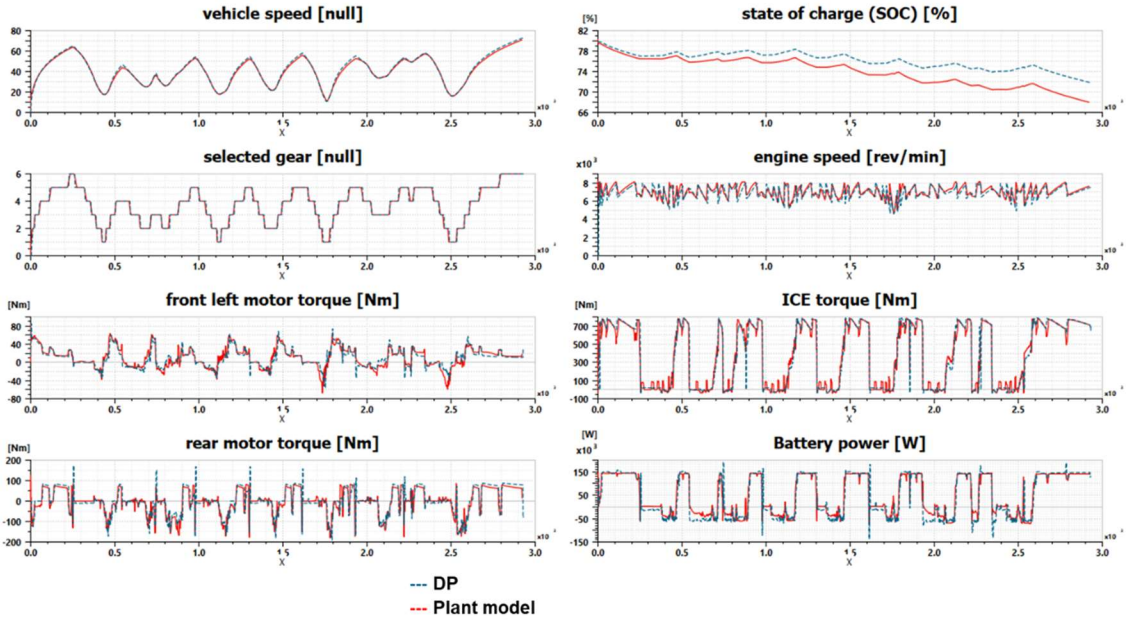

Fig.35: DP vs. Plant model: Lap-time minimization.

During the forward simulation, a lot of energy is dissipated by the safety systems (ABS, ASR, ESP) while using hydraulic brakes for vehicle stability purposes. Due to the computational burden that would be involved, these low-level controls are not considered by the DP formulation. To illustrate the relevance of such assumption, the energy dissipated by the safety systems is computed and converted in terms of equivalent Battery SOC. A corrected SOC is then calculated which is much closer to the SOC predicted by the DP (Fig. 36).

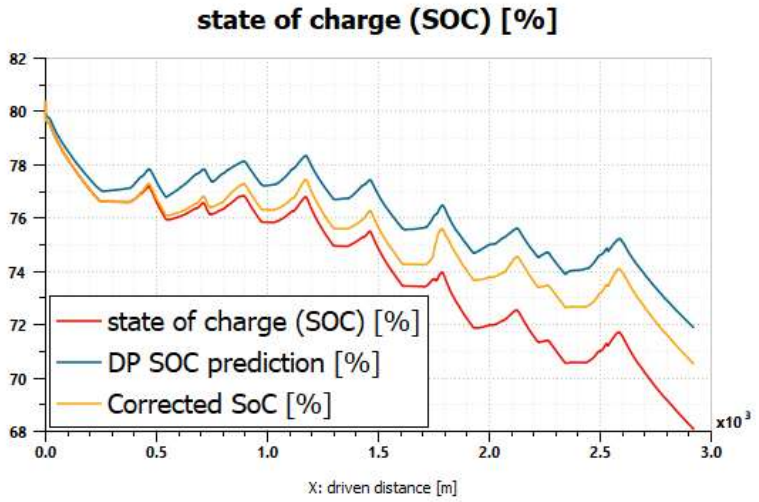

Fig.36: DP vs. Plant model: Lap-time minimization SOC.

As it can be observed in the next graphs (Fig.37-38), when power is requested, ICE is delivering more power than requested most of the time.

To avoid exceeding the battery power or the maximum torque at input shaft of the gearbox but also to avoid providing too much torque to the rear wheels, P1 is often used as generator at high rpm while P4 provide torque to help accelerate.

P4 are also mainly used for regenerative braking.

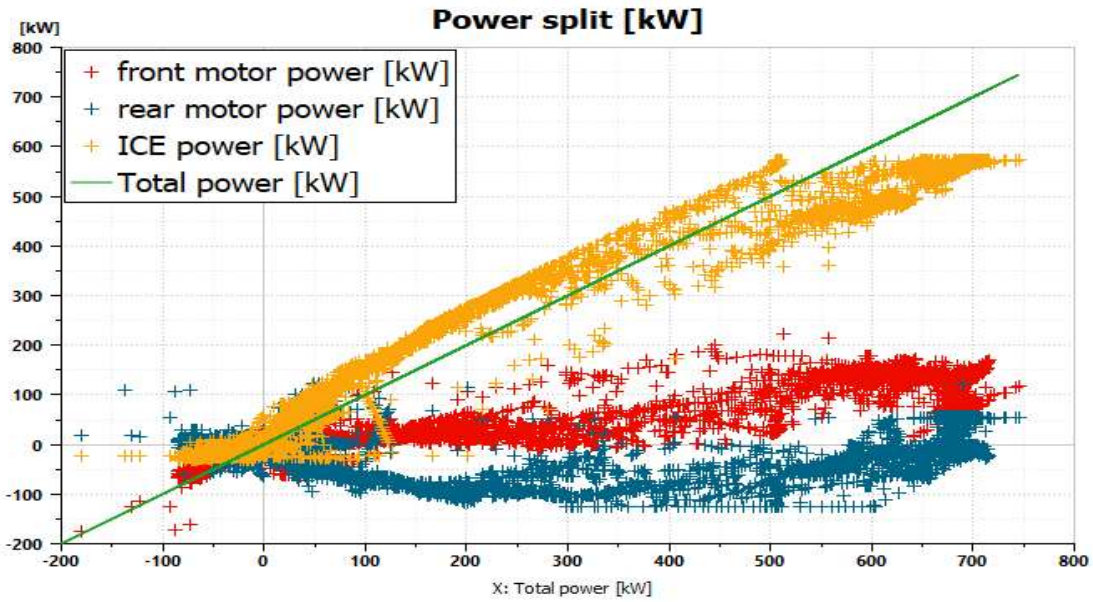

Fig.37: Lap time simulation: Power split assessment

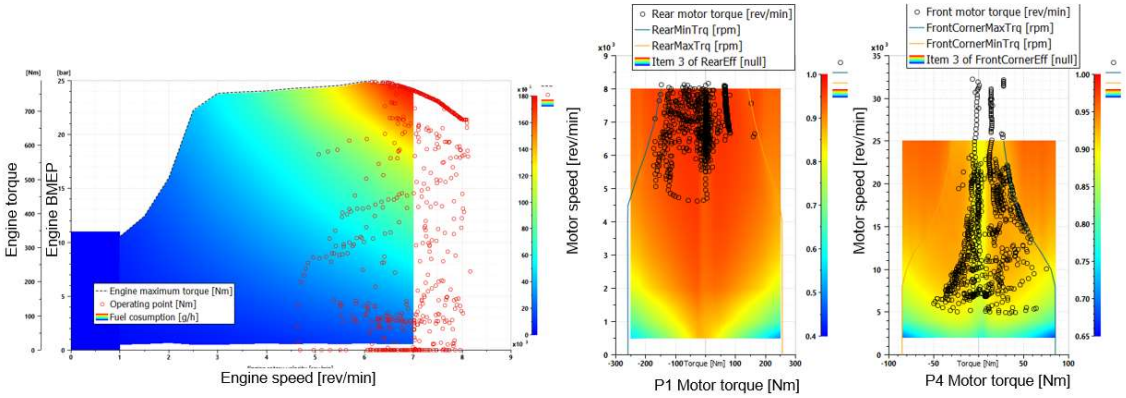

Fig.38: Lap time simulation: ICE- P1- P4 operating points

Analyzing the battery usage during lap time (Fig.39), battery maximum power is used for very strong acceleration in a straight line and maximum recharge is happening in the second part of the turns. When low positive power is requested, the ICE can provide a lot of energy to recharge the battery.

For negative power request, the inertia is used to recharge the battery via regenerative braking. When the braking request is too high, only hydraulic brakes are used.

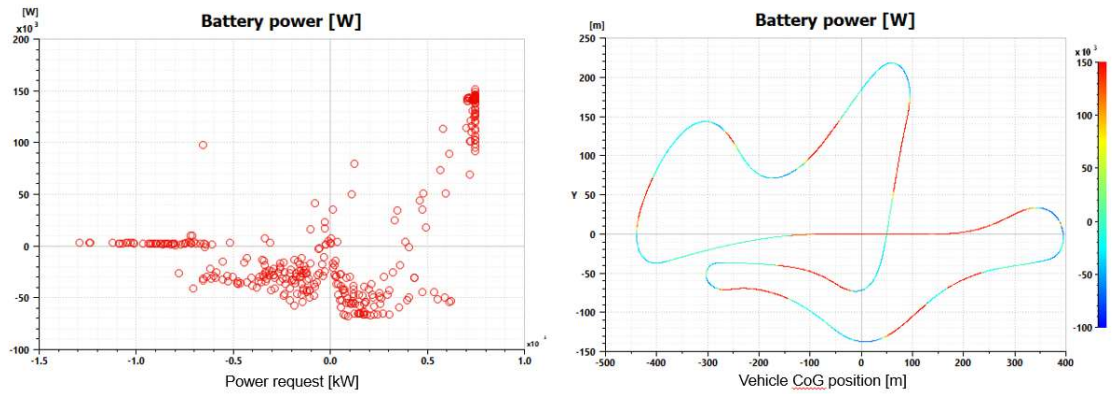

Fig.39: Lap time simulation: Battery usage

Finally, in the next plots (Fig.40-41), the strategies are shown about how each power source (ICE, P1 and P4) have to be used during lap time simulation in order to get best lap time.

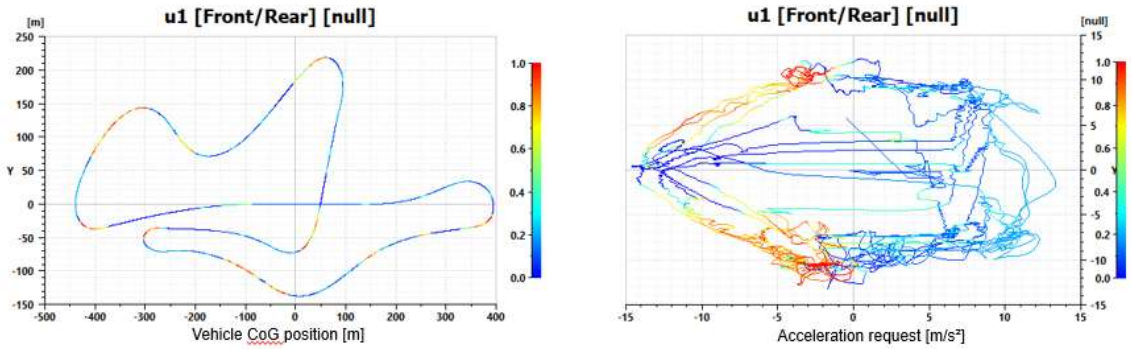

Fig.40: Lap time simulation: Front (P4) and Rear (ICE + P1) Torque split factor

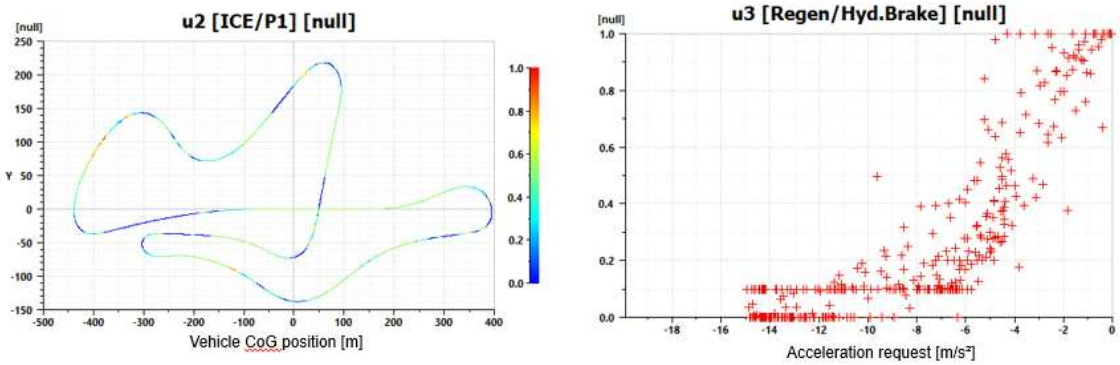

Fig.41: Lap time simulation: ICE vs P1 and Regen Vs Hyd. brake split factor.

1.4 Conclusions

In this chapter, DP is used to find the global optimal solution to the energy management of the HEV described in the previous section. The analysis considered a type P1-P4 HEV as a test case and the research focused on the development of a methodology based on optimal control theory to maximize fuel economy and minimize lap time in sport driving conditions. Due to the possibility to explore different power sources, at each stage, the interesting output was to know how they should be combined in order to find the optimal usage.

The general problem formulation was given. Each state and control variable are defined and the reasons behind their introduction are explored. DP method is used to assess the maximum powertrain capabilities relying on simplified vehicle models, called *DP model,* which was implemented in Python enviroment. The information collected from the DP, is used to create policy maps depending on the main states of the powertrain, which are given as inputs to high fidelity models, called *plant model,* which was implemented in Amesim platform licensed by Siemens, used for the final assessment of the proposed control strategy.

Moreover, the constraints imposed together with the characteristic of the state and control are also reported. The modeling of the gearshift and ICE start losses are integrated into the DP formulation.

The WLTC is considered for the simulations performed with the aim to assess the suggested strategies as optimal solution for fuel consumption minimization.

The simulation results obtained with the described *DP and Plant model* formulation are shown in the section 1.3.3 for three different cases:

1) Charge-depleting run.
2) Charging run.
3) Charge-sustaining run.

Lastly, lap time simulation and the strategies carried out in order to get best lap time are shown in the section 1.3.4.

A deeper analysis of these results for both simulation scope can be used as a benchmark for developing real-time implementable control strategies: possibility to learn from the optimal solution. In addition, such a benchmark enables a fair comparison among different power sources variants.

As next steps, the methodology here proposed and based on a given vehicle architecture and specific power actuators, could be evolved to find the **best size of key components** (motors performance, battery capacity, etc.) through DoE and/or Optimization algorithm and/or to execute a Multi-Attribute balancing with crossed evaluation between architectures for the selection of:

- Best architecture.
- Best hardware design/size.
- Optimal control strategy.

Chapter 2

Virtual assessment of an After-Treatment System equipped with Burner to Speed-up the Light-off at the Engine Cold Start

2.1 Introduction

In the next years, the upcoming emission legislations are expected to introduce further restrictions on the admittable level of pollutants from vehicles measured on homologation cycles and real drive tests. By the end of the decade, the current emission legislation for the automotive sector is expected to evolve worldwide towards a more restrictive scenario, with a further limitation of the admitted levels for pollutant and greenhouse emissions [1, 2]. In Europe, this revision process of the current regulation will lead to the definition of the novel Euro 7 legislation, expected to be introduced within 2030. At the time the author is writing, there hasn't been a decision on the emission limits for Euro 7 legislation. Therefore, a significant effort of design exploration must be performed virtually, in order to select the best technical solutions to achieve the expected targets for the design of the upcoming vehicles.

An integrated system of vehicle control must take into account the strict control of pollutant emissions at the cold start, which will become a crucial point to comply with the new regulation standards. This will necessarily require the implementation of novel strategies to speed-up the light-off of the reactions occurring in the after-treatment system, since the cold start conditions are the most critical one for cumulative emissions. Among the different possible technological solutions, this research focuses on the evaluation of the potential of a burner system, which is activated before the engine start. The burner exploits the lean combustion of an air-gasoline mixture to generate a high temperature gas stream which is directed to the catalyst section promoting a fast heating of the substrate. In this chapter, an experimental test bench has been adopted to characterize the thermal transient of the after-treatment system when the burner is activated, monitoring the temperature of the gas flow and the temperature of the metallic walls at different locations. Moreover, a CFD model has been developed to investigate the light-off of the reactions during the initial operation of the burner and the subsequent start of the engine. The model, developed on the basis of the OpenFOAM code, resorts to a multi-region approach, where different meshes are employed to describe the fluid domain and the solid regions, namely the catalytic porous substrates and the metallic walls constituting pipes and canning. Specific submodels are implemented to consider flow resistance, heat transfer, mass transfer and catalytic reactions occurring in the catalyst region. The CFD framework has been initially validated on the experimental data acquired on the test bench. The methodology has been then applied to the preliminary analysis of the catalyst light-off at engine cold start, considering a full exhaust line equipped with burner.

With these premises, this work focuses on the operation of an after-treatment system equipped with a catalyst burner with the aim to evaluate its potential for the speed-up of the catalyst light-off. In this preliminary study the device is investigated under lab conditions considering a specific test bench, where the operation of the burner can be suitably controlled in all the running phases. The study focuses on the after-treatment system of a high-performance SI gasoline V12 naturally aspirated engine, in order to investigate the behavior of the system during the cold start phase because, at the time of this study, experimental activity and results were suitable for the validation of the model. As the investigation was principally on the after treatment system and not the engine itself, the proposed methodology is generally applicable also to turbocharged engines, such as those used in the other chapters of this thesis. To this purpose, an advanced CFD model is developed on the basis of the open-source OpenFOAM code, with the aim of describing the complex multi-physics nature of the problem which involves different phenomena occurring at different scales, including: mass/heat transfer, chemical reactions, flow through porous media, etc. The numerical model allows the detailed description of the after-treatment geometry by means of a fully-3D approach, making it possible to describe the flow and temperature distribution in the system, enabling the optimization of the configuration. Moreover, it implements advanced catalyst models to evaluate the non-uniformity of the pollutant conversion occurring on the catalytic substrate. The solution algorithm is optimized in order to allow the simulation of quite long time interval, in the order of magnitude of minutes, in such a way to be applied to the analysis of significant portions of the homologation / real driving cycle. More specifically, the scope of this work is confined at the cold start strategy where a pre-heating device has a disruptive impact whereas light-out phenomenon or subsequent burner re-activations, which are not yet guaranteed in terms of component reliability, are preferably assigned to a 1D approach as more reasonable to establish the best possible strategy rather than a 3D one.

2.2 Methodology

The analysis of the after-treatment system equipped with burner heating was performed with a combination of CFD investigations and experimental characterization. In particular, experimental measurements were exploited for the model validation, with particular regards on the thermal aspects. Alongside, CFD analysis were applied for a comprehensive study of all the complex aspects involved (i.e. heat-/mass-transfer, chemical reactions, flow through porous media) and of their interaction, to provide a deep insight of the phenomena occurring at the engine cold start.

2.2.1 Simulation model

The computational model adopted in this work is based on the open-source CFD code OpenFOAM [3] and it consists of an evolution of a previous model, as reported in [4, 5]. In particular, the modeling approach resorts to a multi-region framework (Fig.42), in which multiple computational grids are adopted to describe the different physical domains, namely: a) the fluid, which describes the gas flow through the system; b) the solid, which

describes the metallic walls constituting pipes and cannings; c) the substrate, which describes the catalyzed porous media (honeycomb or open-cell foam) on which surface reactions take place.

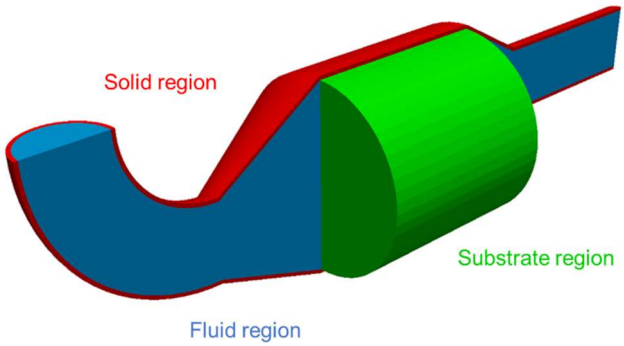

Fig.42: Multi-region framework for after-treatment CFD modeling.

The computational meshes can be adjacent or overlapping: the former is typically the case of the solid metallic wall which bounds the fluid domain while the latter is necessary for describing porous substrates, where the fluid and solid phases coexist in the same zone. This multi-region framework allows to take into account the thermal inertia of the different solid components included in the after-treatment, being metal walls or substrates, making it possible to accurately describe the thermal transient of the system at the cold start of the engine and its effect on the light-off of the catalytic reactions. Since it's not the purpose of the thesis, no further details will be added to the computational setup in this context. However, they can be found in [6].

OpenFOAM was first released as open source by OpenCFD Ltd. in 2004. Since that time it has matured to become the leading open source software for Computational Fluid Dynamics. Therefore, considering its potential in the virtual design and calibration, it surely represents a powerful tool. Furthermore, it doesn't require the purchase of a license, leading to a significant cost reduction in the process.

2.2.2 Experimental set-up

The experimental data for the validation of the computational model were acquired on a test bench specifically designed for the characterization of the thermal transient of the system when the burner is activated. The after-treatment line was instrumented with a set of thermocouples to measure the temperature of the flow and of the metal walls at different locations. As shown in Fig.43, thermocouples were located along the flow path from the burner to the catalyst inlet.

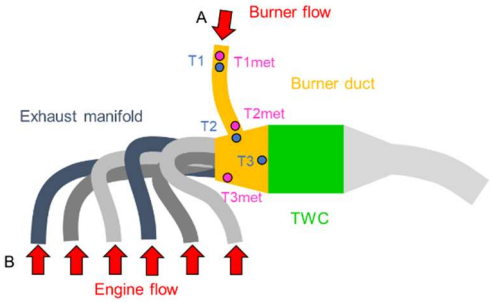

Fig.43: Schematic showing the experimental setup and the thermocouples positions for the measurement of the gas temperature (blue) and of the metal walls (magenta).

2.3 Case study

In this study the after-treatment system for a high-performance V12 engine is considered. The analysis is focused on one single bank and considers the first section of the system including the primary exhaust ducts and the main catalyst. The exhaust line is equipped with a burner which is connected through a dedicated pipe to the inlet cone of the catalyst, in such a way to discharge the hot gas in a section located downstream the exhaust manifold. The analysis of the configuration was performed in two steps: at first, a stand-alone simplified exhaust line (Fig.44.a), specifically designed for thermal assessment and validation, was considered and then the analysis was extended to the full configuration (Fig. 44.b), in order to evaluate abatement performance of the complex system during engine cold start.

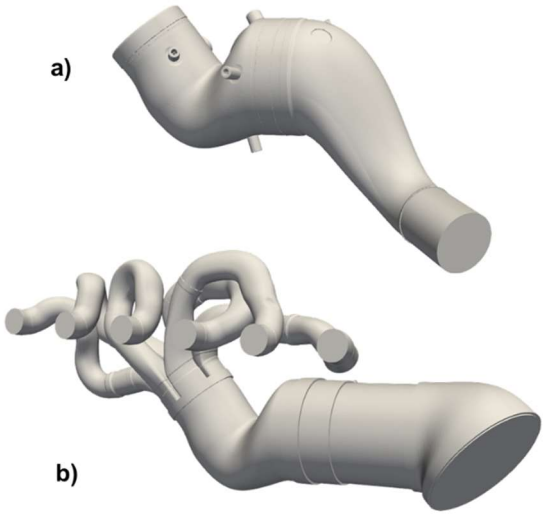

Fig.44: Exhaust line configurations: a) stand-alone experimental test bench; b) full exhaust line equipped with manifold and catalyst

Case A: validation test bench

The reference configuration for the validation consisted in a simplified exhaust line, without manifolds and catalyst. This test bench was designed with the aim to provide an accurate characterization of the flow coming from the burner and directed towards the catalyst inlet section. In particular, the investigation is focused on the characterization of

the flow field, in terms of velocity and temperature distribution and on the analysis of the thermal transient of the metallic walls at different locations.

The CFD model was setup according to the multi-region framework including three different domains: one fluid region describing the exhaust gas flow and two solid regions representing respectively the metallic walls of the pipes and the thermocouples. The accurate modeling of the thermocouples geometry was required in order to directly compare with the temperature measured by the real thermocouples installed on the test bench. As a matter of fact, the detailed description of the thermocouples in terms of geometrical and thermal properties allowed to correctly capture the effects related to the thermal inertia of the probe and the heat transfer phenomena (convective / radiative with the surrounding flow field and conductive along the thermocouple). Moreover, the detailed reconstruction of the thickness of the metallic walls of the exhaust line allowed to take into account their thermal inertia, which has a primary role in the dynamics of the thermal transient at the cold start. The details of the multi-region computational mesh are shown in Fig.45. It has been generated adopting snappy HexMesh, an automatic mesh generator included in OpenFOAM which provides a body fitted grid, predominantly consisting of hexahedral cells, with a small percentage of polyhedral elements near the boundary walls. Hexahedral / prism boundary layers have been added to accurately describe near wall flow and thermal gradients. The overall mesh grid consists of $7.8 \cdot 10^6$ cells, grouped as follows: $5.0 \cdot 10^6$ cells for the fluid region, $2.8 \cdot 10^6$ for the metallic walls and $5.4 \cdot 10^4$ for the thermocouples.

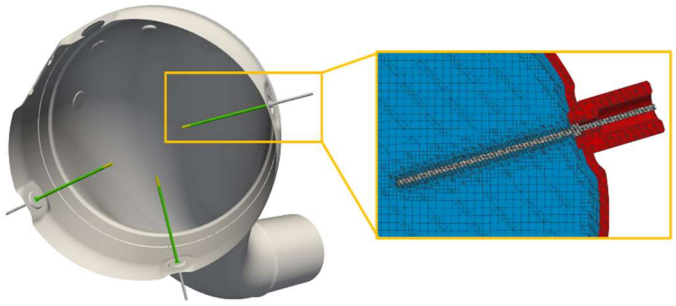

Fig.45: Detail of the multi-region mesh including thermocouple discretization: fluid domain (blue), metal walls solid domain (red), thermocouple solid domain (gray).

The mesh discretization at the fluid walls was able to guarantee a y^+ less than one for all the boundary patches, allowing to employ a low Reynolds turbulence model: hence, the standard k-ω SST turbulence model [6] was applied.

Boundary and initial conditions were imposed on the basis of the experimental measurements performed on the test bench. In particular, at the inlet of the pipe connecting the burner to the catalyst cone (Fig. 43, section A) time-varying experimental conditions of mass flow, temperature and chemical composition were imposed. Moreover, convective heat transfer coefficient between metallic walls and external environment was specified according to experimental estimation. Despite the chemical composition was prescribed at the inlet and the transport of the chemical species was solved by the model, chemical reactions were not taken into account at this stage since the catalyst was not included in the experimental configuration. Moreover, also homogeneous gas phase reactions were not

included in the model, since their rate is negligible at the typical temperature of the exhaust gas.

Case B: full exhaust line

The second configuration considered in the analysis consisted of a full exhaust line equipped with manifold, burner connecting duct and catalytic substrate. The aim of the investigation was to simulate the operation of the after-treatment system at cold start, evaluating at first the heating phase promoted by the activation of the burner and then the subsequent start of the engine.

The computational grid (Fig.46) was generated according to the multi-region framework, including the overlapped substrate region needed for the modeling of the catalyst. The resulting mesh counts $6.6 \cdot 10^6$ cells for the fluid region, $3.1 \cdot 10^6$ for the metal walls and $2.4 \cdot 10^5$ for the substrate.

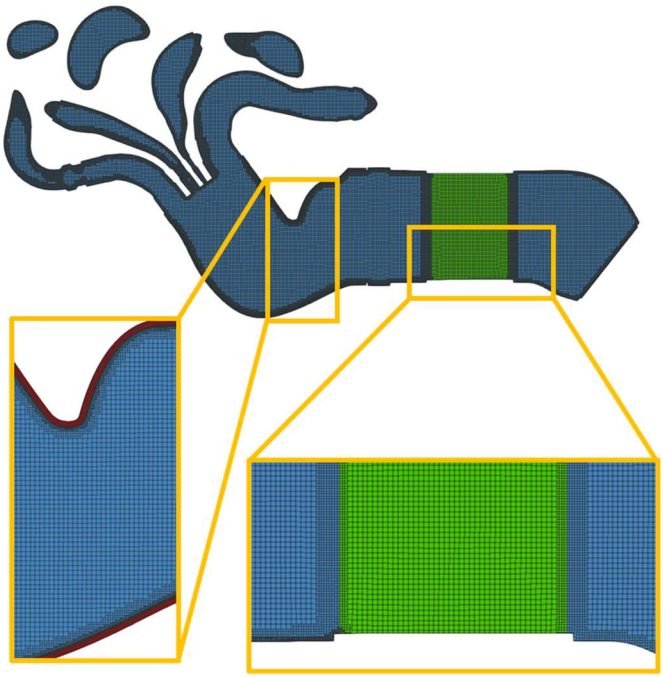

Fig.46: Detail of the multi-region mesh including substrate discretization: fluid domain (blue), metal walls solid domain (red), overlapped substrate domain (green).

The three-way catalyst consisted of a honeycomb ceramic substrate with 800 cpsi and wall thickness equal to 76 μm. Catalytic reactions occurring in the three-way catalyst were described according to the model reported in Table 1, which represents a reasonable starting point when experimental data for the model calibration are not available, as reported in [7].

Table 1. Reaction scheme for the modeling of the TWC.

		$A_{r,i}$	$E_{r,i}$
R1	$CO + \frac{1}{2}O_2 \rightarrow CO_2$	$1.00 \cdot 10^{20}$	$1.00 \cdot 10^{5}$
R2	$H_2 + \frac{1}{2}O_2 \rightarrow H_2O$	$5.00 \cdot 10^{20}$	$1.00 \cdot 10^{5}$
R3	$C_3H_6 + \frac{9}{2}O_2 \rightarrow 3CO_2 + H_2O$	$5.00 \cdot 10^{19}$	$9.00 \cdot 10^{4}$
R4	$C_3H_8 + 5O_2 \rightarrow 3CO_2 + 4H_2O$	$1.00 \cdot 10^{16}$	$1.20 \cdot 10^{5}$
R5	$C_3H_6 + 9NO \rightarrow 3CO_2 + 3H_2O + \frac{9}{2}N_2$	$1.00 \cdot 10^{14}$	$9.00 \cdot 10^{4}$
R6	$CO + NO \rightarrow CO_2 + \frac{1}{2}N_2$	$5.00 \cdot 10^{14}$	$7.00 \cdot 10^{4}$
R7	$H_2 + NO \rightarrow H_2O + \frac{1}{2}N_2$	$5.00 \cdot 10^{15}$	$7.00 \cdot 10^{4}$
R8	$CO + H_2O \rightarrow CO_2 + H_2$	$1.00 \cdot 10^{9}$	$7.00 \cdot 10^{4}$
R9	$CO_2 + H_2 \rightarrow CO + H_2O$	$1.00 \cdot 10^{9}$	$7.00 \cdot 10^{4}$
R10	$C_3H_6 + 3H_2O \rightarrow 3CO + 6H_2$	$9.00 \cdot 10^{11}$	$8.00 \cdot 10^{4}$
R11	$C_3H_8 + 3H_2O \rightarrow 3CO + 7H_2$	$9.00 \cdot 10^{12}$	$1.00 \cdot 10^{5}$
R12	$Ce_2O_3 + \frac{1}{2}O_2 \rightarrow 2CeO_2$	$5.00 \cdot 10^{11}$	$1.50 \cdot 10^{5}$
R13	$Ce_2O_3 + NO \rightarrow 2CeO_2 + \frac{1}{2}N_2$	$3.00 \cdot 10^{13}$	$1.60 \cdot 10^{5}$
R14	$2CeO_2 + CO \rightarrow Ce_2O_3 + CO_2$	$5.00 \cdot 10^{8}$	$1.20 \cdot 10^{5}$
R15	$2CeO_2 + H_2 \rightarrow Ce_2O_3 + H_2O$	$5.00 \cdot 10^{8}$	$1.20 \cdot 10^{5}$
R16	$2CeO_2 + \frac{1}{6}C_3H_6 \rightarrow Ce_2O_3 + \frac{1}{2}CO + \frac{1}{2}H_2O$	$1.00 \cdot 10^{12}$	$1.50 \cdot 10^{5}$
R17	$fCe_2O_3 + \frac{1}{2}O_2 \rightarrow 2fCeO_2$	$3.50 \cdot 10^{10}$	$1.00 \cdot 10^{5}$
R18	$fCe_2O_3 + NO \rightarrow 2fCeO_2 + \frac{1}{2}N_2$	$5.00 \cdot 10^{12}$	$1.00 \cdot 10^{5}$
R19	$2fCeO_2 + CO \rightarrow fCe_2O_3 + CO_2$	$5.00 \cdot 10^{8}$	$8.00 \cdot 10^{4}$
R20	$2fCeO_2 + H_2 \rightarrow fCe_2O_3 + H_2O$	$5.00 \cdot 10^{8}$	$8.00 \cdot 10^{4}$
R21	$2fCeO_2 + \frac{1}{6}C_3H_6 \rightarrow fCe_2O_3 + \frac{1}{2}CO + \frac{1}{2}H_2O$	$5.00 \cdot 10^{8}$	$8.00 \cdot 10^{4}$
R22	$2fCeO_2 + \frac{1}{7}C_3H_8 \rightarrow fCe_2O_3 + \frac{3}{7}CO + \frac{4}{7}H_2O$	$2.00 \cdot 10^{6}$	$8.00 \cdot 10^{4}$

The simulation was run considering a cold start condition in which at first the burner is activated for 20 s and then the engine is started. Flow boundary conditions were imposed at the inlet of the burner duct (Fig.43, section A) and of the manifold (Fig.43, section B) prescribing instantaneous mass flow, temperature and concentration of the chemical species. All the other parameters were maintained the same as described in the previous section.

2.4 Results and Discussion

Simulations were run at first on the simplified configuration mounted on the experimental test bench to validate the model in terms of fluid-dynamics and heat-transfer. Then, the full exhaust line is considered and simulations are run in order to characterize the conversion efficiency of the system in a cold start condition in which the burner is activated before the start of the engine.

Fluid-dynamics & Thermal analysis

The validation of the model was assessed considering the simplified configuration mounted on the experimental test bench (case A). The instantaneous temperature of the flow at the inlet of the connection duct, which is located immediately downstream the burner, was available from experimental measurements and was imposed as boundary condition for the model (Fig.47, temperature T0). The temperature T0 shows a rapid transient towards the regime value, which is reached after 5 s. In a similar way the mass flow from the burner was imposed in the model as constant during the activation time. The fluid temperature measured experimentally was compared with the temperature estimated by the model on the basis of the detailed reconstruction of the thermocouples. This allows to directly estimate the temperature of the metal sheath in correspondence of the joint of the thermocouple, enabling the possibility to directly compare with the temperature value provided by the real probe. As a matter of the fact, the "virtual" thermocouple takes into account the thermal inertia and the conductivity of the probe, while the conjugate heat transfer model accurately describes the convective and radiative heat flux exchanged with the fluid domain.

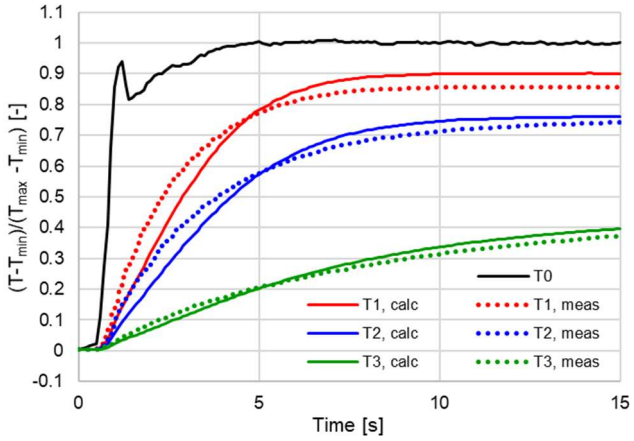

Fig.47: Temperature of the exhaust gas at different locations: validation of the calculated data against experimental measurements. Data are non-dimensionalized with respect to minimum and maximum temperature.

The comparison between calculated and measured temperature can be regarded as satisfactory (Fig.47), both in terms of description of the thermal transient and prediction of the regime temperature. The three probes are located along the flow path between the inlet and the catalyst section (as detailed in Fig.43) and describe the progressive cooling of the burner exhaust gases before reaching the catalyst. Small differences are present regarding the behavior of thermocouples T2 and T3 within the 5s, where slightly differences in thermocouples position from the CAD one, transient flow resolution or thermocouples properties might affect the CFD solution. However, this difference is contained within tenth of a second shift and negligible considering a 15s maneuver. The progressive wall heat up is mainly due to the convective heat transfer between the gas flow and the pipe walls, which are progressively heated increasing their temperature starting from the initial cold condition. The thermal heating of the metallic walls is characterized in Fig.48, where experimental and calculated solid temperatures are compared at three different locations.

Also in this case thermocouples are distributed between the burner connection and the catalyst location, in such a way to describe the temperature non-uniformity of the metallic walls (Fig.43). The comparison shows a good agreement between measurements and calculations. It can be noticed that the temperature of the metal walls is increasing progressively due to the heat transferred from the fluid; however, the final value reached in the considered time interval (15 s) is significantly lower than the fluid temperature and is far from the regime condition. This is mainly due to the thermal inertia of the metallic walls: in this phase, heat accumulation is largely predominant over the external convective heat transfer towards the environment.

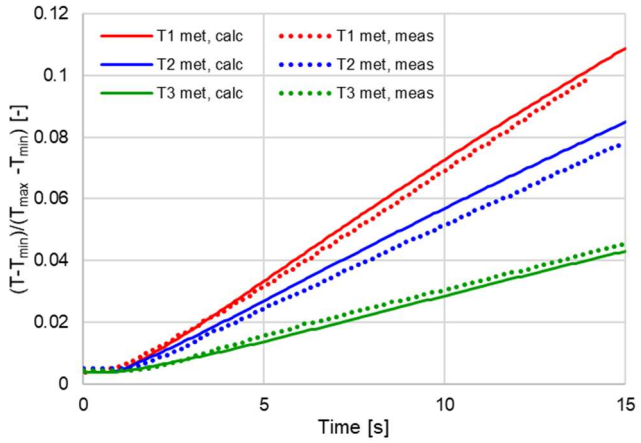

Fig.48: Temperature of the metal walls at different locations: validation of the calculated data against experimental measurements. Data non-dimensionalization is the same as Fig.49.

As further analysis, the role of the radiative heat transfer is evaluated. Fig.49 reports the comparison of the numerical estimation of the thermocouple temperatures when the radiative heat transfer model is disabled. It can be noticed that the larger differences are found at the highest temperatures, where the contribution of the radiative heat transfer is significant. In particular, for the first probe location (T1) it can be seen that the radiative heat transfer is the main responsible for the reduction of the probed temperature at regime condition with respect to the inlet value. On the other hand, at lower temperature (e.g. probe T3) the effect of radiative heat transfer becomes negligible.

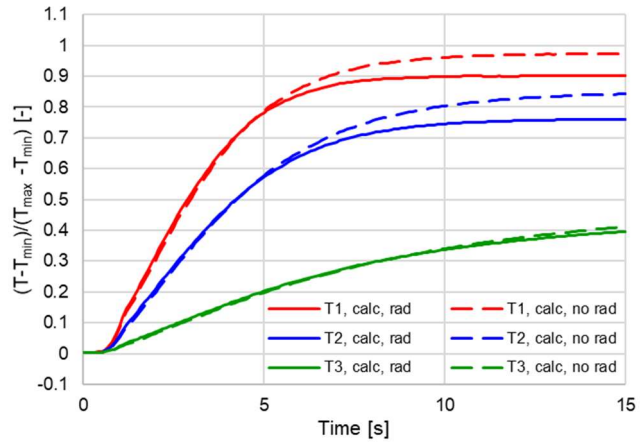

Fig.49: Comparison of the temperature of the exhaust gas calculated with and without radiation model.

In Fig.50 the temperature distribution in the section where the catalyst should be placed (A) and in two other sections downstream (B, C) is reported. The section A is close to the position of the thermocouple T3 discussed with reference to the previous graphs. The temperature field shows a certain degree of non-uniformity, related to the fact that the configuration adopted here for the validation of the model has not been optimized yet. However, from the validation point of view, this test condition is significant because it shows the capability of the model of predicting the non-uniform flow distribution, as assessed by the combination of the information coming from thermocouple T3 (which experiences the lower temperature) and the wall thermocouple T3 met (which measures the temperature of the wall in contact with the flow stream characterized by the highest temperatures).

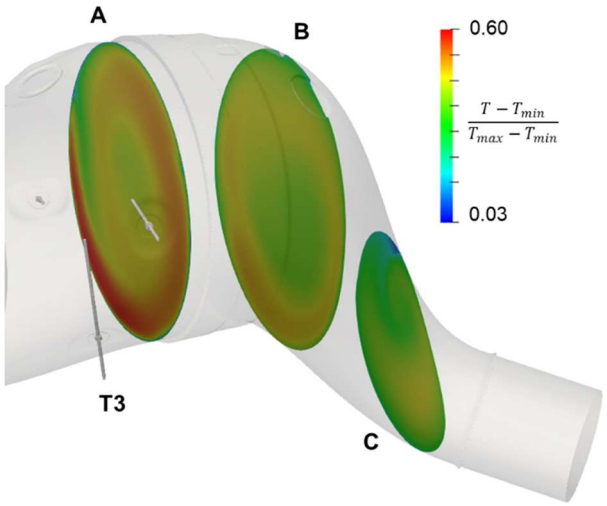

Fig.50: Flow temperature distribution downstream the inlet cone for the catalyst (not included in the test bench configuration) for time 10 s.

Full cold-start analysis

After the first validation step, the CFD model was applied for the investigation of a full cold start transient with burner activation and subsequent start of the engine. Even though the experimental data were not available for this specific tested condition, the numerical analysis was performed on the basis of the data available from the experimental characterization of the burner out (as described in the previous section) and of the engine out (as measured in configurations without burner). Time-dependent boundary conditions were applied at the inlet of the burner duct and of the exhaust manifold. The tested condition considers a first heating step, in which the burner is activated for 20 s, and a subsequent phase in which burner is deactivated and the engine is started. Simulation is run for total 50 s.

Fig.51 shows the temperature and velocity fields on a transversal section of the system 10 sec after the engine start. It can be seen that the flow coming from the exhaust manifold is cooled due to the heat exchanged with the pipe walls, while a high temperature region can be noticed in the second half of the catalyst. This high temperature zone is the result of the previous heating of the substrate due to the burner activation. On the other hand, the lower temperature in the first section of the substrate is due to the cooling associated to the

cold flow coming from the engine during the cranking phase. The temperature distribution inside the substrate determines also the non-uniform flow velocity along the catalyst axis, which is related to the different gas density.

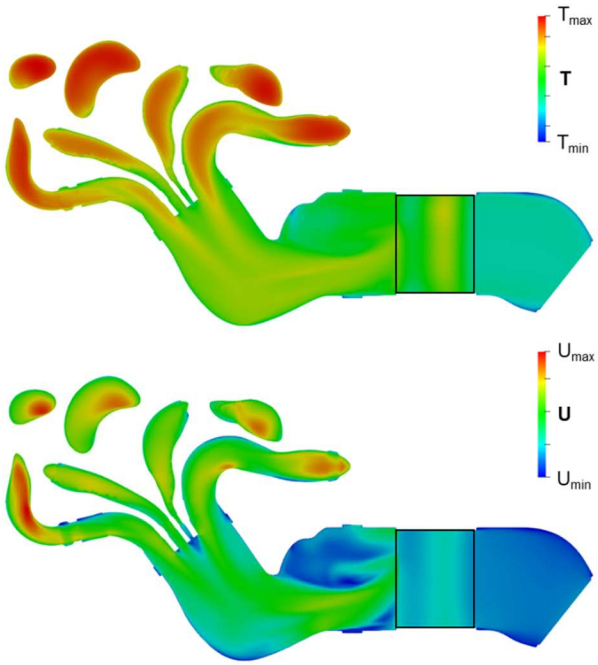

Fig.51: Temperature and flow condition at 30 s (10 s after the engine start) for a transversal section of the ATS including the TWC (highlighted with black line).

The tracking of the pollutant chemical species for the same time (10 s after the engine start) is reported in Fig.52. At this time, the temperature of the substrate is already sufficient to enable the light-off of all the catalytic reactions, determining a significant abatement of the pollutants in the first part of the TWC. Moreover, the low engine mass flow during the start condition contributes to the efficiency of the overall abatement.

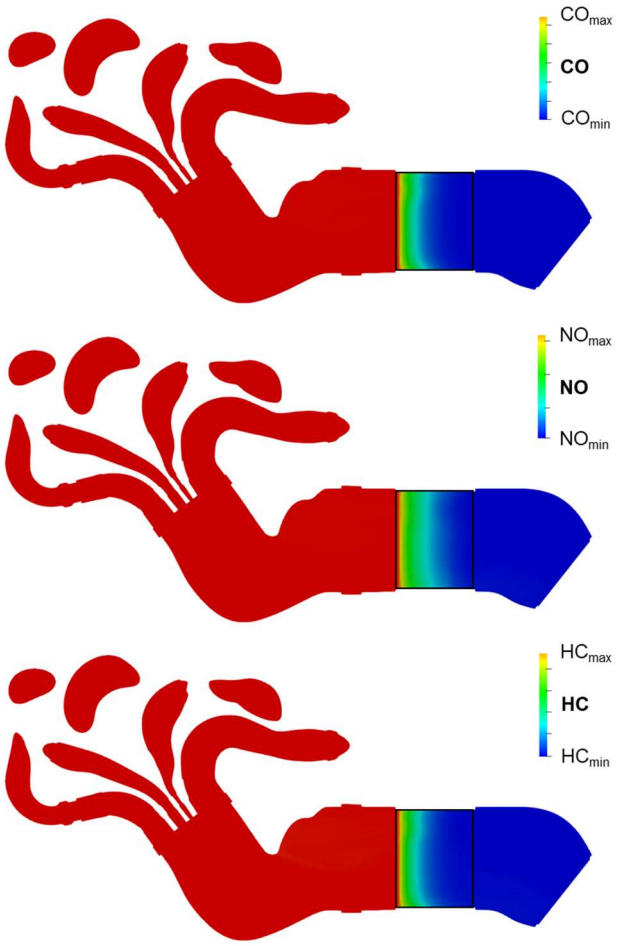

Fig.52: Pollutants mass fractions at 30 s (10 s after the engine start) for a transversal section of the ATS including the TWC (highlighted with black line).

The temperature of the substrate during the cold start transient is monitored in Fig.53, where four different locations are considered along the catalyst axis. During the activation of the burner (time < 20 s) the temperature of the substrate is rising with different rates for the different locations: the heating is quite fast for the first section at the catalyst inlet, while it takes more time as the location is moved downwards. The thermal inertia of the substrate plays a key role, influencing the extension of the zone where the temperature reaches a sufficient value for the light-off of the reactions. In this phase, the conversion of the pollutant emissions from the burner is not a crucial point, as can be seen in the next plots: as a matter of fact, the CO and HC emissions are negligible, since the burner is operated in lean condition, while the NO_x emission can be controlled quite effectively even if the reactions are active only in a restricted portion of the catalyst. After 20 s, when the burner is turned off and the engine is started, the substrate temperature shows a reduction due to the cooling effect of the exhaust gas flow from the engine, which has a low temperature during the cranking phase. The cooling takes place with a certain time delay passing from the inlet location and moving forward to the downstream probe locations. Then, in the next few seconds, the exhaust gas temperature starts to increase, even if slowly due to the cooling effects of the cold metallic walls. However, the increase of the exhaust gas temperature is enough to determine the heating of the substrate temperature in the first section which was

subjected to the strongest cooling. Moreover, exothermic catalytic reactions start to take place in the zone where the temperature is higher, contributing to a further increase of the substrate temperature. This effect is evident after 35 s, when the temperature of the substrate in the central part and second half portion of the TWC reaches a higher temperature with respect of the inlet section.

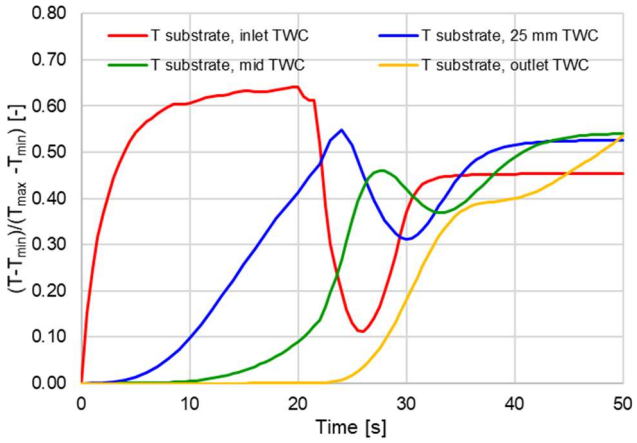

Fig.53: Solid temperature evolution in different locations along the axis of the substrate: inlet section of the TWC, 25 mm downstream the inlet section, mid section, outlet section.

Cumulative emissions, Fig.54-55-56, show a trend which is consistent with the substrate temperature evolution described so far. For all the pollutants, the most critical phase is in the range 20-30 s, when the engine starts and the exhaust gases exhibit a low temperature which has a cooling effect of the substrate. Then, the activity of the catalyst increases in the range 30-50 s, even if different abatement levels are registered for the different pollutants: at 50 s the CO abatement is > 99%, NO is around 97%, HC around 76%. The lower abatement level reached by HC is due to the higher light-off temperature required by the catalytic abatement of this pollutant.

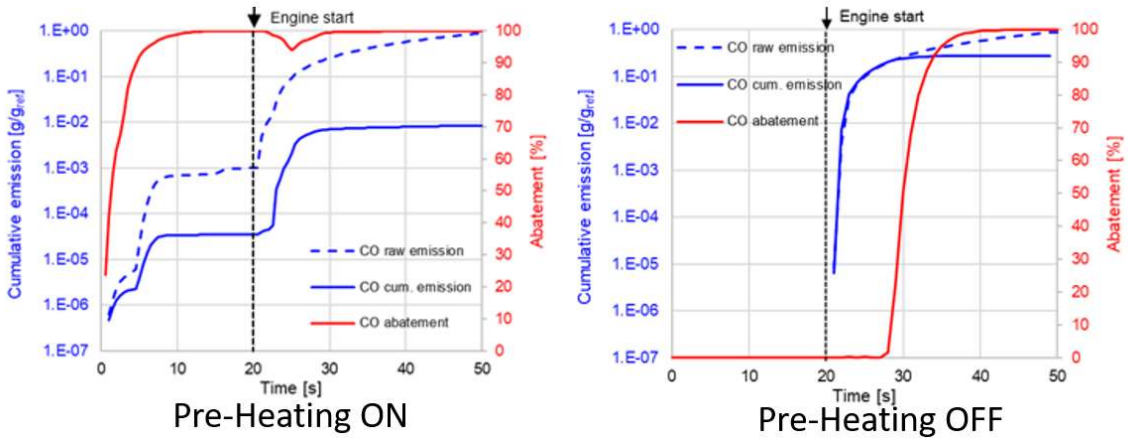

Fig.54: Evolution of the CO emission during the engine cold start with burner activation: cumulative emission (blue line) and conversion efficiency (red line).

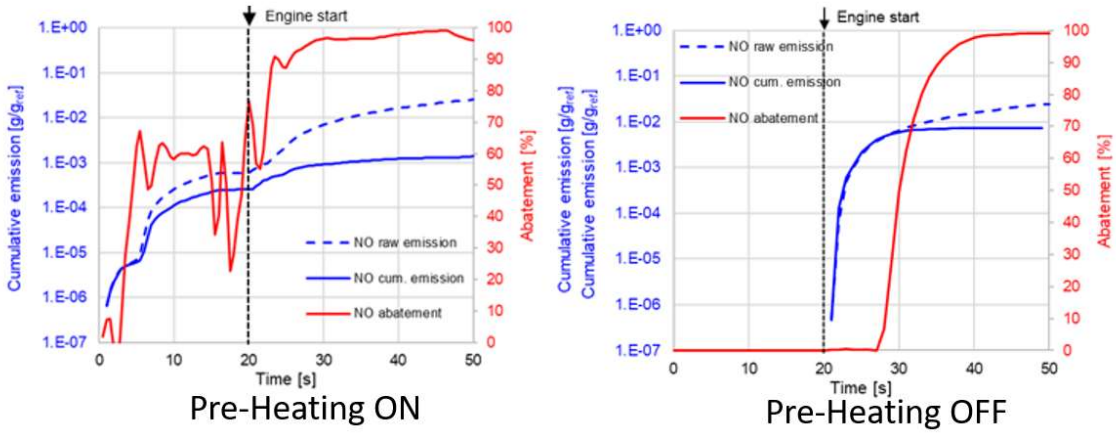

Fig.55: Evolution of the NOx emission during the engine cold start with burner activation: cumulative emission (blue line) and conversion efficiency (red line).

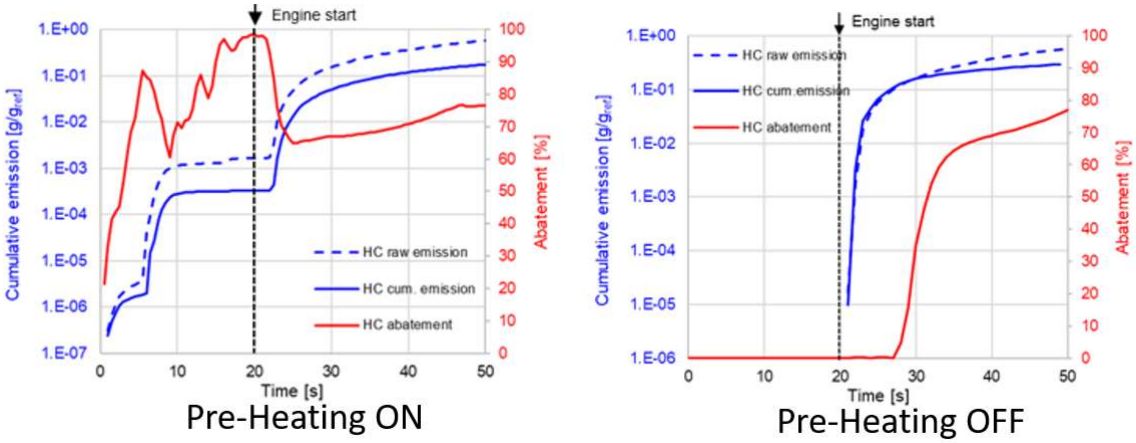

Fig.56: Evolution of the HC emission during the engine cold start with burner activation: cumulative emission (blue line) and conversion efficiency (red line).

A quantitative comparison between pre-heating mode ON and OFF is also shown in Fig. 54-55-56 among the species. It needs to be reminded that the overall effect on emission species is still a preliminary investigation where the burner design and strategy were not yet optimized, still the absolute advantage can vary depending on the engine architecture and exhaust line layout. In order to do not provide misleading numbers, the conversion efficiency is deemed the key parameter to be judged against kW required by a generic pre-heating system over absolute tailpipe emissions.

At the time of this evaluation, what we can say from the experimental evidence (it was not the scope of this 3D study), the fuel consumed from the burner does not relevantly change the CO2 impact from an engine standpoint since the catalyst heating strategy can be reduce from a current application. Again, this aspect is still confidential and subject to a continuous development that strongly depends from engine to engine.

The evolution of the substrate temperature field during the cold start of the engine is reported in Fig.57. Time 21.5 s shows the starting temperature distribution when the burner is deactivated, which exhibits a maximum temperature in correspondence of the inlet section of the catalyst. Then, in time range 22.5 – 27.5 s, the exhaust gas flow coming from

the engine, which is characterized by low temperature due to the heat exchange with the cold metallic walls of the manifold, determines a significant cooling of the substrate. In particular, the cooling is more significant for the zone near the inlet section, while the highest temperature region is progressively moved downstream. For time > 30 s, the temperature of the exhaust gas starts to increase while, at the same time, the exothermic reactions with lower activation energy (i.e. CO oxidation) are occurring in the zones characterized by the highest temperature. This results in a progressive light-off of the catalyst starting from the central part of the substrate.

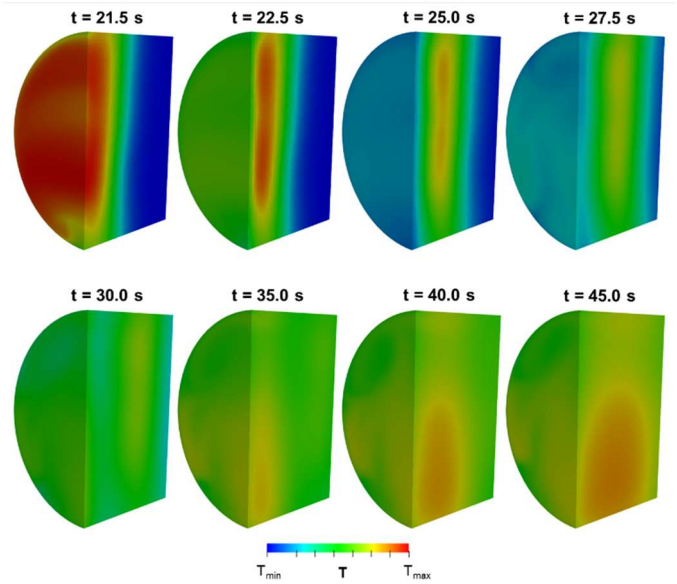

Fig.57: Solid temperature evolution in the substrate during the engine cold start.

The simulation of the full exhaust line was run in parallel employing 4 to 28 processors, applying domain decomposition on all the three regions, and exhibiting a good scalability. The overall computational runtime for simulating 50 s was around 130 h on 28 processors.

2.5 Conclusions

In this chapter an after-treatment system including a burner as heating device has been studied applying a numerical modeling approach. The main findings and conclusions of the work are hereafter summarized:

1. A comprehensive CFD numerical model has been used for the simulation of the exhaust after-treatment system. The model, based on a multi-region approach for the description of the different domain (fluid, metal walls, substrates, thermocouples) allows the detailed description of the heat-transfer phenomena between the regions (including: conduction, convection and radiation), allowing an accurate prediction of the transient heating of the device at cold start. Moreover, a catalyst model based on quasi steady-state assumption is implemented, allowing to consider arbitrary reaction schemes for the modeling of the surface reactions. This solution algorithm allows to keep the computational burden low, in such a way to

make it possible the simulation of relatively long time intervals (in the order of minutes / hours) also exploiting massive parallelization. These aspects make the developed simulation methodology particularly interesting for the design of the next generation ATS in view of the upcoming Euro 7 legislation, as numerical optimization tool to be applied to support and guide the experimental tests.

2. Experimental activity performed on a dedicated test bench was exploited for the validation of the CFD model. Moreover, the combination of experimental data and simulation results allowed to obtain additional information about the operation of the burner and its effects on the heating of the after-treatment. The analysis confirms that the thermal inertia of the metal walls plays a primarily role in the cooling of the gas from the burner during all the burner heating phase. Furthermore, the model confirms that at high temperature it is important to consider heat transferred by radiation, which has a significant influence on the measured gas temperature.

3. A complete after-treatment line, equipped with burner and catalyst, was simulated considering a full cold start transient. The tested condition included the burner heating phase and the subsequent start of the engine, describing the light-off of the catalytic reactions. The simulation shows that the burner is an effective solution for the speed-up of the thermal transient, increasing the temperature and so the abatement efficiency of the catalyst before the engine starts. However, the simulation pointed out that the early phase of the engine start can be critical, since the exhaust gas is subjected to a strong cooling due to the interaction with the cold manifold. This determine a cooling of the catalyst, which was previously preheated by the burner. However, a hot region in the mid of the catalyst is preserved, giving a significant spur to the light-off of the reactions when the concentration of the pollutants in the exhaust gas increased.

4. The results shown in this chapter, obtained by means of a numerical investigation, should be regarded as a promising starting point for the development and the implementation of this solution on the vehicle. However, it should be remarked that, currently, the burner catalyst technology is still at a research stage: further studies and investigations are needed to evaluate its actual potential for production cars.

Chapter 3

Modeling soot and gaseous emissions in 3D-CFD in-cylinder simulations of spark-ignition engines: a methodology to correlate numerical results and experimental data

3.1 Introduction

Internal combustion engines are of critical importance to transportation and hence global energy demand, and are projected to remain so for years to come. Achieving high energy efficiency and at the same time low levels of pollutant emissions are therefore key drivers of development.

To achieve the target, engine manufacturers take advantage of different techniques such as downsizing together with turbocharging (leading to the increase of specific power mentioned above) [1, 2], gasoline direct injection (GDI) [3, 4], complex fuel injection strategies (to exploit charge stratification benefits) [5-7], variable valve timing [8, 9], innovative combustion and ignition processes [10, 11] and water injection [12]. Moreover, the possibility to hybridize vehicles cannot be ignored [13-15], which is de facto an increasingly widespread solution. Besides the benefits, they introduce drawbacks which cannot be neglected. For example, the use of globally lean stratified charge makes the use of 3-way catalytic converters obsolete for the reduction of NO_x. This requires, in turn, the addition of a further device such as a NO_x storage catalyst [16-18], increasing complexity and cost of the after-treatment.

Among all the technological advances accomplished for internal combustion engines (ICE), gasoline direct injection (GDI) engines hold practical potential to achieve a substantial improvement. In a GDI engine, the fuel is pressurized and injected via a common rail fuel line system directly into the combustion chamber of each cylinder as opposed to the more conventional multi-point port fuel injection (PFI). The incorporation of direct injection strategy into a spark-ignition engine offers several advantages including enhanced fuel economy, minimized pumping loss, higher compression ratio, reduced knock tendency and improved transient response. GDI engines are becoming the most widely used gasoline engines attributed to their superior efficiency compared with traditional PFI engines. Unfortunately, the particle emissions are higher for GDI engines, and it is difficult for the manufacturers to control the particle mass and number. Therefore, a gasoline particulate filter (GPF) has to be included in the exhaust line [19, 20]. Additionally, the fine particles, especially the ones with the size less than 2.5 nm (known as PM2.5), have adverse health effects. Characterized by diameters of less than 100 nm, the airborne ultra-fine particles emitted have been found to affect the respiratory health of adults severely. Furthermore, particle deposition along the respiratory tracts leads to elevated risks for development of asthma or pulmonary inflammation. Consequently, it comes as no surprise

that progressively more stringent emission legislations are being implemented to monitor the engine-out exhausts.

In Europe, a 5 mg/km (3.1 mg/mi) PM emission limit for GDI engines took effect in 2009 with the Euro 5 standard. The first restrictions for particulate number (PN) emissions—considered more difficult to achieve than PM targets—come into effect this year with Euro 6. The latter initially limits PN totals to 6×10^{12} number/km, and then in late 2017 falls an order of magnitude to 6×10^{11} number/km.

For the future days, the picture is becoming more and more complicated with the introduction of Euro7 emission standards, and so a new challenge arise for the automotive industry.

In 2017 the EU introduced new requirements, requiring all new vehicles to pass both the new laboratory test and (the Worldwide harmonized light vehicles test procedure – WLTP) and the new on-road Road Driving Emissions (RDE) test. RDE testing is carried out using portable emissions measurement systems (PEMS). It is important to distinguish WLTP testing from RDE testing – the former is carried out to determine whether levels of regulated pollutants are below the given limits, as well as to provide official CO2/fuel consumption (FC) figures, while the latter focuses on a narrow range of pollutant emissions and does not produce CO2/FC results of any legal relevance. The aforementioned procedures (WLTP and RDE) share certain similarities (e.g. commencing from cold start urban driving). The specifics of the two test types are very important, especially the total distance covered and the distance covered under low-speed (urban) conditions before higher speeds (rural, highway) are encountered for the first time since powertrain startup. The WLTP procedure is based around its near eponymous speed trace, the Worldwide harmonized light vehicles test cycle (WLTC), which commences with 3.08 km of urban driving, followed by three further phases of monotonically increasing mean (and maximum) velocity. RDE testing must consist of three phases (rural, urban, motorway), which must occur in that order. However, each of those phases must cover at least 16 km (and they normally cover significantly more distance, in order to meet other RDE requirements) and thus powertrain behavior can differ very strongly between the two test types.

Thus, in order to keep the benefits offered by GDI engines and to meet the strict emission standards simultaneously, in-depth knowledge of complex engine phenomena especially soot processes occurring within GDI engines is crucial; above all, it is necessary to determine the source of particles in GDI engines and how take measures to reduce the particle emissions.

In this complex scenario, CFD tools play a fundamental role. They can be proficiently adopted to estimate engine efficiency, optimize injection [23] and cooling strategies [24, 25], investigate alternative combustion [26, 27] and ignition [28] technologies, evaluate the effect of water injection [29-32], prevent knock [33-35] and thermo-mechanical failures [36] and, finally, predict tailpipe emissions [37]. In the last decade CFD codes have undergone a massive development to offer improved modeling for gaseous and, mostly, solid pollutants.

While traditional combustion diagnostics including pressure-based combustion analysis and engine-out emissions measurements provide quantitative data of in-cylinder events in

GDI engines, 3D CFD tools can support engine design providing reliable estimations of tailpipe emissions. In particular, in-cylinder simulations are able to evaluate formation of both Soot and gaseous pollutants inside the combustion chamber. In the last decade, given the increasing interest on emissions simulation, a strong improvement of CFD models has been pursued, mostly for Soot. In particular, attention has been largely focused on the inclusion of chemistry calculations.

One of the main critical issue in such kind of simulations is the validation against experimental findings. In fact, the complexity of emissions measurements does not allow a straightforward one-to-one comparison between numerical results and experimental evidence.

Comparison against experiments is not straightforward. In fact, complex methods and instruments are usually adopted, whose characteristic outputs are sometimes far from typical simulations results. In other words, an ad-hoc post-processing of simulation outcomes is needed to make them comparable to experiments. In the present manuscript, a detailed methodology to correlate numerical and experimental outcomes is proposed for both gaseous and solid tailpipe emissions, that is for CO, CO_2, NO_x, HC and Soot.

The methodology described hereafter aims at providing both a robust numerical framework to obtain reliable estimations of the pollutants and an approach to process simulation outputs.

The Sectional Method is specifically tailored to account for the specific chemistry of the adopted fuel, which is represented by a fuel surrogate built to match the sooting tendency of the tested gasoline [38]. As for the latter, it is based on a detailed analysis of the instruments principle to understand how they handle the exhaust gas. The proposed methodology is validated against experiments carried out on a high performance turbocharged GDI engine, operated at different low revving speed part-load conditions. The main difference between the operations consists in the start of injection (SOI), whose variation is expected to determine noticeable differences in the fuel distribution inside the combustion chamber.

3.2 Engine, Investigated Conditions and Experimental Apparatus

3.2.1 Engine Overview and Operating Conditions

A direct injection spark ignition (DISI) turbocharged engine is investigated, whose main characteristics are reported in Table 2.

Table 2. Main engine characteristics.

Engine Type	V8
B/S	>1
Total Displacement	>3500 cm^3
Number of Valves / cyl	4
Maximum Injection Pressure	>300 bar
Brake Specific Power	>>150 CV/l

The engine has a 90° angle between the cylinder banks, aluminum block and heads. The forced induction system uses two parallel twin-scroll water-cooled turbochargers and two air-to-air intercoolers. The valve-train consists of four valves per cylinder actuated through roller finger followers by two overhead camshafts per bank. The engine features gasoline direct injection and continuously variable valve timing on both intake and exhaust side as well as dry sump lubrication.

The engine is experimentally analyzed at part-load low-revving speed condition, characterized by BMEP and revving speed equal to 2 bar and 2000 rpm, respectively.

Different injection timings are investigated. Specifically, start of injection (SOI) varies from 130 °CA bTDCF to 300 °CA bTDCF. Such a wide sweep of SOI leads to large variations in charge stratification. Moreover, liquid film formation and mixture cooling are affected as well. As a consequence, in order to fix BMEP (with a tolerance of ±2.5%) despite SOI shift, slight modifications of the engine calibration are needed at each condition by adjusting the electronic control unit, so the coefficient of variation (COV) was maintained below 3% during the measurement and sampling process. Fuel consumption, airflow rate and spark advance undergo variations lower than 5%. While the formers decrease anticipating the injection start, the latter increases. For all the conditions mixture is nearly stoichiometric, i.e. equivalence ratio ϕ=1 (±2.5%). This is confirmed by air and fuel flow rates and oxygen sensor at the exhaust.

Four conditions are numerically investigated, hereafter referred to as SOI 150, SOI 175, SOI 200 and SOI 245. They are characterized by injection start equal to 150, 175, 200 and 245 °CA bTDCF, respectively. These conditions are purposely selected as, on the one hand, they offer a wide variation of the SOI and, thus, of the stratification, leading to non-negligible differences in emissions production (mostly in terms of Soot). On the other hand, highly anticipated SOIs ($\gg$245 °CA bTDCF) are discarded to prevent massive fuel deposits on the piston head. In fact, liquid film leads to diffusive flames and non-negligible increase of particulate. Therefore, efforts and attentions have to be dedicated to its modeling and validation to achieve a reliable estimation of emissions. The selected set of experiments offers an interesting test case for the validation of emission-related numerical procedures and models.

3.2.2 Combustion Performance Indicators

Besides test bench results in terms of combustion performance and emissions, a comprehensive experimental data set on the adopted GDI injector is available. This will be presented afterwards, in the section dedicated to the Lagrangian spray model validation. Focusing on engine performance, experimental pressure is measured for each single cylinder via a high-sensitivity dynamic pressure transducer with a very small sensor size manufactured by Kistler. It is a piezoelectric sensor working with pressure up to 250 bar and characterized by a natural frequency higher than 200 kHz. Experimental in-cylinder pressure traces adopted in the results section represent, for each single cylinder, an ensemble average over more than 300 cycles. Moreover, an additional curve is shown for

each condition, representing averages among the cylinders to obtain a representative pressure trace of the engine, which is the one adopted for combustion simulation calibration. For each condition the overall curve is then exploited to obtain MBF50%, burn duration (10-90%) and IMEP. Specifically, as for the first two combustion indicators, they are obtained converting pressure trace into apparent heat release rate (AHRR) following Eq. 1.

$$\frac{dQ}{d\theta} = \frac{\gamma}{\gamma - 1} p \frac{dV}{d\theta} + \frac{1}{\gamma - 1} V \frac{dp}{d\theta} \quad (1)$$

3.2.3 Soot Particle Number and Gaseous Emissions Concentrations at the Exhaust

Experimental data are available on both solid and gaseous emissions. In particular, as for the first, Soot particle number (PN) is measured via the AVL Particle Number Counter (PNC).Thanks to a dedicated tailpipe measurement kit, consisting in a hole probe and a heated pipe, Soot is sampled directly from the exhaust port few millimeters downstream the engine head. Such sampling line is heated in order to prevent deposits and it sends exhaust gas to the Volatile Particle Remover (VPR) which allows the vaporization of volatile particles inside the Evaporation Tube (ET). In addition, VPR ensures a sufficient dilution ratio (DR) which, on the one hand, lower particles concentration below the maximum limit tolerated by the PNC (namely 10˙000 #/cm^3) [39]; on the other hand it decreases gas temperature below the limit given by the United Nations regulations of 35 °C [40]. Experiments used in the present activity are characterized by a dilution ratio of nearly 5000:1. Finally, particles enter the PNC in which a photo-sensor detects scattered light pulses generated when particles pass through a laser beam produced by a diode. Output of the PNC is the so-called Particle Number (PN), which is a particle concentration [#/cm^3] referred to standard conditions (273.2 K and 101.33 kPa). Legislation rules both the accuracy (±10% over a wide range of particles concentrations) and the efficiency at small diameters. As for the latter, according to the Particle Measurement Program (PMP), detection efficiency levels ensured by the PNC are resumed in Table 3. In particular, at 23 nm (±1nm) counting efficiency achieves 50%. Such brief and schematic description of the PNC is needed to point out some aspects playing a crucial role in the comparison between 3D-CFD simulation results and experimental outcomes. As it will be shown in the results section, for a fair comparison, numerical particle concentrations have to undergo the same dilution (PND1*PND2), they have to be referred to standard conditions and, finally, it is necessary to account for efficiency of the instrument.

Table 3. AVL PNC Efficiency.

Efficiency	Diameter
10%	16.4 nm
25%	18.5 nm
50%	22.2 nm
90%	34.9 nm

Concentrations of gaseous emissions are measured via the MEXA 7170 produced by Horiba [41], suitable for raw sampling. It exploits different principles, based on the pollutant to be estimated. For CO and CO_2 the Non Dispersive Infrared Detector (NDIR) is adopted, in which the exhaust gas flows in a cell and it interacts with an infrared radiation. CO and CO_2 concentrations are proportional to the infrared light adsorbed by the gas molecules. NO_x are estimated via a Chemiluminescence Detetcor (CLD). In this case, NO_x are converted to NO at first. Then the latter flows in a chemiluminescence reaction chamber where, along with ozone, it forms electrically excited Nitrogen dioxide which immediately reverts to the ground state emitting photons. Light intensity is measured by a photodiode detector. Finally, for UHC, the Flame Ionization Detector principle is adopted. In this case exhaust gas flows through a flame obtained by combustion between chromatographic air and a mixture of Hydrogen and Helium. Any hydrocarbons in the sample will produce ions when they are burnt. Ions are detected using a metal collector which is biased with a high DC voltage. The current across this collector depends on the UHC concentration in the sample gas.

As it will be discussed in the results section, numerical-experimental comparison is easier in this case. In fact, for all the analyzed gaseous emissions, neither dilution nor efficiency have to be accounted for. Outputs are simply provided in terms of volume concentrations, specifically %vol for CO and CO_2 and ppm(v) for NO_x. The only critical issue regards UHC, whose unit is slightly different, i.e. ppmC3. The reason is twofold. Firstly, "C" indicates that values represent nor volume neither mass fractions [42]. The output signal is merely proportional to the number of Carbon atoms present in the gas. In particular, "3" implies that signal is proportional to the one provided by a mixture of Propane (C_3H_8). In fact, the instrument is calibrated replacing the exhaust gas with a mixture of Propane and Nitrogen in a given proportion (that is mixture ppm(v) is known). When calibration ends, burnt gases flow into the FID system. The latter is only a Carbon atoms counter, thus measured current intensity and the deriving output signal in case of burnt gases are proportional to the original values obtained during calibration. Constant of proportionality is equal to the ratio between the Carbon contents of the burnt gases and the Propane-Nitrogen mixture. If exhaust gas has a carbon content higher than the C_3H_8/N_2 mixture, factor is higher than 1 and output signal is higher than the original value. The opposite happens if the exhaust gas Carbon content is lower. Since FID is completely insensitive to the presence of Hydrogen, output signal cannot be considered neither a volume fraction (i.e. ppm(v)) nor a mass measurement. For this reason, ppmC is used. To

be precise, a number has to be specified, that is it can be ppmC_1 or ppmC_3 based on the Carbon content of the gas adopted for calibration. In this case Propane is used, thus signal value is expressed as ppmC_3. It is useful to point out that ppmC_1 can be obtained from a value in ppmC_3 simply multiplying the latter by factor of 3. One the one hand, this prevents the possibility to obtain exact mass or volume fractions for UHC from experiments. On the other, it complicates the comparison against simulations results, as it will be shown in the results section.

In the Fig.58 is reported a small sketch where all the emission species are obtained after the exhaust line before the turbine.

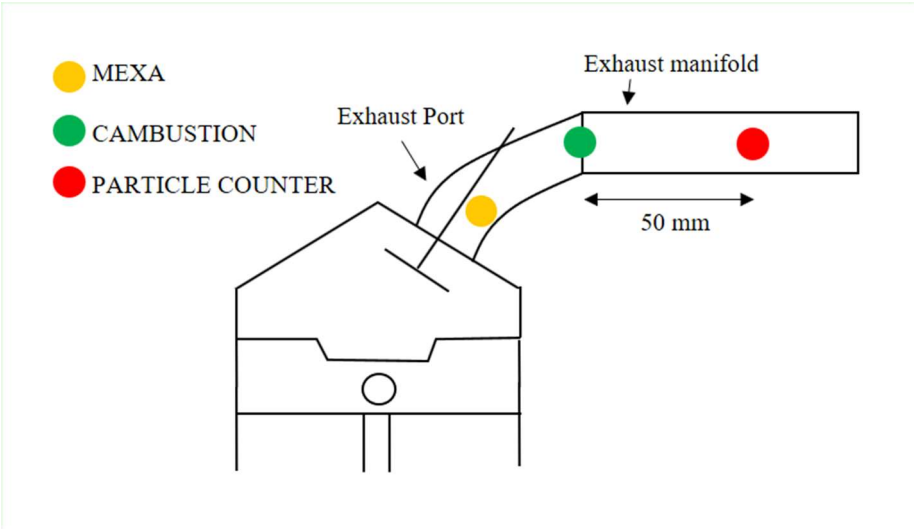

Fig.58: Instruments locations after the exhaust valve and before the turbine.

It is interesting to point out two different aspects. Firstly, gaseous and solid emissions tailpipe measurements are carried out on different cylinders to allow simultaneous measurements while accommodating the instruments in the available space. As a consequence, hereafter, calibration of numerical combustion will refer to the average of the cylinders rather than to a single one. Secondly, besides measurements are as close as possible to the engine head, probes are placed downstream along the exhaust line as well, specifically just before the oxidation catalyst. Fig.59 shows a comparison between data coming from the different locations. For brevity only PN and NO_x are reported but the same considerations are valid for all the other gaseous emissions. Minor differences can be noticed from data comparison. This confirms that, because of gas expansion at EVO (and, thus, related temperature drop), reactions can be considered as “frozen”. Therefore, when comparing simulation and experimental outcomes, the adoption of numerical particle concentrations at EVO seems to be reasonable.

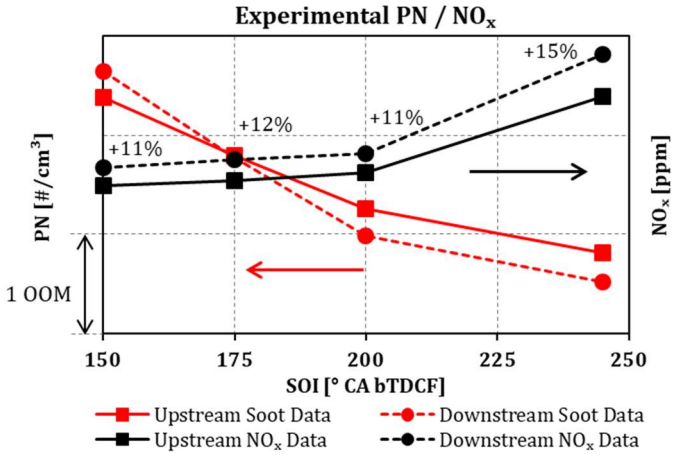

Fig.59: Comparison, in terms of Soot and NO_x between measures carried out at different locations

3.3 Numerical set-up

3.3.1 3D Model

3D-CFD simulations are carried out with STAR-CD v4.30, licensed by SIEMENS DISW [44]. Turbulence is approached via the $k-\varepsilon$ RNG model for compressible flows [45], widely diffused for in-cylinder simulations in the engine community. Ideal gas equation of state is adopted to close the set of RANS equations. Viscosity is a function of temperature and modeled by the Sutherland's equation. Specific heat and thermal conductivity are still temperature dependent but, in this case, expressed as polynomial functions. Non-slip condition is imposed at solid walls and temperature is fixed, whose value depends on the specific boundary and it is obtained from a combination of experimental evidences and structural analysis results. Despite there may be critical aspects on the use of laws of the wall [46, 47], the near-wall flow is modeled via a high-Reynolds approach to save computational cost, thus wall functions are adopted both for velocity and thermal boundary layers. As for the first, a standard law of the wall is adopted. As for the second, the GruMo-UniMORE thermal wall function proposed by the authors in previous publications [48, 49] is preferred, as validated on engines similar to the one of the present activity. Computational domain includes cylinder and in-head portions of intake and exhaust ports. Geometrical symmetry is exploited, thus only half of the domain is simulated in order to reduce the computational effort. Therefore, extensive quantities (such as number of particles [#]) in the result section refer to half of the chamber. PISO solution algorithm and second order MARS numerical scheme are adopted for momentum, temperature and turbulent quantities transport equations. Time dependent pressure and temperature boundary conditions are derived from a GT-Power 1D model, provided with phenomenological models for turbulence and combustion [50-52] and extensively validated against experimental measurements. Since differences between the operations are limited, a unique set of boundary conditions is adopted for all the simulations. For the same reason, an equal injected fuel amount is considered. Only spark-advance (SA) slightly differ (of less than 5%) for the cases, similarly to experiments. Time dependent pressures and temperatures at intake and exhaust ports adopted in the 3D in-cylinder simulations refer to

one of the cylinders where experimental emission measurements are performed. As for the spray, a combined Eulerian-Lagrangian approach [53] able to properly account for both the vessel gaseous ambient and the dispersed liquid phase is adopted, whose details are described in the next paragraph where validation of the spray model is proposed. Senda's approach [54] is included to manage the interaction between droplets and walls and the evaluation of the Leidenfrost temperature, which liquid film formation depends on, is entrusted to the Habchi model [55]. Combustion is modeled via ECFM-3Z [56], as it was widely validated in previous publications on similar engines [57-59]. ECFM-3Z is a general-purpose combustion model capable of simulating the complex mechanisms of turbulent mixing, flame propagation, diffusive combustion and pollutant emission formation that characterize modern internal combustion engines. It is based on a flame surface density (Σ) transport equation which governs the turbulent premixed flame propagation. In order to account for the local thermodynamic state and composition of the mixture, laminar flame speed is included in Σ equation. In order to improve the fuel chemistry modeling thus enhancing predictive capabilities of the combustion model, a dedicated part-load laminar flame speed correlation is provided via user subroutine [60, 61]. In the present activity ignition is mimicked via deposition of an initial spherical flame kernel [44], whose deployment is then governed by Σ equation.

Part of ECFM-3Z is devoted to post-flame reactions and emissions modeling. This allows to account for diffusive combustion as well as formation of tailpipe emissions, included Soot. Since the latter is modeled via empirical correlations in ECFM-3Z, the advanced "Sectional Method" available in STAR-CD package is preferred. A wider description of emissions modeling can be found in the next paragraphs. End of simulation (EoS) corresponds nearly to the Exhaust Valve Opening (EVO), in order to increase the consistency between EoS in-cylinder emissions and measured data. A flow chart of the numerical procedure is proposed in Fig.60. Firstly, soot library for Sectional model is obtained via 0D chemical kinetic calculations and spray is validated in 3D-CFD quiescent vessel simulations. Afterwards, 3D-CFD in-cylinder analyses are run and combustion is calibrated against experimental data if needed. Multiple cycles are run to eliminate the influence of the initial condition and to obtain a fully converged solution for each of mixture, liquid film and emissions, which means that the difference between results of two consecutive cycles is minimized.

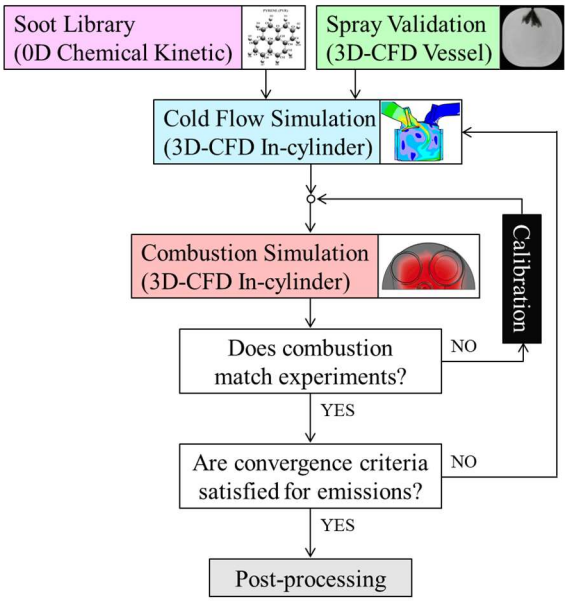

Fig 60: Flow chart of the numerical procedure.

3.3.2 Spray model

A detailed validation of the Lagrangian spray model is carried out in a quiescent vessel. In particular, injection pressure and temperature as well as back pressure and vessel temperature considered for the validation are similar to the actual conditions experienced during the engine operations. For the spray calibration, a comprehensive set of experimental data is available. In particular, the injection rate reported in Fig.61 is supplied by hydraulic characterization, while imaging in a quiescent vessel provides information on both spray morphology and jet penetration. PDA (Phase Droplet Anemometry) measures diameter and velocity of the droplets. Finally, momentum map returns information on spray pattern and cone angle of each plume.

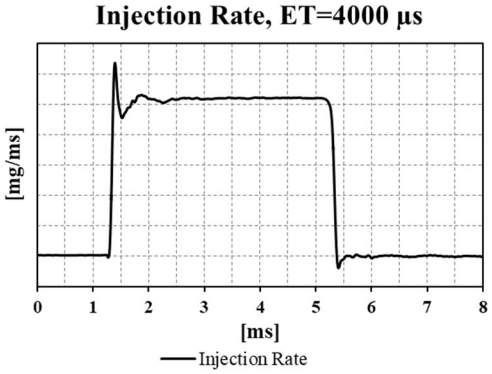

Fig.61: Experimental injection rate for the adopted injection pressure and an excitation time of 4000 µs.

As for the secondary break-up, the model proposed by Reitz [66] is used, whose constants are similar to the ones available in the reference paper. Fuel is single-component and properties are user-coded and provided by the fuel supplier.

The computational domains consist in the block-shaped geometry shown in Fig.62, whose characteristic dimensions are 220x220x128 mm. All the boundaries are modeled as non-slip walls and temperature is fixed equal to the ambient one.

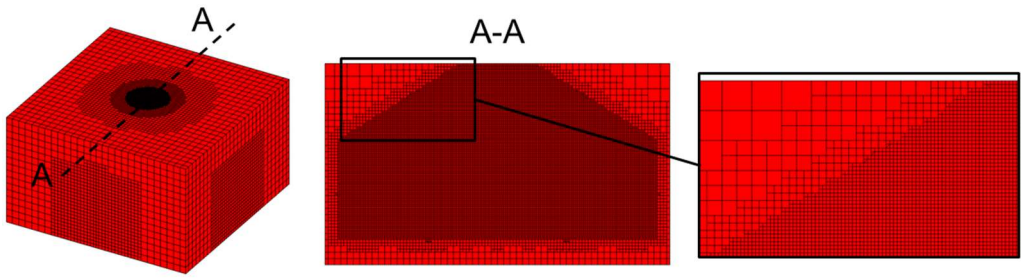

Fig.62: Adopted computational mesh. Besides the whole domain, a section along with a detail is reported.

Some of the main outcomes of the spray validation are reported in Fig. 63. In particular, Fig.63a) shows a comparison in terms of imaging between simulation and experiments, for both front and side view. Morphology and liquid penetration of the spray are properly reproduced, as confirmed by the joint observation of Fig.63a) and Fig.63b), which shows liquid penetration curves. Fig. 63c) represents the difference from numerical droplet diameter with the experimental counterpart resulting from PDA (where a common high pressure GDI falls in the range on 15-25 micros). For the sake of confidentiality, difference between numerical and experimental values is reported. Even in this case, the difference is minimized which means that break-up phenomenon is properly represented by simulation.

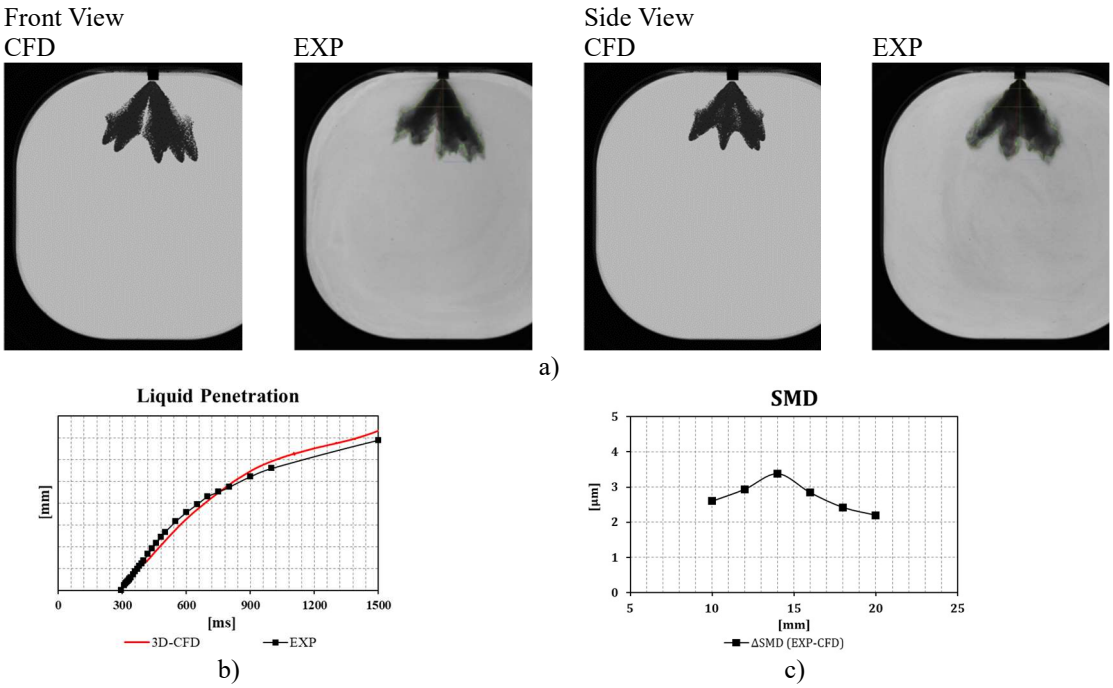

Fig.63: a) CFD and experimental imaging at 700µs after start of injection; b) liquid penetration; c) difference in terms of SMD between simulation and experiment, at 30 mm from the injector tip.

3.3.3 Gaseous Emissions Models

To understand how gaseous emissions are obtained from simulations, the description of ECFM-3Z needs to be extended. The model is based on the wrinkled flamelet assumption, i.e. turbulence can corrugate the flame front. The mixing model divides each computational cell involved in the combustion process in three zones, as visible in Fig.64.

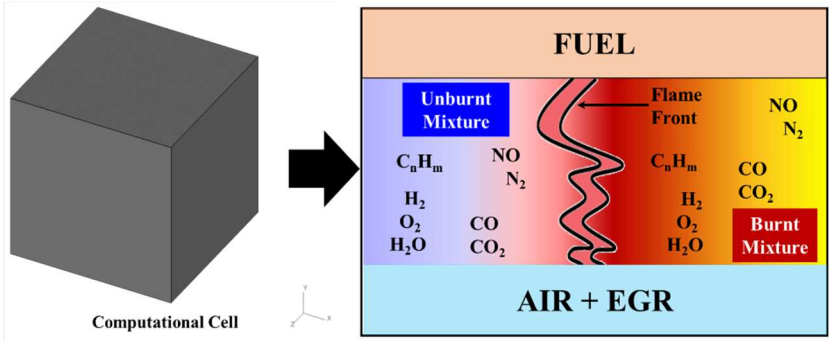

Fig.64: Schematic representation of the combustion model in a representative computational cell.

The zone in the center is essential for emissions modeling. In fact, species such as unburnt hydrocarbons (UHC), carbon monoxide (CO) and dioxide (CO_2), nitrogen oxides (NO_x) and Soot originate in this region.

Then, any species in the burnt mixture region can take part to further reactions (such as dissociation and radical formation reactions involving species assumed to be at equilibrium and not containing carbon atoms), formation of CO_2 from CO, formation of NO_x and Soot chemistry.

NO_x formation is described by a multi-step reaction mechanism involving radical species. Nitrogen oxides chemistry is modeled with the three-step Zeldovich mechanism, whose reactions are reported in Table 4.

Table 4. Three-step Zeldovich mechanism for NO_x formation.

$O + N_2 \Leftrightarrow N + NO$
$O_2 + N \Leftrightarrow O + NO$
$N + OH \Leftrightarrow H + NO$

Fuel may be present in the burnt gas zone for two reasons: either the fuel evaporates in that region, or the oxygen is the deficient species; thus fuel in the burnt gases or even in the unburnt ones that remains up to EVO in the combustion chamber can be regarded as UHC.

3.3.4 Sectional Soot Method

Several approaches have been developed in the last years to tackle soot formation modeling. One of the most advanced and diffused models is the Sectional Method, thoroughly discussed by [69-71]. It allows the direct description of the soot particle size,

without any a priori assumption on the distribution function, which makes it one of the most promising CFD models to numerically evaluate particulate production in GDI engines. The Sectional Method relies on a volume-based discretization of the soot particle size together with conservation of soot mass and number density. Soot content in each computational cell is divided into a fixed number of sections based on the soot particle diameter. In other words, each section contains spherically shaped soot particles characterized by the same diameter and, thus, by the same representative volume. Soot particle density has the same value regardless the particle size. The model solves a transport equation, namely Eq. 10, for the soot mass fraction in each section. Sections provide the local soot mass fraction distribution and thus, also, size distribution, number density and mean diameter of the particles.

$$\frac{\partial \bar{\rho}\,\widetilde{Y}_{soot,i}}{\partial t} + \nabla \cdot \left(\bar{\rho}\,\tilde{u}\,\widetilde{Y}_{soot,i}\right) = \nabla \cdot \left(\bar{\rho} D_{soot,t} \nabla \widetilde{Y}_{soot,i}\right) + \rho_{soot}\widetilde{\Omega}_{soot,i} \qquad for\ i = 1{:}\,i_{max} \quad (10)$$

The model includes all the phenomena that can lead to particle formation and evolution: physics-based phenomena (nucleation, condensation, and coagulation) and chemistry-based mechanisms (surface growth and oxidation). More specifically, soot formation begins with fuel pyrolysis and oxidation reactions: acetylene and other soot precursor species are formed based on mixture quality and thermodynamic state of the system. The polycyclic aromatic hydrocarbons (PAHs) are the gas phase precursors that produce, via nucleation, a solid soot particle. The new nucleated particles are stored in the first section, which is the only section where the particle inception contribution is accounted for in the source term. Larger particles can be formed from smaller ones via coagulation (which accounts for inter-particle collisions) or via condensation (of the PAHs on the particle surface). Particle size evolution is also affected by two chemistry-dominated phenomena, namely surface growth and oxidation, leading to increase and reduction of the particle size, respectively. In Eq. 10, the overall source term $\widetilde{\Omega}_{soot,i}$ for section i is computed as the sum of individual source terms as in Eq. 11. Each one is related to a specific soot formation or evolution contribution: particle inception, coagulation, condensation, surface growth, and oxidation.

$$\widetilde{\Omega}_{soot,i} = \widetilde{\Omega}_{PI,i} + \widetilde{\Omega}_{COND,i} + \widetilde{\Omega}_{COAG,i} + \widetilde{\Omega}_{SG,i} + \widetilde{\Omega}_{OX\,i} \qquad \text{with } \widetilde{\Omega}_{PI,i}|_{i\neq 1} = 0 \quad (11)$$

The sectional method has been extensively validated for Diesel engines, whereas its application for soot prediction in GDI engines is a recent practice. Since soot formation is highly correlated to both combustion mode and fuel chemical nature, the extension of the Sectional Method to GDI engines should be carefully validated.

In this study, the fuel chemical nature is taken into account providing customized inputs for the computation of the source terms adopted in the soot mass fraction transport equations. Such inputs are tabulated values of the reaction rate coefficients: $\widetilde{RPAH}$, that describes the gas-phase precursors rate of formation, $\tilde{k}_d$ and $\tilde{k}_{rev}$ that influence the surface growth, $\tilde{k}_{O_2}$ and $\tilde{k}_{OH}$ that affect the oxidation process. Each coefficient is tabulated as a function of independent variables, in particular unburnt temperature, pressure, equivalence ratio, dilution, and combustion progress variable. The CFD solver reads the tabulated

values corresponding to the cell-wise values assumed by the independent variables. To compute the above coefficients, combustion in a 0D homogeneous constant pressure reactor is simulated via chemical kinetics calculations, carried out using DARS v4.30 [73]. Detailed chemical kinetics simulations are solved "offline" with respect to 3D full-engine cycle simulations. Stored values are recalled by the Sectional Method when source terms computation in Eq. 11 is carried out. Workflow describing information exchange between the Soot library and the 3D-CFD tool is shown in Fig.65.

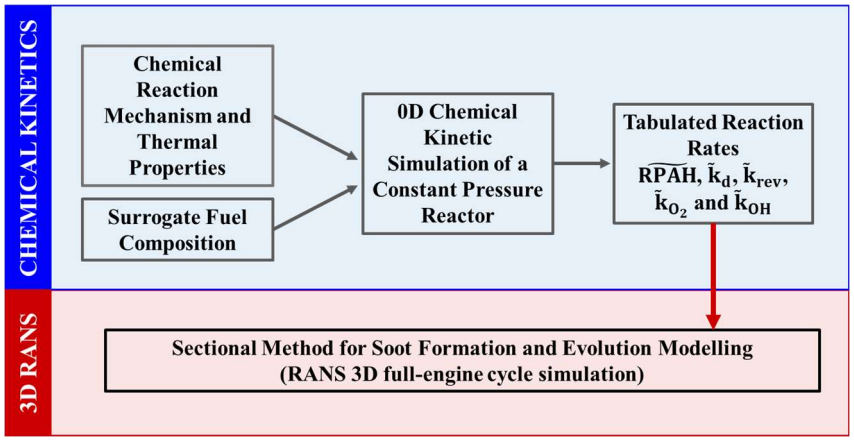

Fig.65: Input and output flow diagram describing the offline chemistry interaction with 3D-CFD simulations.

Chemical kinetics simulations are carried out at the engine-relevant conditions using the reaction scheme developed by Cai et al. [74], derived from the one proposed by Blanquart et al. [75]. This mechanism focuses on the PAH formation and, besides a detailed description of hydrocarbon oxidation, it also includes the ethanol pathways, thus it is suitable for oxygenated gasoline surrogate fuels.

Along with the reaction mechanism, fuel composition is an essential input to chemical kinetic simulations. Gasoline is a complex mixture of several hydrocarbon species and it would be computationally unfeasible to simulate the exact composition. An effective strategy to cope with this problem is the formulation of a surrogate fuel that matches the most important properties. In this study, RON, MON, H/C and O/C ratios as well as the Threshold Sooting Index (TSI) are actively targeted solving an over-determined equations system with the methodology reported by Del Pecchia et al. [38]. To account for the oxygenated content, ethanol is added to the Toluene Reference Fuel (TRF) to obtain an E-TRF (Ethanol Toluene Reference Fuel), whose final properties and composition are reported in Table 5 and 6 respectively.

Table 5. Surrogate properties.

	RON	MON	H/C	O/C	TSI
Ref.	98	88	1.895	0.037	-
Surr.	96.2	89.1	1.919	0.017	14.65

Table 6. Surrogate composition.

Composition			
Ethanol	Toluene	N-heptane	Iso-octane
11.50 mol%	30.51 mol%	10.80 mol%	47.19mol%

3.4 Results

3.4.1 Combustion Validation

Besides secondary effects such as trapped mass variations, the main consequence of a SOI sweep is a large modification of the mixture distribution inside the combustion chamber which, in turn, leads to a considerable difference in terms of flame front propagation and tailpipe emissions. Thus, before moving into details of the combustion analysis, a focus on charge stratification at combustion onset is mandatory. Despite the very similar mean mixture quality between the SOI, significant variations locally emerge.

In the Fig. 66 is compared equivalence ratio for the different SOI (on equal °CA) just before spark. With the very delayed SOI, namely 150 °CA bTDCF, a rich zone is formed on the intake side. In particular, two rich spots are visible, near the symmetry plane and on the upper periphery respectively. On the opposite side, close to the cylinder liner, mixture is much leaner than stoichiometry. The same pattern is visible also for the other SOIs. However, progressively anticipating the injection start, mixture distribution becomes more homogeneous and mixture gradients decrease.

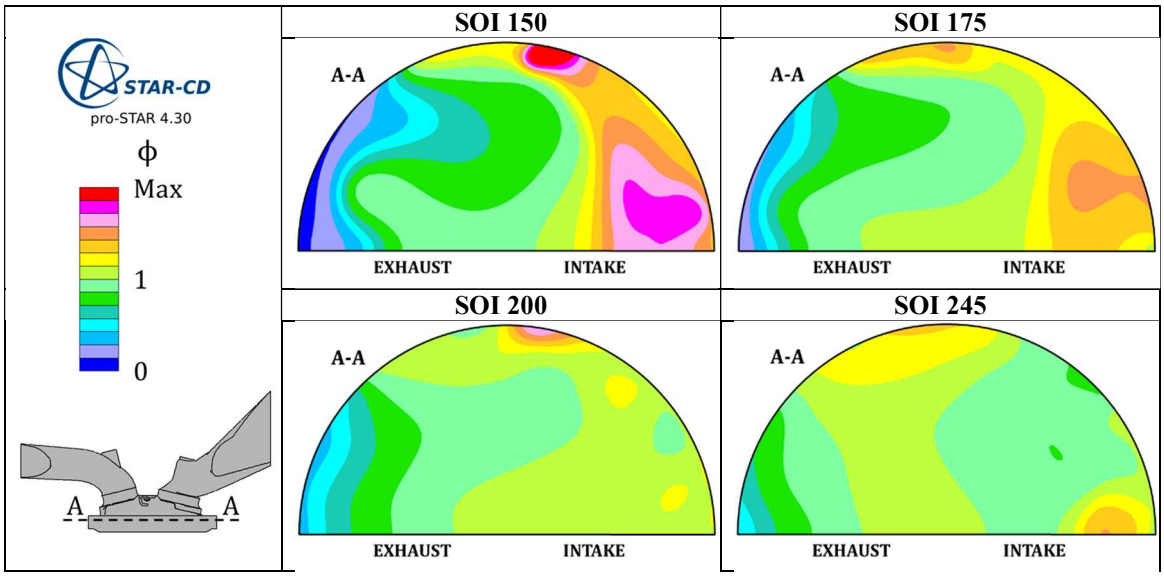

Fig.66: Equivalence ratio before combustion onset (the same °CA is considered for all the cases). Sections are normal to the cylinder axis and 0.1 mm below the cylinder head.

Figs. 67a) to 67d) show, on equal combustion calibration (regardless small variations of the SA of ±2°CA according to test bench data), a comparison between simulations and experiments in terms of mean in-cylinder pressure and AHRR. Focusing on simulation results (red curves), pressure progressively increases moving from SOI 150 to SOI 245. The reason is related to ϕ distributions discussed above. For very advanced SOIs, mixture is more homogeneous leading to an increase of the laminar (and, thus, of the turbulent)

flame speed. Comparison with experiments reveals that the effect of SOI sweep is mildly overestimated. While, for the very delayed injection, numerical pressure and AHRR are slightly underestimated, for the very anticipated SOI case the result is opposite, with an over-prediction of the same quantities. This is confirmed by combustion indicators shown in Figs. 68a) and 68b), expressed as difference between numerical and experimental values. For the very delayed SOI (150 °CA bTDCF), very lean and rich zones present in the combustion chamber lead to an overestimation of combustion duration and resulting IMEP is lower than the expected value. Conversely, for the very anticipated injection case (SOI 245), 10-90% reduces compared to the experimental counterpart thus IMEP is slightly over-predicted.

Despite differences between 3D-CFD and experimental outcomes, the effect of a SOI modification is fairly captured and the overall agreement can be considered as satisfactory, mostly remembering that no case-by-case ad-hoc tuning in terms of combustion model and ignition sub-model parameters is carried out. Moreover, as suggested by MBF50% in Fig. 68c), combustion phasing is properly matched by simulations. Difference is less than 0.5 CA for all the analyzed SOI. Therefore, attention can move to tailpipe emissions, whose discussion is demanded to the following paragraph.

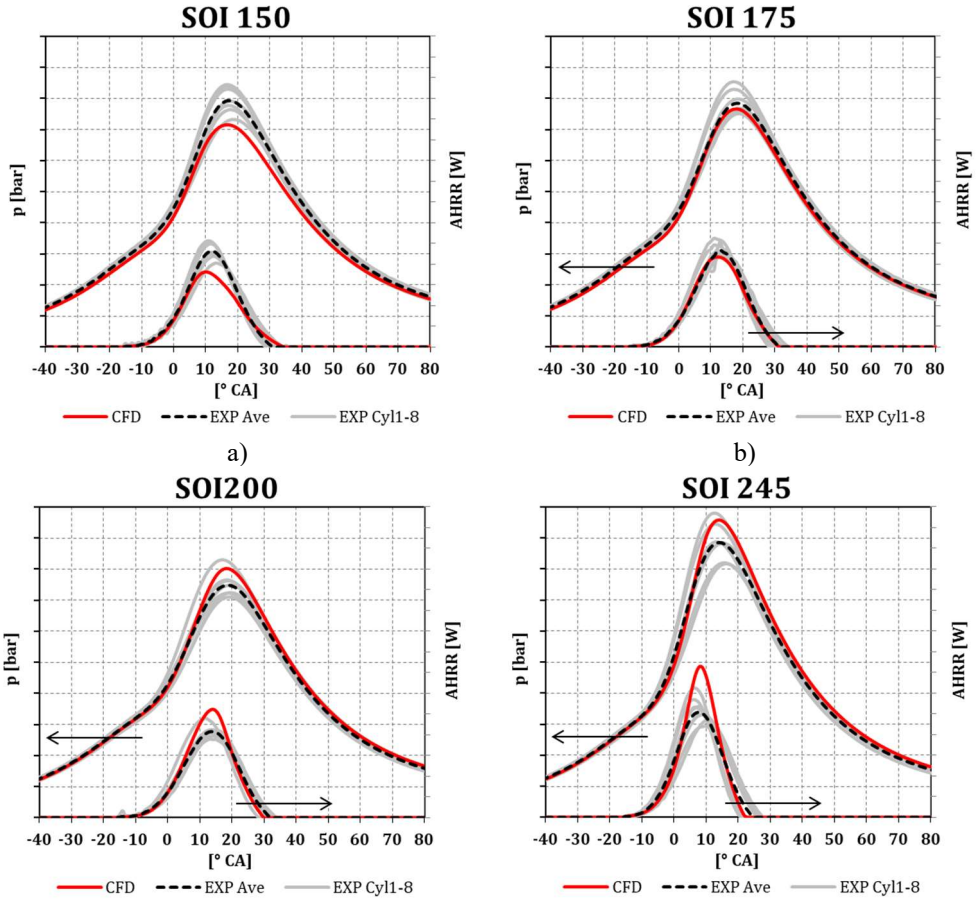

Fig.67: Mean in-cylinder pressure and apparent heat release rate provided by both simulations and experiments. Scales of p and AHRR are common for all the graphs.

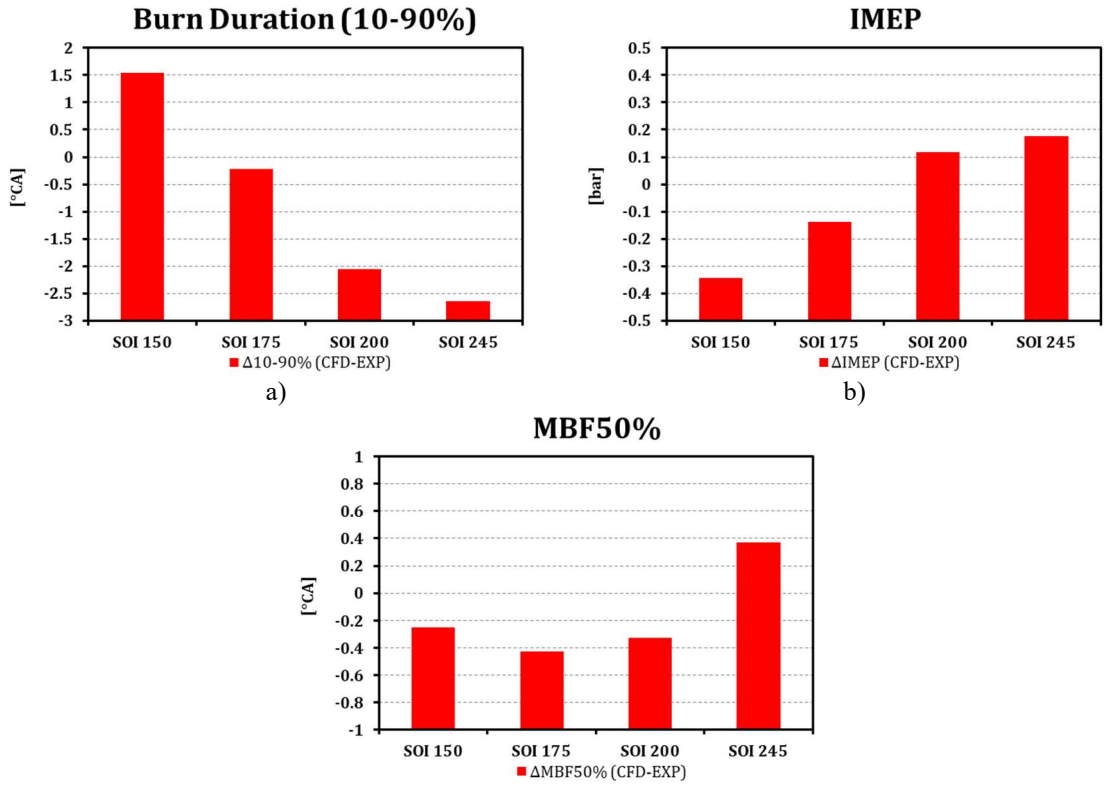

Fig.68: Numerical-experimental comparison in terms of combustion indicators, namely Burn Duration (a), IMEP (b) and MBF50% (c).

3.4.2 Numerical-Experimental Comparison on Pollutant Emissions

Once combustion is validated against experiments and multiple cycles are run to obtain a converged solution in terms of emissions (i.e. cycle-to-cycle variations at EVO are negligible), pollutants can be finally compared to the experimental counterparts. It is useful to point out that, to reduce uncertainties, units adopted in the numerical-experimental comparisons are the original ones of the instrument, so that conversions are avoided. Moreover, for each condition, results proposed hereafter come from the last simulated cycle. Starting from Soot and focusing on the numerical side, Fig.69 shows the number of generated particles, which is noticeably higher for SOI 150 and it progressively decreases anticipating the start of injection. This is confirmed by contour plots in Fig.70, where Soot mass fraction is reported for all the investigated cases at 30 °CA aTDCF.

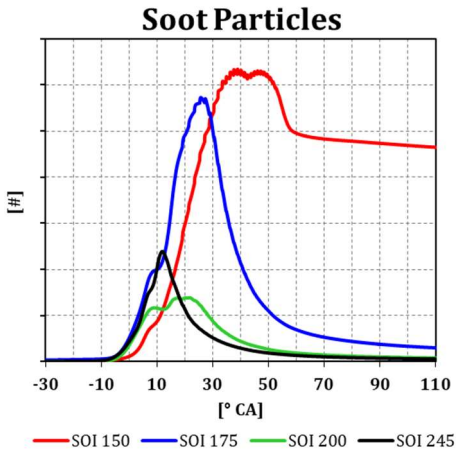

Fig.69: Number of Soot particles for the last simulated cycle (linear scale).

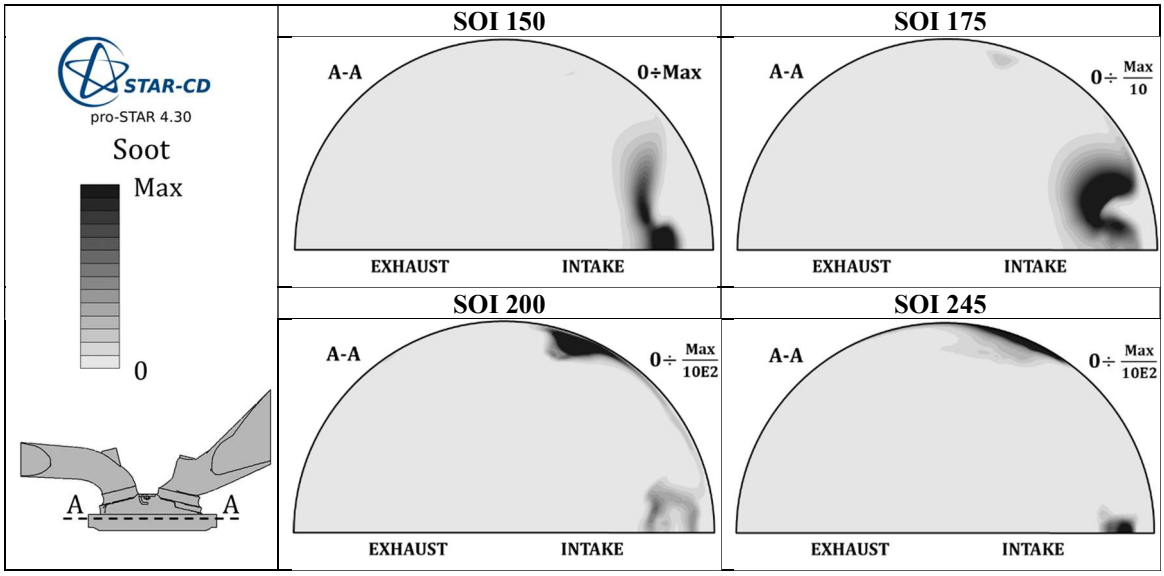

Fig.70: Soot mass fraction, 30 °CA aTDCF, for the different SOI. Scale on the left is valid only for SOI 150. Anticipating the SOI, maximum reduces, as indicated in the figures. Sections are normal to the cylinder axis and 3 mm below the cylinder head.

Before any quantitative comparison with experiments is made, it is necessary to account for all the processes that particles undergo in the PNC as described in the previous paragraph. In particular dilution, which is nearly 5000:1. Moreover, experimental outcomes refer to standard conditions (273.2 K and 101.33 kPa), which are sensibly different from in-cylinder ones at EVO. To account for both DR and standard pressure and temperature, Eq. 12 is adopted. The equivalent volume $V_{eq,EVO}$ can be used along with the resulting number of Soot particles at EVO PN_{EVO} [#] to obtain the Particle Number (PN) [#/cm^3] as in Eq. 13. PN_{EVO} is evaluated in Eq. 14, as the sum of the particle number of each single section $PN_{EVO,i}$.

$$V_{eq,EVO} = V_{CC,EVO}(1 + DR)\left(\frac{T_o}{T_{CC,EVO}}\right)\left(\frac{p_{CC,EVO}}{p_o}\right) \quad (12)$$

$$PN = \frac{PN_{EVO}}{V_{eq,EVO}} \quad (13)$$

$$PN_{EVO} = \sum_i PN_{EVO,i} = \sum_i \frac{m_{Soot,EVO,i}}{V_{mean,i}\,\rho_{Soot}} \qquad (14)$$

Finally, counting efficiency of the instrument is applied to numerical particles. In this regard, Fig.71 shows the actual counting efficiency curve of the PNC. As visible, a complete efficiency is achieved in between 40 and 50 nm while below 10 nm the photosensor is not able to detect particles.

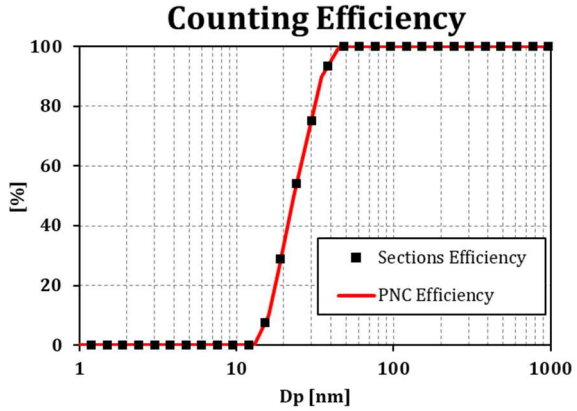

Fig.71: Experimental counting efficiency curve of PNC and relative extrapolated values for numerical Soot model sections.

A comparison between numerical and experimental outcomes in terms of PN is shown in Fig.72. On the numerical side, three different dataset are plot. The first one ("Total") reports PN obtained considering the total number of particles inside the cylinder at EVO and the original volume of the combustion chamber at the same CA, $V_{CC,EVO}$. This set of data remarkably differs from experimental values of more than 5 OoM. The second set ("Dilution"), compared to the previous one, is based on the equivalent volume $V_{eq,EVO}$, hence both standard conditions and, mostly, dilution are introduced. This remarkably improves results which approach the test bench outcome by OoM. Last data set adds the effect of counting efficiency. This leads to a further decrease of the numerical results which sensibly resemble the experimental values. In this case the error reduces and, for the worst case (the most sooting one, namely SOI 150) it is lower than 1 OoM. For more anticipated SOI, deviation from experimental data is even lower. Despite residual error is still not negligible for SOI 150, the fact that it is largely lower than 1 OoM represents a satisfying result, as confirmed by the existing literature [69, 76].

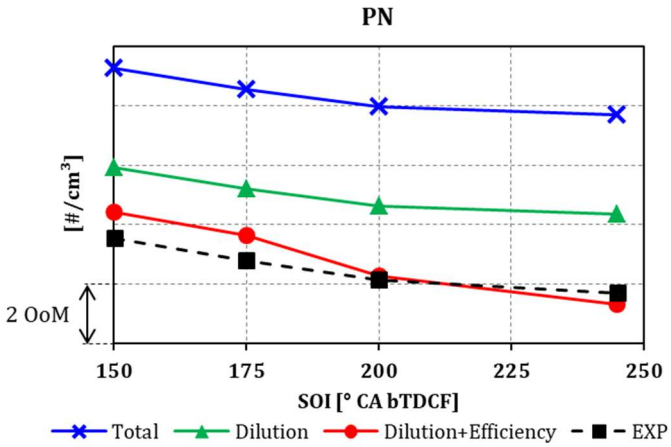

Fig.72: Numerical-experimental comparison in terms of Soot particle number (log scale).

Moving to gaseous emissions, Fig.73 reports values during the hot portion of the engine cycle, where formation is expected. Focusing on CO in Fig.73a), at the end of simulation mass is higher for the most delayed SOI. The reason is visible in Fig.74, which shows CO distributions for each condition at 30 °CA aTDCF. Similar to Soot, formation occurs in the rich mixture zones, where not enough oxygen is available to complete oxidation to CO_2. SOI 150 is the one exhibiting the richest zone on the intake side, thus it is the one with the highest production of CO. CO_2 is complementary to CO. For cases in which the latter is higher, the former is lower, as visible comparing Figs.73a) and 73b). In fact, Fig.75 CO_2 maps show that zones with lower concentration coincide with those exhibiting higher presence of CO in Fig.74. NO_x production is based on oxygen concentration and temperature. Therefore, it is not surprising that NO_x mass is larger for cases in which in-cylinder pressure is higher, as shown in Fig. 73c). Moreover, Fig.76 confirms that NO_x concentration is maximum where temperature is higher, that is in the core of the combustion chamber. As anticipated in the numerical setup paragraph, there is no dedicated model for unburnt hydrocarbons. Therefore, they are simply approximated by the remaining fuel at EVO. Fig. 73d) shows fuel amount in the chamber for the different SOIs: despite it reduces during combustion, a non-negligible quantity remains at the end of the simulation (~EVO) for all the cases. Even if combustion is still in completion, Fig.77 (reporting gasoline mass fraction at 30 °CA bTDCF) provides a reliable indication of the zones with the highest UHC concentration. As expected, they are located at the periphery of the combustion chamber, i.e. near the liner. Moreover, they are highly correlated, once again, to regions of rich mixture visible in Fig.66.

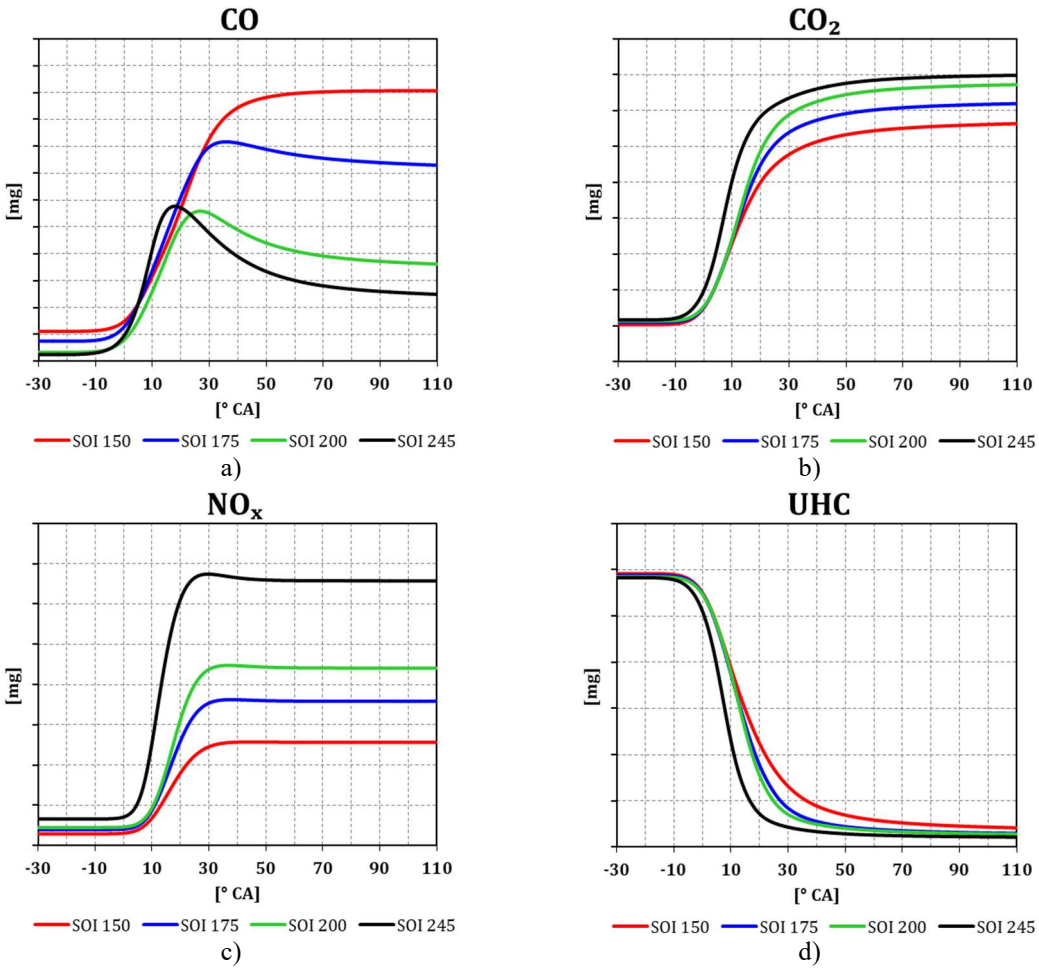

Fig.73: CO, CO_2, NO_x and UHC mass during the hot portion of the engine cycle.

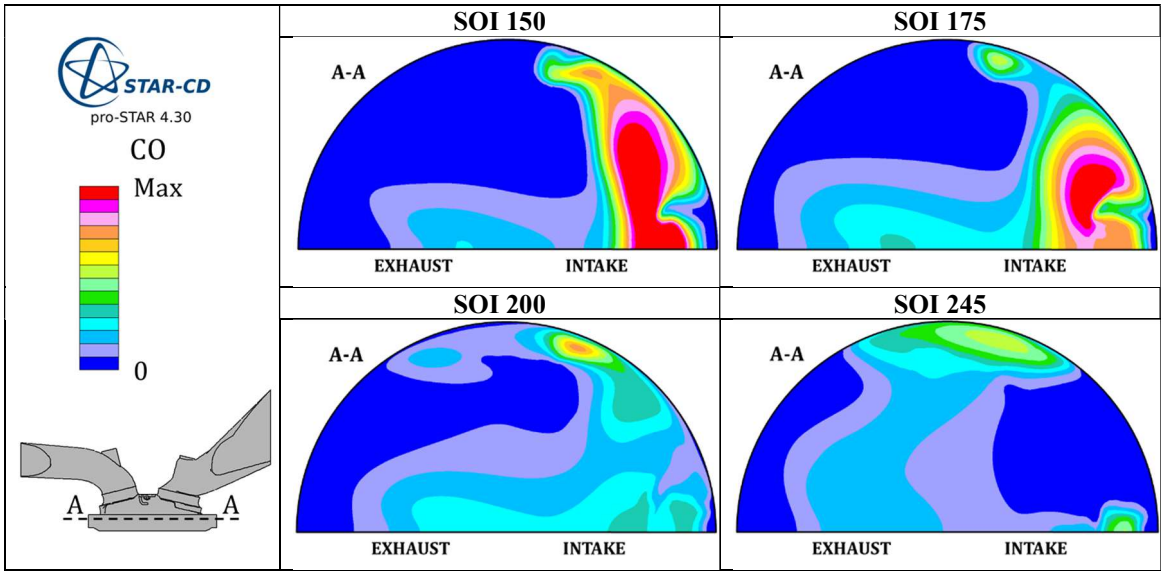

Fig.74: CO mass fraction, 30 °CA aTDCF, for the different SOI. Sections are normal to the cylinder axis and 3 mm below the cylinder head.

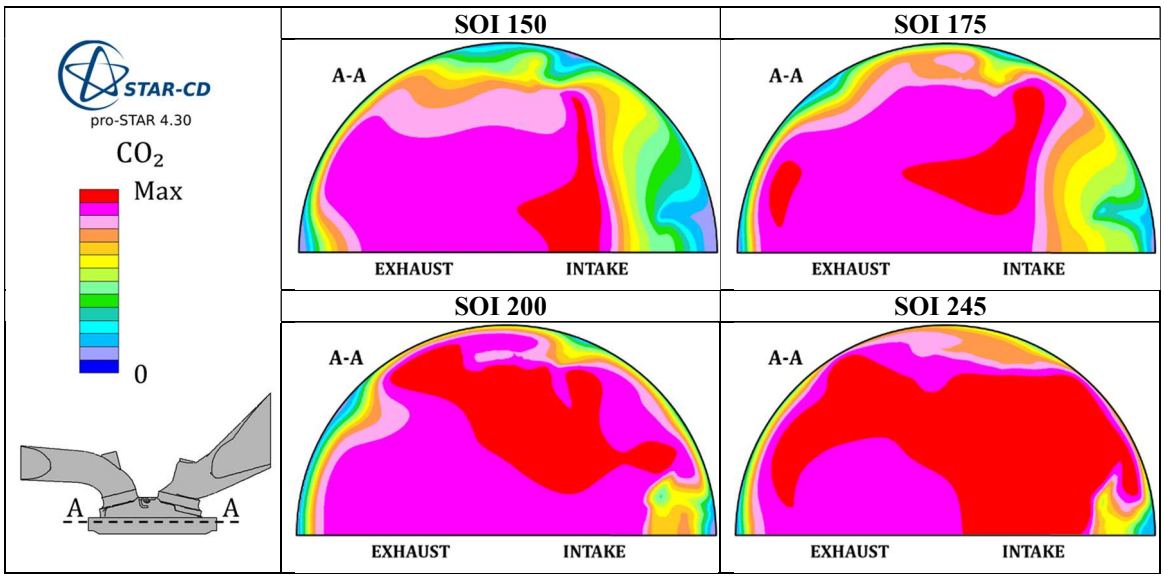

Fig.75: CO_2 mass fraction, 30 °CA aTDCF, for the different SOI. Sections are normal to the cylinder axis and 3 mm below the cylinder head.

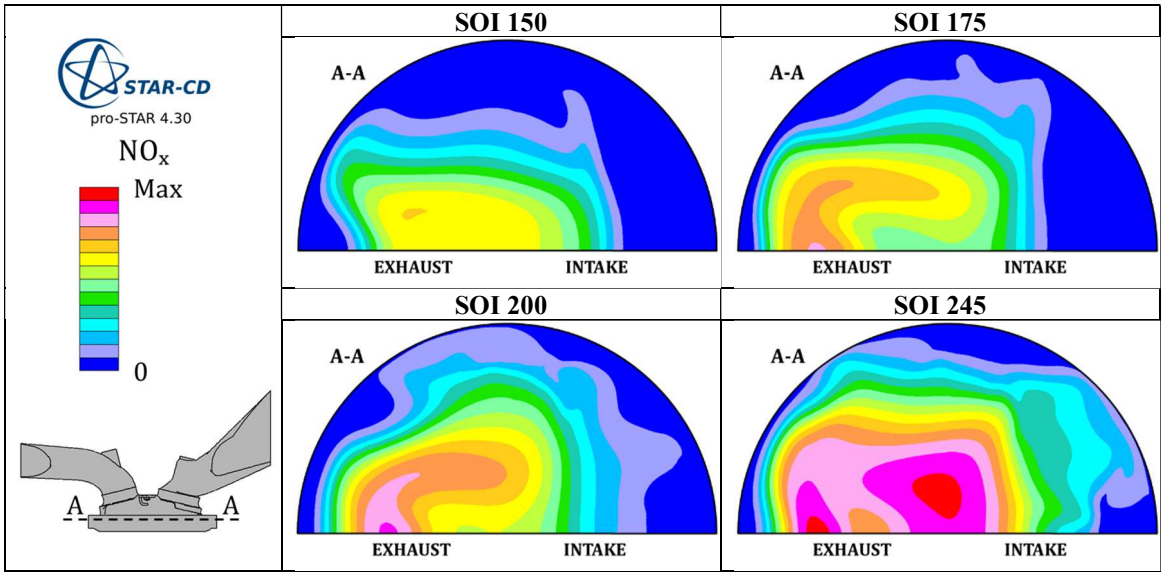

Fig.76: NO_x mass fraction, 30 °CA aTDCF, for the different SOI. Sections are normal to the cylinder axis and 3 mm below the cylinder head.

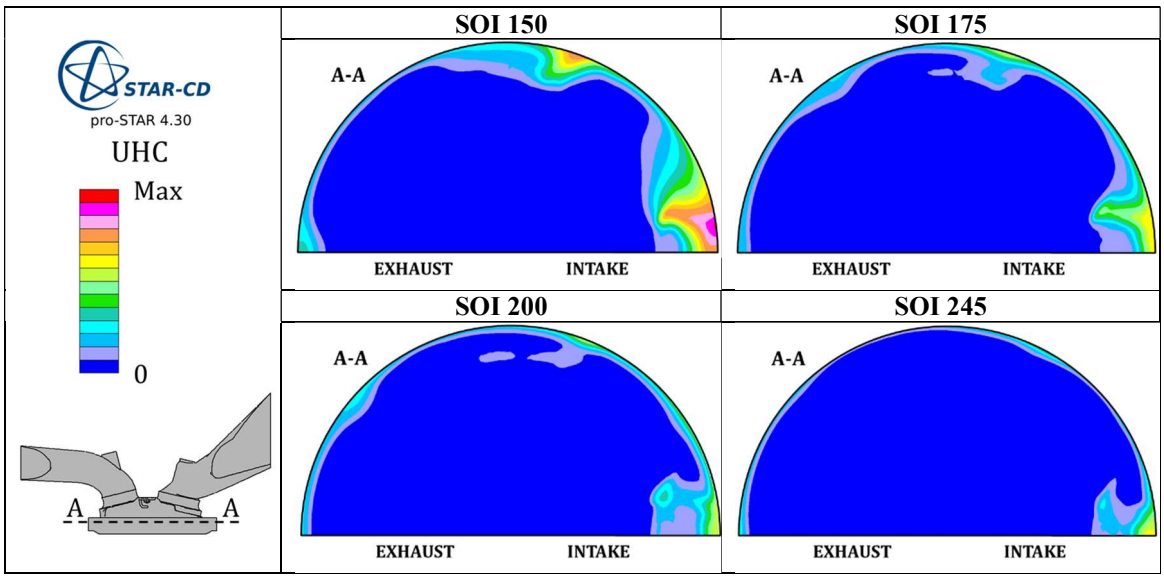

Fig.77: UHC mass fraction, 30 °CA aTDCF, for the different SOI. Sections are normal to the cylinder axis and 3 mm below the cylinder head.

With respect to Soot, numerical concentrations of gaseous emissions can be compared to the experimental counterparts in a more straightforward manner. Firstly, no dilution is performed. Secondly, concentrations expressed in %vol or ppm are not affected by thermodynamic conditions of the gas. In other words, there is no need to relate numerical results to the instrument output reference conditions. Finally, no counting efficiency has to be considered. At most, instrument tolerance should be accounted for, which is anyhow negligible. Both %vol and ppm, which is actually ppm(v), are concentrations by volume. Since the code returns mass fractions of transported scalars, a conversion is needed, following Eq. 15. To obtain density of each gas component (i-th gas) at EVO, Eq. 16 can be exploited, where the gas constant is evaluated as in Eq. 17 via the molecular weight M_w. Once volume of each component is known at EVO, then %vol or ppm can be obtained as in Eq. 18 and 19, respectively. The only critical issue is related to unburnt hydrocarbons, which are expressed as ppmC. Firstly, this prevents a one-to-one comparison between CFD and experiments. Secondly, Gasoline M_w (equal to 102) cannot be used to convert numerical mass fraction to ppmC following Eqs. 15 to 19, despite it is a pathway coherent with other emissions. In fact, this would require a conversion of the experimental data as well. The most straightforward solution to compare simulations and test bench data requires the adoption, in Eq. 17, of a M_w coming from a molecule containing 3 Carbon atoms, such as Propane (C_3H_8). This is needed to be coherent with the instrument which is calibrated via a Propane mixture and whose output is proportional to the one obtained via the Propane mixture itself. It is useful to remember that FID is insensitive to H atoms, thus output signal is just proportional to the one obtained during calibration and it is based on the Carbon atoms content of the exhaust gas. For this reason, any other molecule containing 3 Carbon atoms could be potentially adopted on the numerical side. Alternatively, molecules with different C content could be chosen but, as anticipated before, such choice would require a conversion of the experimental values.

$$V_{i-th\ gas,EVO} = \frac{m_{i-th\ gas,EVO}}{\rho_{i-th\ gas,EVO}} \quad (15)$$

$$\rho_{i-th\ gas,EVO} = \frac{p_{cc,EVO}}{T_{cc,EVO}\ R_{i-th\ gas}} \quad (16)$$

$$R_{i-th\ gas} = \frac{R}{M_{w,i-th\ gas}} \quad (17)$$

$$\%vol = \frac{V_{i-th\ gas,EVO}}{V_{CC,EVO}} 100 \quad (18)$$

$$ppm = \frac{V_{i-th\ gas,EVO}}{V_{CC,EVO}} 1e6 \quad (19)$$

In Fig.78 numerical and experimental values are finally compared for all the cases. In particular, Fig. 78a) focuses on CO, CO_2 and their sum. For the very delayed SOI, a slight overestimation of the CO content is noticed, which leads to a consequent minimal under-prediction of the CO_2. Comparing the summation of the two given by simulations with the experimental counterparts, an almost negligible error is noticed for each SOI. Fig. 78b) proposes the same comparison for NO_x. Trend is properly captured by CFD outcomes. Only for SOI 150 NO_x volume concentration is under-predicted. This is coherent with combustion results showing a slight underestimation of the in-cylinder pressure, which in turn leads to lower temperature peaks and, thus, to a lower production of Nitrogen oxides. Figure 78c) is dedicated to UHC. Different datasets are proposed. Blue curves represent the starting case, in which the experimental curve represents the instrument output while the numerical one relies on Propane M_w. A very satisfying agreement is obtained for SOI 175 and 200. For the extreme cases the error is not negligible and once again it is traceable to combustion. For the most delayed SOI, the resulting rich mixture on the intake side leads to an excessive amount of residual gasoline at EVO. Conversely, the most anticipated SOI is characterized by a slight over-prediction of the IMEP and thus of the heat release rate. This leads to a lower value of UHC compared to the experimental target. It is important to point out that residual gasoline (i.e. UHC value) is minimal for all the cases, thus a small variation can cause a non-negligible percentage error. Two additional datasets are compared in the figure. Black curves are obtained referring to the gasoline involved in the combustion, whose molecule has an equivalent Carbon content of 7.4 atoms (as well as 13.2 H atoms). In this case M_w equal to 102 is adopted in Eq. 17. Experimental data must be reduced via a multiplying factor of 3/7.4. In fact, the output signal relies on the calibration carried out via Propane and it has to be referred to gasoline. Fig. 78c) shows that results do not change remarkably and they are simply shifted compared to the previous ones. Only error percentage slightly differs. A final comparison is carried out considering a molecule characterized by a lower M_w compared to the reference case. To this aim, Methane (CH_4) is used, thus ppmC values increase for both simulations and experiments. As for the former, M_w of CH4 has to be used in Eq. 17. Values must be multiplied by a factor equal to 3. Once again, percentage errors are marginally affected and red curves are simply a shift of the previous ones. Therefore, it can be concluded that, regardless the adopted M_w (that is

regardless the selected molecule), almost the same relative error between CFD and experiments is obtained. In other words, the selected molecule is not decisive, provided that the same Carbon content is considered both for simulations and experiments.

Concluding, for all the gaseous emissions compared in Fig. 78, the overall agreement between CFD and experiments is satisfying. Major deviations are noticed for the most delayed SOI. This is coherent with the results previously discussed in terms of combustion indicators and Soot. Most likely, for SOI 150, CFD predicts regions with richer mixture than the expectations. On the one hand, this explains the underestimation of performance, CO_2 and NO_x with reference to the experimental evidence. On the other hand, it justifies the over-prediction of CO and UHC. The opposite happens for SOI 245. For this specific case, UHC value needs to be improved, while for the other analyzed emissions the agreement with experiments is already satisfying. In order to improve results, further investigations on the spray representation are needed, since it is (along with flow field) the main responsible of mixture stratification. The discrepancy in the in-cylinder pressure could one of the reasons but surely not the only one. For example, also a fuel multi-component approach can have significant mixture formation impact, thus combustion completeness, when we are at the extremes of the SOI variation where a relevant liquid formation occurs or the least volatile components play a relevant role in the most retarded ones. A geometrical feature like crevices (not taken into account in this study) might be object of future investigations. Despite calibration of the Lagrangian spray, especially of the secondary break-up model constants, is carried out at engine-like conditions, vessel pressure is higher (because of the availability of PDA data) than the actual one in the combustion chamber during injection. This can be a source of error. Moreover, approximations introduced to simplify the approach, may require partial reconsideration. Among them, the adoption of a unique set of boundary conditions from the 1D engine model and the use of exactly the same fuel amount for all the investigated conditions should be further checked.

That said, despite discrepancies (sometime even not negligible), the proposed methodology for post-processing and data management proves to be effective to obtain a fair comparison between CFD and test bench outcomes.

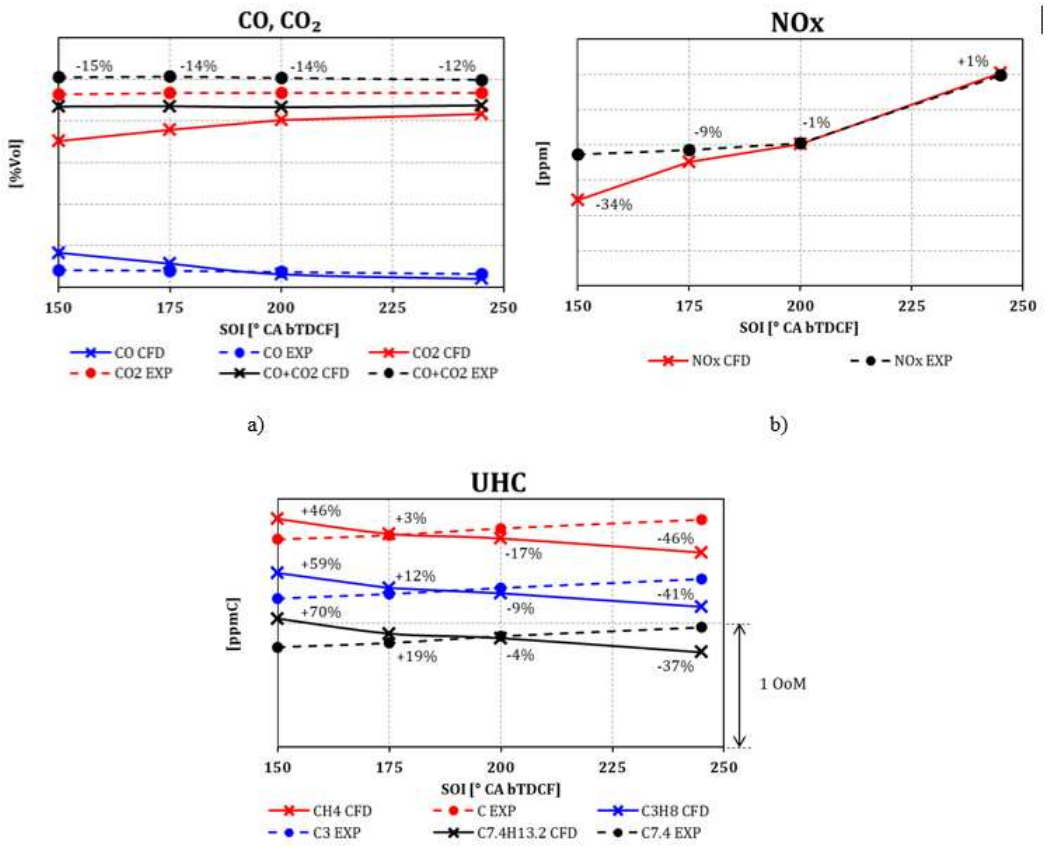

Fig.78: Numerical-experimental comparisons in terms of concentrations of CO, CO_2, $CO+CO_2$ (a), NO_x (b) and UHC (c). Percentage errors in a) refer to the deviation between numerical and experimental $CO+CO_2$; unlike a) and b), c) has a log-scale. Still in c), unit of measurement indicated in the y-axis is purposely generic as each set of curves has a its own; specifically, red curve values are expressed in $ppmC_1$, ones in blue curves in $ppmC_3$ and values of black curves are in $ppmC_{7.4}$.

3.5 CONCLUSIONS

In the present work, a robust numerical framework for the 3D-CFD simulation of Soot and gaseous emissions in spark-ignition engines is presented. It relies on well consolidated combustion and Soot models, namely ECFM-3Z and Sectional Method. In order to validate the numerical approach, a methodology to correlate CFD outcomes and experimental findings is proposed. In fact, a fair quantitative comparison requires an ad-hoc post-processing of the numerical results. Simulations and experiments are carried out on a high performance GDI turbocharged engine operated at part-load and low revving speed. As for the Soot particle number (PN), the thorough post-processing allows to obtain numerical results comparable to test bench data while, using the original output, the difference between CFD and experimental data would be greater than 5 OoM. As for gaseous emissions, in most of the cases the percentage error is acceptable. The main deviations regard NO_x and UHC estimations for the very delayed SOI, coherently with combustion indicators which reveal an underestimation of the combustion efficiency for the same case. This is mainly due to the resulting charge stratification at spark-time. In order to improve the simulation of the mixing process thus reducing the estimation error of the pollutant

emissions, on the one hand a more refined calibration of the spray model is needed. In particular, vessel conditions have to be as closed as possible the actual ones in the combustion chamber during injection. On the other hand, approximations such as the adoption of a unique set of boundary conditions and the use of the same fuel amount for all the investigated conditions have to be reduced at minimum. So overall, the proposed numerical setup and the developed post-processing are able to provide a quantitative estimation of both gaseous and solid emissions close to the experiments, as long as all the involved aspects such as chemical kinetic and mixture formation are accurately modeled.

3.6 ABBREVIATIONS AND SYMBOLS

0D/1D/3D	Zero-/ One-/ Three-Dimensional	$\tilde{k}_{OH}$	Reaction Rate for Oxidation involving OH radical
AHRR	Apparent Heat Release Rate	$\tilde{k}_{rev}$	Backward Reaction Rate for Surface Growth
aTDCF	After Top Dead Center of Firing	O	Oxygen
BDC	Bottom Dead Center	O_2	Molecular Oxygen
BMEP	Brake Mean Effective Pressure	O/C	Oxygen/Carbon Atom Ratio
bTDCF	Before Top Dead Center of Firing	OH	Hydroxyl group
CA	Crank Angle	m	Number of Hydrogen atoms in the fuel molecule
CFD	Computational Fluid Dynamics	$m_{i-th\ gas,EVO}$	Mass of the i-th gas at EVO
CFL	Courant-Friedrichs-Lewy	$m_{Soot,EVO,i}$	Soot mass of i-th section at EVO
CLD	Chemiluminescence Detetcor	$M_{w,i-th\ gas}$	i-th gas molecular weight
DC	Direct Current	n	Number of Carbon atoms in the fuel molecule
DISI	Direct-Injection Spark-Ignition	N	Nitrogen
DR	Dilution Ratio	N_2	Molecular Nitrogen
ECFM-3Z	Extended Coherent Flame Model – 3 Zones	NO	Nitrogen Monoxide
EGR	Exhaust Gas Recirculation	NO_x	Nitrogen Oxides
EoS	End of Simulation	p	Combustion chamber (instantaneous) pressure
ET	Evaporation Tube	p_0	Pressure at standard conditions
ETRF	ethanol/toluene/n-heptane/iso-octane based surrogate	$p_{CC,EVO}$	Combustion chamber mean p at EVO
EVO	Exhaust Valve Opening	PN	Particle Number
FID	Flame Ionization Detector	PN_{EVO}	Particle Number at EVO
GDI	Gasoline Direct Injection	$PN_{EVO,i}$	Particle Number of section i-th at EVO
GPF	Gasoline Particulate Filter	ppmC	Parts per million Carbon
IMEP	Indicated Mean Effective Pressure	ppm(v)	Parts per million (by volume)
MARS	Monotone Advection and Reconstruction Scheme	Q	Heat released
MON	Motor Octane Number	R	Universal gas constant
OoM	Order of Magnitude	$R_{i-th\ gas}$	i-th gas constant

PAHs	Polycyclic Aromatic Hydrocarbons	$\widetilde{RPAH}$	Rate of Formation of PAHs
PDF	Probability Density Function	S	Stroke
PISO	Pressure-Implicit with Splitting of Operators	T	Combustion chamber (instantaneous) temperature
PMP	Particle Measurement Program	T_0	Temperature at standard conditions
PNC	Particle Number Counter	$T_{CC,EVO}$	Combustion chamber mean T at EVO
PND	Particle Number Diluter	UHC	Unburned Hydrocarbons
RANS	Reynolds Average Navier-Stokes	$\tilde{u}$	Gas-phase Velocity
RNG	Re-Normalization Group	V	Combustion chamber (instantaneous) volume
RON	Research Octane Number	$V_{CC,EVO}$	Combustion Chamber Volume at EVO
SA	Spark-Advance	$V_{eq,EVO}$	Equivalent Volume at EVO
SOI	Start Of Injection	$V_{i-th\ gas,EVO}$	Volume of the i-th gas at EVO
TDC	Top Dead Center	$V_{mean,i}$	Mean particle volume at section i-th
TRF	toluene/n-heptane/iso-octane based surrogate	$\widetilde{Y}_{soot,i}$	Soot Mass Fraction for Section i
TSI	Threshold Soot Index	Σ	Flame surface density
VPR	Volatile Particle Remover	Φ	Equivalence Ratio
B	Bore	Φ_2	Equivalence Ratio threshold
C_nH_m	Generic fuel molecule	$\widetilde{\Omega}_{COAG,i}$	Coagulation Source Term for Section i
CO	Carbon Monoxide	$\widetilde{\Omega}_{COND,i}$	Condensation Source Term for Section i
CO_2	Carbon Dioxide	$\widetilde{\Omega}_{OX\,i}$	Oxidation Source Term for Section i
$D_{soot,t}$	Soot Turbulent Diffusion Coefficient	$\widetilde{\Omega}_{PI,i}$	Particle Inception Source Term for Section i
F	Fuel oxidation reaction coefficient	$\widetilde{\Omega}_{SG,i}$	Surface Growth Source Term for Section i
H	Hydrogen	$\widetilde{\Omega}_{soot,i}$	Soot Source Term for Section i
H_2	Molecular Hydrogen	γ	Specific heat ratio
H_2O	Water molecule	θ	Crank angle relative to TDC
H/C	Hydrogen/Carbon Atom Ratio	$\bar{\rho}$	Gas-phase Density
i	Section Index	$\rho_{i-th\ gas,EVO}$	Density of the i-th gas at EVO
$\tilde{k}_d$	Forward Reaction Rate for Surface Growth	ρ_{Soot}	Mean Soot density
$\tilde{k}_{O_2}$	Reaction Rate for Oxidation involving molecular oxygen	%vol	Percent by volume

Chapter 4

A new methodology development to assess oil tank sloshing of a High-Performance Car under racetrack maneuvers

4.1 Introduction

In modern engine architecture, the auxiliary system of oil tank addresses many tasks, from the obvious lubricant purposes to also emission related missions. From the performance/lubricant target point of view, the engine oil tank needs to be able to separate the oil blow-by coming from the recovery pumps. During all the working conditions of the vehicle mission, the lower part of the engine oil tank has to cover the feeding pump section in order to prevent oil pressure drops in the lubricant circuit. Lubricant oil pressure needs to be maintained at the designed level in order to guarantee the correct amount of oil at all the engine utilities and thus prevent engine failures. From the emission point of view, the engine blow-by has to be recirculated into the engine intake line. The major engine oil tank mission is to separate as much as possible the engine oil from the blow-by air, thus reducing as much as possible oil entrance in the engine intake line. Once the oil enters in the intake line, it is well known its connection to HC emission release, due to the oil burning in the combustion chamber. This condition is detrimental for modern engine, especially looking at the stricter emission regulations they are going to face in the near future time.

Considering that during the normal vehicle development plan, the engine, the oil tank and the vehicle itself will meet quite close to the production phase, it is quite important to develop a virtual tool to minimize:

- Oil tank dimension to improve vehicle performance.
- Optimize the oil tank shape to reach performance and emission targets in order to reduce/avoid the number of experimental loops to solve possible system anomalies.
- Time to market of the component itself.

In this context, CFD tools have been evaluated and a novel promising approach is later described. As stated above, in the oil tank functioning, air, oil and their mixture have to be described at the same time as well as for their interactions, consequently a multiphase approach is mandatory in numerical CFD investigations.

A multiphase flow is based on the interaction of more than one matter or phase of matter that exist simultaneously. Multiphase flows are commonly adopted and spread in many industries, starting from power up to aerospace, transport, and power. Their application ranges from engine injection, distillation, bubble columns and coolant systems. As a consequence, it is crucial to understand what the term “multiphase flow” stands for.

Many applications of CFD in the process and associated industries are found in literature [1,2]. While the development of CFD methodologies for dispersed multiphase flows has been long focused on relatively low volume fractions of the dispersed phase, many important industrial processes are carried out at high volume fractions. Phase separation is

often used to isolate products from unwanted by-products, e.g. lubricating oil tanks. At free-surfaces, rapid changes in the flow properties occur, which tend to cause singularities in numerical methods and are often troublesome. Among the industrial problems where multiphase flows are found, liquid sloshing in storage tanks has been largely studied over the past decades for the analysis of a multitude of applications ranging from industrial processes to aeronautics, from naval to automotive [3] Liu Z. et al. [4] found out that sloshing excitations have great influence also on the thermal physical process in cryogenic storage tanks, promoting the mixing of vapor and liquid and enhancing heat exchange. With reference to the automotive field, Fontanesi et al. [7] investigated the use of automated mesh adaptation to limit the numerical diffusion issues in CFD simulations of a lubricant tank for high performance engine applications.

Going into detail within the automotive field, the design of fuel and oil tanks must deal with several challenging issues. Firstly, the correct estimate of the instantaneous position and shape of the free surface in both fuel and oil tanks is of primary importance to prevent partial or total uncovering of the suction section of feed pumps leading to sudden pressure drops in the fuel / oil circuits. Secondly, in modern lubricant oil tanks it is increasingly important to properly account for oil vapor formation due to high thermal loads occurring into high performance engines. Oil vapor should not be released into the atmosphere, and it must be properly managed according to current legislation. Thirdly, the mixture entering the tank is usually a finely dispersed air/oil mist or even a foam-like mixture. Therefore, it is essential, in the design process of the tank, to seek solutions promoting phase separation upstream of the feeding pump, thus avoiding pressure drops due to low-density mist/foam in the oil pump delivery pressure.

As previously stated, sloshing dynamics is often a very difficult topic to study. The experimental investigation of sloshing problems is extremely complex since it usually relies both on the visualization of the motion of the free surface by means of transparent models and on local pressure signals measured by transducers placed in different locations of the tank. Furthermore, experiments are useful as long as they are carried out imposing accelerations and motions of the tank as close as possible to real ones. Because of this, CFD is massively used for the analysis of sloshing problems, since it allows a deeper understanding of the thermo-physical phenomena affecting sloshing dynamics with lower response times and costs than experimental practice.

4.2 Methodology

4.2.1 Vof Approach

Most CFD applications with regard to oil tank sloshing are based on the assumption that liquids and air are immiscible. Such applications are traditionally investigated using the Volume Of Fluid (VoF) approach [8], which assumes that the two phases are immiscible, resolving the interface between them. In this perspective, in order to limit as much as possible numerical diffusion and to maintain a sharp interface, it is crucial the adoption of appropriately low time steps as well as very fine computational grids around the free surface.

Since the presented application covers long physical time, spanning multiple track laps, computational cost grows dramatically despite the adoption of devoted strategies such as adaptive time-step and local grid refinements. In addition, a fully mixed mixture enters in the tank, where a conventional VoF approach could be unsuitable in this specific investigation. Under these circumstances, the adoption of a model able to handle the separation between the phases, as well as possible foam formation is of paramount importance.

4.2.2 EMP approach

In the Eulerian MultiPhase approach, the governing equations are solved everywhere in the domain, i.e. each phase is treated as inter-penetrating continua. Therefore, this approach is well-suited to a wide range of multiphase flows and is commonly used for modeling dispersed flows. A volume fraction of each phase is defined, coherently with VoF approach.

The model is able to simulate phase separation and foam formation according to local inertial forces since the conservation equations for each phase variable require closure by the definition of phase interactions at each phase interface. As a consequence, this approach does not necessarily require the adoption of very low time steps or very fine computational grids.

On top of that, VoF approach may provide misleading results since the assumption of immiscible fluids could become critical under rapidly changing and severe inertial accelerations. Finally, considering the high computational costs of transient VoF simulations inevitably leads to waste of both time and resources during the design phase of the tank.

4.2.3 Modus Operandi

In order to evaluate the EMP robustness and responsiveness, in handling the phases interaction, different applications are carried out, characterized by an increasing level of complexity.

Firstly, a simplified test case, studied in detail by Akyildiz et al. [9] is replicated; Secondly, a static application of a real oil tank for high-performance sports cars is performed. In this case, the aim is to reproduce the experimental pressure signal of the oil circuit. In fact, due to partial/total uncovering of the pump feeding section or to air entrainment during the oil motion, the oil pressure shows some valleys affecting the lubricant capability of the whole system. As a last case, this current production oil tank for high-performance sports car is analyzed under actual driving inertial accelerations, that is a dynamic simulation of two consecutive track-laps. In this case the numerical air percentage which reaches the feed pump suction side is compared to the experimental oil pump delivery signal along the track-lap.

In the studies of Akyildiz et al. [9], the sloshing effects on a rectangular tank, partially filled with water, was analyzed under pitch oscillations. Several tests were performed varying the liquid fill depth, the roll amplitude, the rotation frequency and the disposition of the internal baffles. In each case, a sensitivity of sloshing loads and wave observation were carried out. They highlighted that both vertical and horizontal baffles were able to significantly reduce fluid motion. The tank was purposely designed with interchangeable internal baffle arrangements. Nine pressure transducers were mounted to monitor pressure distribution at different locations. The tank dimensions, the arrangement of the internal baffles and pressure transducers are shown in Fig.79. The tank can rotate about a transverse axis passing through the tank geometrical center. Despite this application could be effectively simulated using a traditional VoF framework, the application of EMP modelling is preferred in order to test the capability of the approach to properly reproduce the entrapment and releasing of air into water as well as the formation of water droplets with a cheaper computational cost than that of VoF. With the specific purpose to evaluate the effectiveness of the model in challenging scenarios, the case with the most complicated dynamics is considered, i.e., with the maximum roll amplitude (8 deg), the maximum liquid fill depth (75%) and with a rotation frequency of 3 rad/s; both horizontal and vertical baffles are considered.

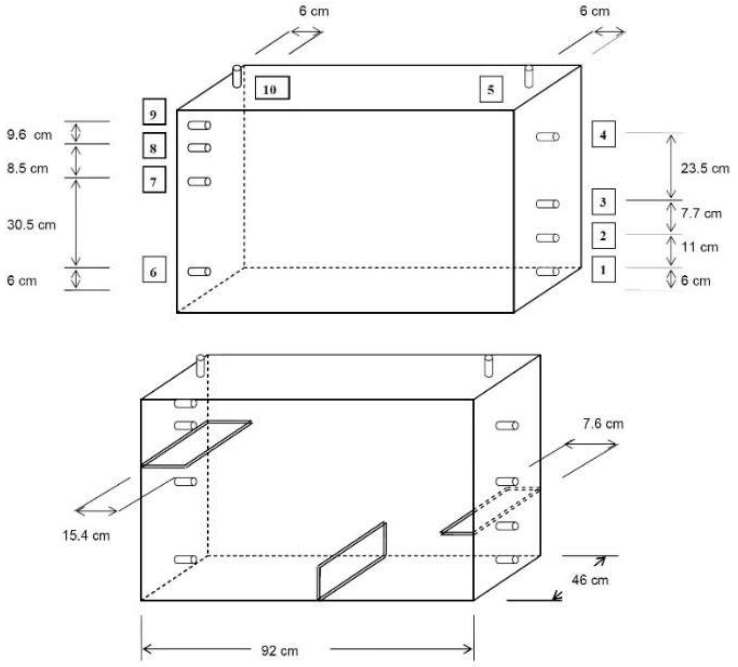

Fig.79: Experimental setup

The CFD setup for all cases is based on a k-ε two-Layer turbulence model. An All-Y+ approach is used because of the wide range of y+ experienced during the simulation. As opposed to VoF-based simulations, the EMP ones can handle phase interaction regardless of the adopted grid, because phase interaction models act at a sub-grid level. At the same time, it is still recommended to use a sufficiently fine grid to capture the sloshing dynamics and fit even the thinnest passages, typical of lubricant tanks of high-performance cars. Hence a trade-off between conflicting requirements has to be found. A polyhedral grid is considered a good solution to well reproduce the complex geometry of the oil tanks which will be described in the next sections. To confirm grid-independence of the EMP model, a mesh sensitivity is preliminarily carried out and both hexahedral and polyhedral grids are compared. Thanks to the symmetry of the real geometry, only half of the domain is modelled to reduce the computational effort, this resulting in a computational grid made up of approximately 1 mil. cells, with a uniform cell size of 5 mm. As depicted in Fig.80, a comparable water distribution is found with the two grid approaches and, as shown in Fig.81, the EMP model grid-independency is further confirmed by the numerical pressure signals measured at Probe2 and Probe7.

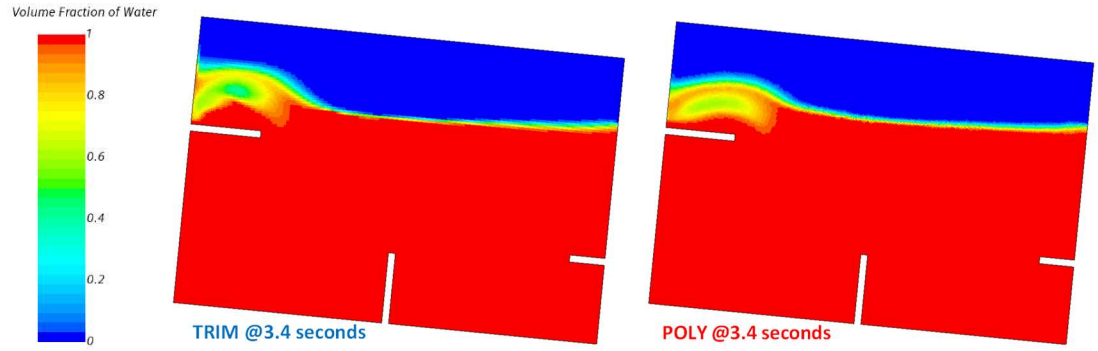

Fig.80: Air/oil mixture after 3.4 seconds with trim and polyhedral grid.

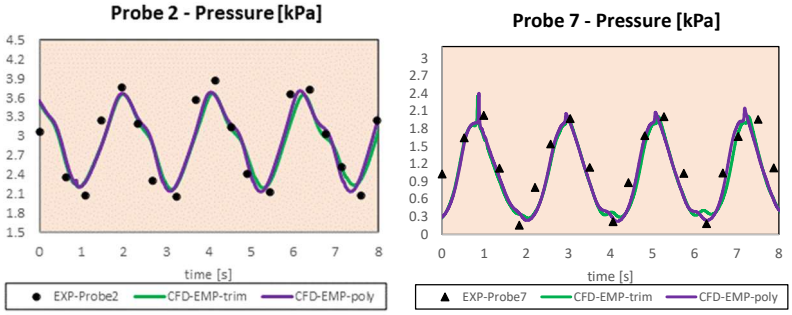

Fig.81: Experimental and numerical pressure traces.

Finally, the EMP model and its VoF counterpart are compared on equal grid spacing and time-step. As depicted in Fig.82, phases quickly start to mix. Despite VoF assumes immiscible fluids and the two phases are completely separated at the beginning of the simulation; partially mixed air/water spots appear throughout the domain. Once formed, such spots cannot be recovered by the model. This is a confirmation of the well-known sensitivity of VoF to numerical diffusion unless very fine grids and time steps are adopted.

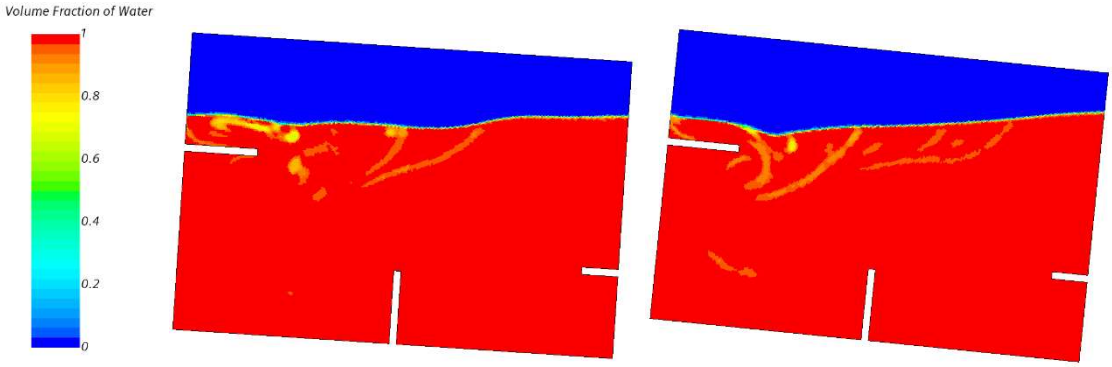

Fig.82: Air/oil mixture after 5.4 and 7.6 seconds, respectively on the left and on the right, with VoF model, polyhedral mesh.

The numerical pressure signals measured at Probe2 and Probe7 using both EMP and VoF simulations on equal grid are compared with the corresponding experimental pressure signals and they are reported in Fig.83. Once again, the EMP model shows a better agreement with experimental data besides its superior capability to predict shape and position of the free surface, local phase separation and mixing.

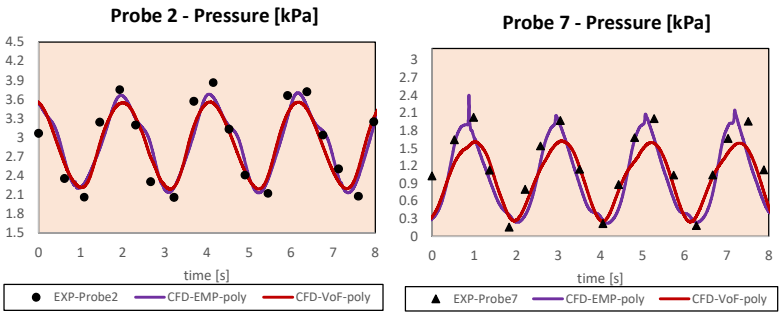

Fig.83: Experimental and numerical pressure traces

4.3 Static simulation of an oil tank for high-performance sports cars

Before assessing the performance of EMP in the simulation of the lubricant tank subject to multiple consecutive racetrack laps, a further preliminary sensitivity analysis is carried out on the oil tank subject to a static load, i.e., neither displacements nor accelerations are applied. In this application the tank is placed in a fixed position and no car accelerations are considered. Based on the promising results of the EMP model in terms of ability to simulate the separation and mixing of phases without the need of using either numerically expensive high-resolution grids or very low time steps, the methodology is furtherly tested in a real oil tank for high-performance sports cars. Particular attention is paid to the capability of the EMP approach to predict the formation of lubricant oil foam. Test rig data at peak power operation are available in terms of volume percentage of foam measured shortly downstream the suction side of a feeding pump. The experimental dataset consists of the variation of foam quantity as a function of the initial oil level inside the tank. It is essential to guarantee the continuous oil exchange from the inlet pipe up to the feeding pump.

A network of chambers and ducts is used to allow the incoming air/oil mixture, which is perfectly mixed with 61% air in volume, to separate so that the suction side of the feeding pump is supplied with a continuous flow of oil. The simultaneous presence of multiphase fluid-dynamics and the complex geometry of a real lubricant tank requires to use a model able to accurately handle the interaction between phases, while preserving rapidity and efficiency. Under static conditions and with a constant feeding flow rate, the tank is perfectly able to separate the incoming phases. Therefore, equal mass flow is found at the suction side of the feed valve and at the vent ducts in the upper part of the tank. The percentage of foam measured in the experiments can be therefore calculated from the equilibrium of the entering oil mass flow and the one exiting towards the pump.

In the present work two oil levels are simulated, for the sake of simplicity named as “high” and “low” in the following. An experimental foam percentage of 0.5% and 8% is measured for the high and low oil levels, respectively. The absolute uncertainty affecting the experimental data is ±6%. The measured foam percentage is expected to decrease for increasing oil quantity within the tank.

Constant density is again assumed for both phases and an All-y+ approach is used to accommodate the wide range of y+ experienced during the simulation.

For the sake of consistency with the experimental measurements, the computational domain covers the whole lubricant tank from the mixture inlet duct to the suction side of the feeding pump, resulting in a grid made up of nearly 800’000 cells with cell sizes ranging between 1 and 4 mm. Unlike the simplified test case described in the previous section, this oil tank is rich in fittings, edges, bulkheads and cavities. This further emphasizes the advantage of discretizing the domain with a polyhedral grid, to better preserve consistency with the original CAD geometry.

Fig.84 shows a section cutting the inlet duct within the tank and, specifically, a comparison of VoF and EMP models in managing the entering air/oil mixture under the

same numerical setup and grid. Focusing on the proposed methodology, i.e. the EMP approach, the centrifugal force to which the mixture is subjected along the 90 deg. curvature of the inlet duct tends to separate the phases, pushing the heavier oil towards the outer radius. As for the VoF model, phase separation is not found either along the 90-degree curvature or in the subsequent hat-like surface. On the contrary, a remarkable non-physical transport of the oil in the upper chambers of the tank is found. This phenomenon, which is attributable to numerical diffusion, highlights the limits of VoF model in representing phase separation and mixing. In this type of application, the limits of VoF cannot be solved by brute-force reduction of time-step size and grid size, as the problem lies in the fact that a fully homogeneous mixture enters the domain, and its separation and mixing must be handled by the model.

To further emphasize the combination of improved robustness and higher computational efficiency of the EMP model, the same application is approached using a numerical setup which better suits VoF requirements in terms of grid finesse and convective Courant number. In particular, automatic mesh adaptation is used for the best trade-off between computational time and reduction of numerical diffusion over the iso-surface. Also, a stratified mixture enters the domain to fulfill VoF constraint of immiscible fluids, despite in reality the incoming fluid is a fully homogeneous mixture of air and lubricating oil.

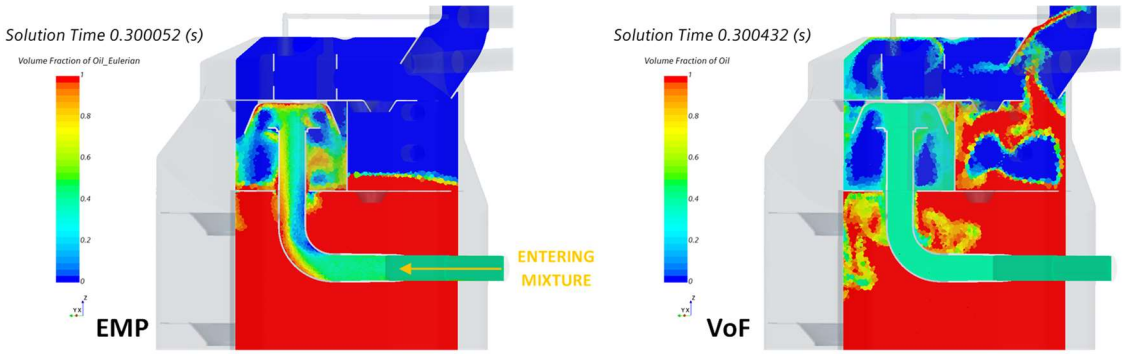

Fig.84: Air/oil mixture after 0.3 seconds. EMP on the left and VoF on the right.

As depicted in Fig.85, phase interaction is much better predicted and air bubble dragging is well appreciable all over the fluid domain. However, numerical diffusion is still visible in the domain and, most of all, the total computational time increases by nearly 20 times due to the combination of finer grid and resulting lower time-step needed to ensure low CFL numbers over the iso-surface.

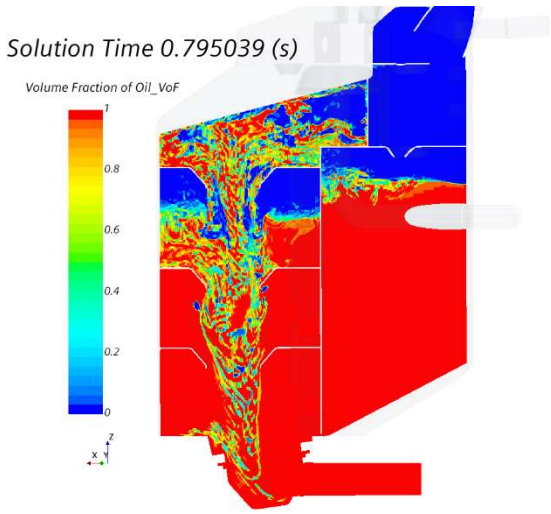

Fig.85: Air/oil mixture after 0.8 second, VoF model with adaptive mesh adaptation.

As depicted in Fig.86, a good agreement emerges between the measured foam percentage and the calculated one for both oil levels only when EMP model is adopted. Conversely, the same application approached with VoF using automatic mesh adaptation shows a much worse predictivity in terms of foam percentage at feed valve, in particular when a higher oil level is considered.

Focusing on EMP results, from a qualitatively standpoint the progressive increase of foam formation reducing the oil level inside the tank is well reproduced by CFD. Quantitatively speaking, the foam percentage found in the "high" case is higher than the experimental value, while decreasing the oil quantity a lower percentage of foam is found compared to the experimental one. Based on these results it can be deduced that the quantity of foam deriving from CFD simulations is less sensitive to the oil level within the tank than the experiments. However, numerical results perfectly fit within the error bandwidth affecting test-rig measurements. The EMP model can therefore be considered effective to simulate both phase separation and phase mixing.

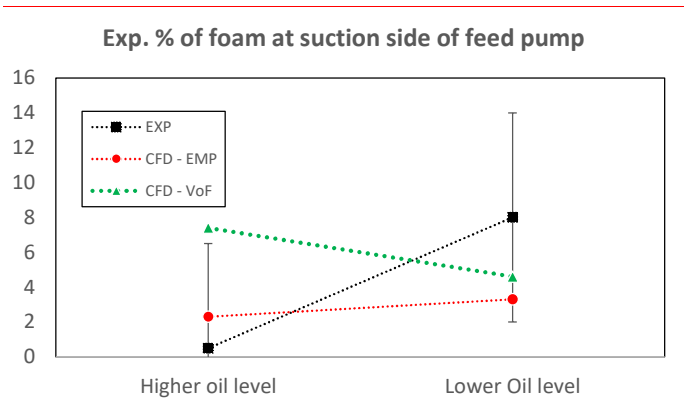

Fig.86: Numerical vs Experimental data.

4.4 Dynamic simulation of an oil tank for high-performance sport car

Given the promising results found not only in a simplified rectangular tank, but also in a real oil tank geometry designed for high-performance sports cars, the model is finally applied to simulate the lubricating oil tank under actual accelerations in typical racetrack maneuvers. As aforementioned, to simulate the sloshing dynamics affecting real lubricating tanks under actual racetrack accelerations, it is fundamental to use a 3D-CFD modelling framework able not only to properly handle interaction between the phases (mixing and separation), but also to do it in a responsive and computationally efficient manner.

As depicted in Fig.87, both longitudinal and lateral track lap accelerations onto the vehicle, and therefore onto the lubricant tank, vary quickly in both magnitude and sign. The first consequence of such steep variations on the CFD analyses is that it is difficult to identify and isolate specific maneuvers, since arbitrary imposition of prescribed initial conditions (mainly, location of the free surface and local mixture state) would tremendously impact the numerical outcomes. Therefore, it is recommended to run CFD analyses covering multiple (at least two) consecutive laps to let the model forget the imposed initial conditions. The second consequence is that the adopted modelling framework should be able to manage phase interactions during and after the most invasive maneuvers in a sound manner, since they are expected to lead to foam formation and/or separation of oil droplets, whose dynamics must be properly managed. In fact, the tank design phase is strongly influenced by these phenomena, which therefore deserve maximum care and attention by the CFD simulations. Consistently with the preceding static case, the computational domain covers the whole oil tank from the mixture inlet duct up to the lubricating pump inlet section. A polyhedral grid is once again adopted because of the complexity of the tank geometry. The computational grid is made up of approximately 600 thousand cells. Starting from an initial oil position at rest, i.e. with a horizontal free surface inside the tank, two consecutive track-laps are simulated to get rid of the influence of arbitrarily imposed initial conditions.

The air percentage entering the domain is now varying throughout the simulation ranging from a minimum of 68% to a maximum of 83%, according to the instantaneous air/oil mass flow measured at inlet duct.

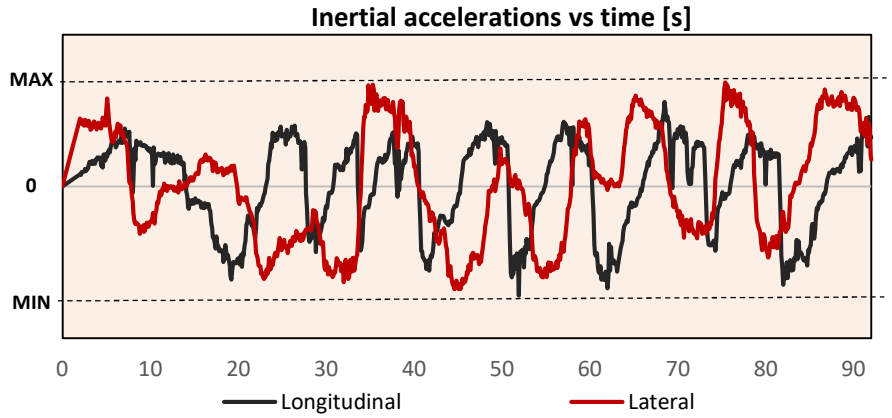

Fig.87: Inertial accelerations vs time

The oil pump delivery pressure signal is measured during the entire lap time. Fig. 88 shows the signal measured during the first 60 seconds of a track lap, which accounts for about two third of the total lap time. Any deviation or oscillation with respect to the reference value is associated with a non-continuous and non-uniform functioning of the feed pump; it can therefore be associated with the formation of foam inside the tank. As abovementioned, this undesired behavior could lead to mechanical failures even for very short interruptions of the lubrication. The investigated application, where physical and geometrical complexities are combined to very long physical times to be covered, emphasizes the need to define a proper modelling approach able to robustly simulate sloshing dynamics and phase interactions at reasonable computational costs and times.

Consistently with the static application described above, the air percentage is measured at the suction side of the feeding pump throughout the simulation, and it is shown in Fig.88. As it can be seen, a good agreement is found between the numerical air percentage and the experimental pressure signal measured shortly before the feeding pump. Whenever a perturbation in the experimental pressure signal is measured, air is detected in the corresponding CFD simulation. Moreover, the sudden drops in the oil pump delivery pressure are well phased with the peaks of air concentration seen by CFD at the pump inlet section. Finally, as it can be seen, non-negligible differences between the simulated laps can be observed. Even if peaks are phased in time in the two consecutive simulated laps, higher air percentages are computed along most of the second lap. This is due to the effect of initial conditions: while the first lap starts with an ideal (unrealistic) horizontal free surface inside the main chamber of the tank, the oil is well spread inside the tank at the beginning of the second lap and part of it falls inside the ducts and chambers in the upper part of the tank. Consequently, a lower level of oil is found inside the main chamber and, based on the results of the static application described in the previous chapter, a higher tendency towards foam formation is found.

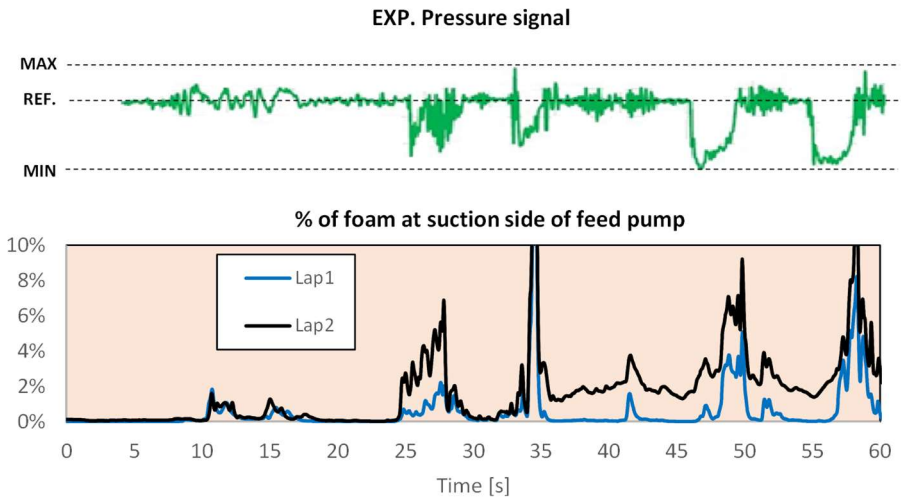

Fig.88: Comparison between exp. and num. pressure traces measured at suction side of feed pump

4.5 Conclusions

In this work a new methodology for sloshing applications based on the so-called Eulerian Multi Phase framework is described and investigated through 3D-CFD simulations. The effectiveness and responsiveness of EMP model in managing the phases interaction is assessed with three different applications, characterized by increasing complexity.

The methodology is firstly validated against experimental measurements in a simplified rectangular tank with internal baffles and under pitch oscillations, showing the capability of the model to handle phase separation and mixing.

Secondly, a static simulation of a current production lubricating oil tank for high-performance sports cars is carried out. Test-rig measurements of foam formation at the suction side of the feed pump are used to evaluate the capability of the model in representing phase interactions. Once again, EMP model shows good agreement with experimental data, reproducing the increase of foam reducing the oil quantity inside the tank.

Thirdly, a dynamic simulation of a current production lubricating oil tank for high-performance sports cars is analyzed under actual racetrack acceleration. The experimental oil pump delivery pressure signal along the track-lap is compared to the numerical air percentage which reaches the feed pump suction side. Once again, the model responsiveness in representing both sloshing dynamics and phase interactions throughout the simulation allows the simulation to fairly agree with the experimental evidence and data.

The analyzed applications increasingly demonstrate the superiority of the EMP model with reference to more established approaches such as VoF. EMP simulations are characterized by fewer constraints in terms of mesh density and Courant numbers, therefore they allow results to be obtained with much lower computational costs and times. Such observation is particularly relevant when facing computationally-expensive tasks such as the transient analysis of lubricating tanks under actual driving maneuvers. Furthermore,

conversely from VoF, EMP is able to correctly account for phase mixing and subsequent separation which play a relevant role in the evaluation of the performance of lubricant circuits and tanks.

Finally, the methodology shows high capability to effectively handle phase separation and mixing both qualitatively and quantitatively with massive computational-time savings, far exceeding the limits of the VoF approach and furtherly extending the fields of application of CFD analysis in multi-phase problems.

FINAL REMARKS

Today, designing a sports car represents a very complex challenge. On the one hand, it is necessary to take into account increasingly stringent homologation constraints in terms of emissions, sound, use of materials, etc. on the other hand, the advent of new technologies offers opportunities that were unthinkable until some time ago. Driven by these constraints, the technologies that have undergone a very important development process in the last period concern both the after-treatment part and the hybridization of the powertrain.

For a vehicle 'Architect' who during the setting phase has to design a car from a blank sheet that must meet all the requirements in terms of style, performance, emissions, consumption and costs, the big question is to understand how to exploit all the components concerned in order to obtain the best trade off.

It is clear that this is a design process that requires several evaluations and iterations because it is subject to many constraints and objectives but that, thanks to advanced simulation tools, today they can be deepened and addressed.

This context is what animated the development of the various virtual analysis methodologies present in this thesis on topics considered fundamental in order to be able to give useful help both in the concept phase and in the subsequent vehicle design phase.

As reported in the previous chapters, despite having dealt with very complex issues from both a physical and modeling point of view, the validation part of the methodologies gave good results for which the results set at the beginning of the research were achieved.

REFERENCES CHAPTER 1

[1] G. R. Guercioni, "Integration of Dual-Clutch Transmissions in Hybrid Electric Vehicle Powertrains", Politecnico di Torino, 2018.

[2] R. E. Bellman and S. E. Dreyfus, Applied Dynamic Programming. Princeton University Press, 2015.

[3] R. E. Bellman and R. E. Kalaba, Dynamic Programming and Modern Control Theory, 1st ed. Academic Press, 1966.

[4] R. E. Bellman, Dynamic Programming, 1st ed. Princeton, NJ: Princeton University Press, 1957.

[5] D. Bertsekas, Dynamic Programming and Optimal Control. Belmont, MA: Athena Scientific, 1995.

[6] S. Onori, L. Serrao, and G. Rizzoni, Hybrid Electric Vehicles: Energy Management Strategies, 1st ed. Springer-Verlag London, 2016.

[7] D. E. Kirk, Optimal Control Theory - An Introduction. Dover Publications, 1998.

[8] L. Tang, "Optimal energy management strategy for hybrid electric vehicles with consideration of battery life," Ohio State University, 2017.

[9] D. Sinoquet, G. Rousseau, and Y. Milhau, "Design optimization and optimal control for hybrid vehicles," Optim Eng, vol. 12, no. 1–2, pp. 199–213, 2011.

[10] E. Vinot, R. Trigui, Y. Cheng, C. Espanet, A. Bouscayrol, and V. Reinbold, "Improvement of an EVT-Based HEV Using Dynamic Programming," IEEE Trans. Veh. Technol., vol. 63, no. 1, pp. 40–50, 2014.

[11] T. Hofman, M. Steinbuch, R. van Druten, and A. Serrarens, "A Rule-based energy management strategies for hybrid vehicles," Int. J. Electr. Hybrid Veh., vol. 1, no. 1, pp. 71–94, 2007.

[12] R. Biasini, S. Onori, and G. Rizzoni, "A near-optimal rule-based energy management strategy for medium duty hybrid truck," Int. J. Powertrains, vol. 2, no. 2–3, pp. 232–261, 2013.

[13] L. Pérez, G. Bossio, D. Moitre, and G. García, "Optimization of power management in an hybrid electric vehicle using dynamic programming," Math. Comput. Simul., vol. 73, no. 1–4, pp. 244–254, 2006.

[14] L. Serrao, S. Onori, and G. Rizzoni, "A Comparative Analysis of Energy Management Strategies for Hybrid Electric Vehicles," ASME J. Dyn. Syst. Meas. Control, vol. 133, no. 3, p. 31012, 2011.

[15] V. D. Ngo, J. A. C. Navarrete, T. Hofman, M. Steinbuch, and A. Serrarens, "Optimal gear shift strategies for fuel economy and driveability," Proc. Inst. Mech. Eng. Part D J. Automob. Eng., vol. 227, no. 10, pp. 1398–1413, 2013.

[16] C.-C. Lin, H. Peng, J. W. Grizzle, and J.-M. Kang, "Power management strategy for a parallel hybrid electric truck," IEEE Trans. Control Syst. Technol., vol. 11, no. 6, pp. 839–849, 2003.

[17] G. Rousseau, D. Sinoquet, and P. Rouchon, "Constrained Optimization of Energy Management for a Mild-Hybrid Vehicle," Oil Gas Sci. Technol., vol. 62, no. 4, pp. 623–634, 2007.

[18] Bianchi D, Rolando L, Serrao L, Onori L, Rizzoni G, Al-Khayat N, Hsieh TM, Kang P. A rule-based strategy for a series/parallel Hybrid Electric Vehicle: an approach based on Dynamic Programming. 2010 ASME Dynamic Systems and Control Conference.

[19] Millo F, Rolando L, Andreata M. Numerical simulation for vehicle powertrain development. In: Numerical analysis – theory and application, AA.VV. 2011: pp. 519–540. ISBN 978-953-307-389-7.

[20] Guzzella G, Sciarretta A. Vehicle propulsion systems: introduction to modeling and optimization. Berlin: Springer; 2007, ISBN 9783642094156.

[21] Guercioni G.R., Vigliani A., Galvagno E., Midlam-Mohler S., Gearshift Control for Hybrid Powertrains with AMTs, 2017 International Conference of Electrical and Electronic Technologies for Automotive, Torino (Italy), June 15-16, 2017, pp. 1-9. ISBN:978-88-87237-26-9. DOI:10.23919/EETA.2017.7993202.

REFERENCES CHAPTER 2

[1] Sterlepper, S., Claßen, J., Pischinger, S., Görgen, M. et al., "Relevance of Exhaust Afertreatment System Degradation for EU7 Gasoline Engine Applications," SAE Technical Paper 2020-01-0382 (2020). https://doi.org/10.4271/2020-01-0382

[2] Joshi, A., "Review of Vehicle Engine Efciency and Emissions," SAE Int. J. Advances & Curr. Prac. in Mobility 2, no. 5 (2020): 2479-2507

[3] Weller, H., Tabor, G., Jasak, H., and Fureby, C., "A Tensorial Approach to CFD using Object Orientated Techniques,"Computers in Physics 12, no. 6 (1998): 620

[4] Della Torre, A., Montenegro, G., Onorati, A., and Cerri, T., "CFD Investigation of the Impact of Electrical Heating on the Light-off of a Diesel Oxidation Catalyst," SAE Technical Paper 2018-01-0961 (2018). https://doi.org/10.4271/2018-01-0961.

[5] Della Torre, A., Montenegro, G., Onorati, A., Cerri, T. et al., "Numerical Optimization of a SCR System Based on the Injection of Pure Gaseous Ammonia for the NOx Reduction in Light-Duty Diesel Engines," SAE Technical Paper 2020- 01-0356 (2020). https://doi.org/10.4271/2020-01-0356.

[6] Della Torre, A., Barillari, L., Montenegro, G., Onorati, A. et al., "Numerical Assessment of an After-Treatment System Equipped with a Burner to Speed-Up the Light-Off during Engine Cold Start," SAE Technical Paper 2021-24-0089, 2021, doi:10.4271/2021-24-0089

[7] Della Torre, A., Montenegro, G., Onorati, A., Paltrinieri, S.et al., "Calibration of the Oxygen Storage Reactions for the Modeling of an Automotive Tree-Way Catalyst," Industrial & Engineering Chemistry Research 20, no. 18 (2021): 6653-6661.

REFERENCES CHAPTER 3

[1] Fraser, N., et al., Challenges for Increased Efficiency through Gasoline Engine Downsizing. SAE International Journal of Engines, 2009. 2(1): p. 991-1008.

[2] Turner, J.W.G., R.J. Pearson, and S.A. Kenchington, Concepts for improved fuel economy from gasoline engines. International Journal of Engine Research, 2005. 6(2): p. 137-157.

[3] Schäpertöns, H., et al., VW's Gasoline Direct Injection (GDI) Research Engine. 1991, SAE International.

[4] Spicher, U., et al., Gasoline Direct Injection (GDI) Engines - Development Potentialities. 1999, SAE International.

[5] Costa, M., et al., Split Injection in a GDI Engine Under Knock Conditions: An Experimental and Numerical Investigation. 2015, SAE International.

[6] Gentili, R., E. Musu, and S. Zanforlin, Stratified Charge Strategies in Direct Injection S.I. Engines. 2005, Consiglio Nazionale delle Ricerche.

[7] Li, Y., et al., Experimental investigation the impacts of injection strategies coupled with gasoline/ethanol blend on combustion, performance and emissions characteristics of a GDI spark-ignition engine. Fuel, 2019. 256: p. 115910.

[8] Teodosio, L., V. De Bellis, and F. Bozza, Combined Effects of Valve Strategies, Compression Ratio, Water Injection, and Cooled EGR on the Fuel Consumption of a Small Turbocharged VVA Spark-Ignition Engine. SAE Int. J. Engines, 2018. 11(6): p. 643-656.

[9] Teodosio, L., et al., Impact of intake valve strategies on fuel consumption and knock tendency of a spark ignition engine. Applied Energy, 2018. 216: p. 91-104.

[10] Cracknell, R., et al., Assessing the Efficiency of a New Gasoline Compression Ignition (GCI) Concept. 2020, SAE International.

[11] Hua, J., et al., Influence of pre-chamber structure and injection parameters on engine performance and combustion characteristics in a turbulent jet ignition (TJI) engine. Fuel, 2021. 283: p. 119236.

[12] Paltrinieri, S., et al., Water Injection Contribution to Enabling Stoichiometric Air-to-Fuel Ratio Operation at Rated Power Conditions of a High-Performance DISI Single Cylinder Engine. 2019, SAE International.

[13] Franco Briguiet, G.d.O., et al., Investigation of powertrains in hybrid vehicles. 2021, SAE International.

[14] Seibel, J., S. Pischinger, and P. von Dincklage, Optimized Layout of Gasoline Engines for Hybrid Powertrains. 2008, The Automotive Research Association of India.

[15] Smirnov, O., et al., New Concept for Creating a Vehicle Hybrid Power Units. 2020, SAE International.

[16] Küsell, M., W. Moser, and M. Philipp, Motronic MED7 for Gasoline Direct Injection Engines: Engine Management System and Calibration Procedures. 1999, SAE International.

[17] Philipp, S., et al., Exhaust Gas Aftertreatment for Lean Gasoline Direct Injection Engines - Potential for Future Applications. 2013, SAE International.

[18] Pauly, T., et al., Cost and Fuel Economy Driven Aftertreatment Solutions -for Lean GDI. 2010, SAE International.

[19] Czerwinski, J., et al., PN-Emissions of Gasoline Cars MPI and Potentials of GPF. 2018, SAE International.

[20] Rubino, L., et al., Fundamental Study of GPF Performance on Soot and Ash Accumulation over Artemis Urban and Motorway Cycles - Comparison of Engine Bench Results with GPF Durability Study on Road. 2017, SAE International.

[23] Breda, S., et al., Experimental and numerical study on the adoption of split injection strategies to improve air-butanol mixture formation in a DISI optical engine. Fuel, 2019: p. 104-124.

[24] Mangeruga, V., et al., Design of a Hybrid Power Unit for Formula SAE Application: Packaging Optimization and Thermomechanical Design of the Electric Motor Case. SAE Int. J. Adv. & Curr. Prac. in Mobility, 2019. 2(2): p. 721-736.

[25] Teodosio, L., F. Bozza, and F. Berni, Effects of nanofluid contaminated coolant on the performance of a spark ignition engine. AIP Conference Proceedings, 2019. 2191(1): p. 020147.

[26] Xu, L., et al., Emission characteristics and engine performance of gasoline DICI engine in the transition from HCCI to PPC. Fuel, 2019. 254: p. 115619.

[27] Zheng, Z. and M. Yao, Charge stratification to control HCCI: Experiments and CFD modeling with n-heptane as fuel. Fuel, 2009. 88(2): p. 354-365.

[28] Bianco, A., F. Millo, and A. Piano, Modelling of combustion and knock onset risk in a high-performance turbulent jet ignition engine. Transportation Engineering, 2020. 2: p. 100037.

[29] Berni, F., et al. A numerical investigation on the potentials of water injection to increase knock resistance and reduce fuel consumption in highly downsized GDI engines. in Energy Procedia. 2015.

[30] D'Adamo, A., et al., A Numerical Investigation on the Potentials of Water Injection as a Fuel Efficiency Enhancer in Highly Downsized GDI Engines. SAE Technical Papers, 2015. 2015-April(April).

[31] Falfari, S., et al., Water Injection Applicability to Gasoline Engines: Thermodynamic Analysis. 2019, SAE International.

[32] Falfari, S., et al., PWI and DWI Systems in Modern GDI Engines: Optimization and Comparison Part I: Non-Reacting Flow Analysis. 2021, SAE International.

[33] d'Adamo, A., et al., The potential of statistical RANS to predict knock tendency: Comparison with LES and experiments on a spark-ignition engine. Applied Energy, 2019. 249: p. 126-142.

[34] Forte, C., et al., A RANS CFD 3D Methodology for the Evaluation of the Effects of Cycle By Cycle Variation on Knock Tendency of a High Performance Spark Ignition Engine. 2014, SAE International.

[35] Rosetti, A., et al., CFD analysis and knock prediction into crevices of piston to liner fireland of an high performance ICE. SAE Technical Papers, 2019. 2019.

[36] Cicalese, G., F. Berni, and S. Fontanesi, Integrated in-cylinder / CHT methodology for the simulation of the engine thermal field: An application to high performance turbocharged DISI engines. SAE International Journal of Engines, 2016. 9(1).

[37] Fontanesi, S., et al., Quantitative investigation on the impact of injection timing on soot formation in a GDI engine with a customized sectional method. International Journal of Engine Research. 0(0): p. 1468087421993955.

[38] Del Pecchia, M., et al., A threshold soot index-based fuel surrogate formulation methodology to mimic sooting tendency of real fuels in 3D-CFD simulations. Applied Energy, 2020. 280: p. 115909.

[39] AVL, AVL Partcile Counter Product Guide. 2010.

[40] UK, Regulation no. 83, Emissions of M1 and N1 categories of vehicles : proposal for draft supplement 7 to the 05 series of amendments to Regulation no. 83 / submitted by the expert from the United Kingdom, U. NATIONS, Editor. 2007.

[41] Horiba, MEXA 7170 User Guide.

[42] Garthe, C., et al., HC Measurements by Means of Flame Ionization: Background and Limits of Low Emission Measurement. 2003, SAE International.

[43] Ltd., C., HFR500 Fast Response FID Hydrocarbon Measurement System - User Manual (Version 2.9). 2011.

[44] SIEMENS, STAR-CD METHODOLOGY Version 4.30.

[45] Y. Han, Z. and R. Reitz, "Turbulence Modeling of Internal Combustion Engines Using RNG κ-ϵ Models". Vol. 106. 1995. 267-295.

[46] Berni, F., et al., On the existence of universal wall functions in in-cylinder simulations using a low-Reynolds RANS turbulence model. AIP Conference Proceedings, 2019. 2191(1): p. 020019.

[47] Berni, F. and S. Fontanesi, A 3D-CFD methodology to investigate boundary layers and assess the applicability of wall functions in actual industrial problems: A focus on in-cylinder simulations. Applied Thermal Engineering, 2020. 174.

[48] Berni, F., et al., Towards grid-independent 3D-CFD wall-function-based heat transfer models for complex industrial flows with focus on in-cylinder simulations. Applied Thermal Engineering, 2021. 190: p. 116838.

[49] Berni, F., G. Cicalese, and S. Fontanesi, A modified thermal wall function for the estimation of gas-to-wall heat fluxes in CFD in-cylinder simulations of high performance spark-ignition engines. Applied Thermal Engineering, 2017. 115: p. 1045-1062.

[50] Bozza, F., et al., Refinement of a 0D Turbulence Model to Predict Tumble and Turbulent Intensity in SI Engines. Part I: 3D Analyses. SAE Technical Papers, 2018. 2018-April.

[51] Bozza, F., et al., Refinement of a 0D Turbulence Model to Predict Tumble and Turbulent Intensity in SI Engines. Part II: Model Concept, Validation and Discussion. SAE Technical Papers, 2018. 2018-April.

[52] De Bellis, V., et al., Development of a phenomenological turbulence model through a hierarchical 1D/3D approach applied to a VVA turbocharged engine. SAE International Journal of Engines, 2016. 9(1): p. 506-519.

[53] Bracco, F.V., "Modeling of Engine Sprays". 1985, SAE International.

[54] Senda, J., et al., Modeling Spray Impingement Considering Fuel Film Formation on the Wall. 1997, SAE International.

[55] Habchi, C., A Comprehensive Model for Liquid Film Boiling in Internal Combustion Engines. Oil Gas Sci. Technol. – Rev. IFP, 2010. 65(2): p. 331-343.

[56] Colin, O. and A. Benkenida, The 3-Zones Extended Coherent Flame Model (Ecfm3z) for Computing Premixed/Diffusion Combustion. Oil & Gas Science and Technology - Rev. IFP, 2004. 59(6): p. 593-609.

[57] Berni, F., et al., Numerical Investigation on the Effects of Water/Methanol Injection as Knock Suppressor to Increase the Fuel Efficiency of a Highly Downsized GDI Engine. SAE Technical Papers, 2015. 2015-September(September).

[58] D'Adamo, A., et al., Understanding the origin of cycle-to-cycle variation using large-eddy simulation: Similarities and differences between a homogeneous low-revving speed research engine and a production DI turbocharged engine. SAE International Journal of Engines, 2018. 12(1): p. 1-22.

[59] Severi, E., et al. Numerical investigation on the effects of bore reduction in a high performance turbocharged GDI engine. 3D investigation of knock tendency. in Energy Procedia. 2015.

[60] D'Adamo, A., et al., Chemistry-Based Laminar Flame Speed Correlations for a Wide Range of Engine Conditions for Iso-Octane, n-Heptane, Toluene and Gasoline Surrogate Fuels. SAE Technical Papers, 2017. 2017-October.

[61] Del Pecchia, M., et al., Gasoline-ethanol blend formulation to mimic laminar flame speed and auto-ignition quality in automotive engines. Fuel, 2020. 264.

[62] Cavicchi, A., et al., Evaluation of hole-specific injection rate based on momentum flux measurement in GDI systems. Fuel, 2020. 263.

[63] Cavicchi, A., et al. Evaluation of the single jet flow rate for a multi-hole GDI nozzle. in AIP Conference Proceedings. 2019.

[66] Reitz, R.D. and R. Diwaker, "Effect of drop breakup on fuel sprays". 1986.

[67] Postrioti, L., et al., "Experimental and Numerical Analysis of Spray Evolution, Hydraulics and Atomization for a 60 MPa Injection Pressure GDI System". 2018, SAE International.

[68] Baulch, D.L., et al., Evaluated Kinetic Data for High-Temperature Reactions. Volume 5. Part 1. Homogeneous Gas Phase Reactions of the Hydroxyl Radical with Alkanes. Journal of Physical and Chemical Reference Data, 1986. 15(2): p. 465-592.

[69] Aubagnac-Karkar, D., et al., Sectional soot model coupled to tabulated chemistry for Diesel RANS simulations. Combustion and Flame, 2015. 162(8): p. 3081-3099.

[70] Marchal, C., et al. Soot modelling in automotive engines. in ECM, European Combustion Meeting, 4. 2009. ;.

[71] Netzell, K., H. Lehtiniemi, and F. Mauss, Calculating the soot particle size distribution function in turbulent diffusion flames using a sectional method. Proceedings of the Combustion Institute, 2007. 31(1): p. 667-674.

[72] Quiros, D.C., et al., Particle effective density and mass during steady-state operation of GDI, PFI, and diesel passenger cars. Journal of Aerosol Science, 2015. 83: p. 39-54.

[74] Software, S.D.I., DARS User Manual Version 2019.1. 2019.

[75] Cai, L., et al., Impact of exhaust gas recirculation on ignition delay times of gasoline fuel: An experimental and modeling study. Proceedings of the Combustion Institute, 2019. 37(1): p. 639-647.

[76] Blanquart, G., P. Pepiot-Desjardins, and H. Pitsch, Chemical mechanism for high temperature combustion of engine relevant fuels with emphasis on soot precursors. Combustion and Flame, 2009. 156(3): p. 588-607.

[77] Aubagnac-Karkar, D., Sectional soot modeling for Diesel RANS simulations. 2014, Ecole Centrale Paris.

REFERENCES CHAPTER 4

[1] Gosman AD. Developments in industrial computational fluid dynamics. Chem. Eng. Res. Des., 76(A2): 153-161,1998. https://doi.org/10.1205/026387698524721

[2] Casey M, Lang E, Mack R, Schlegel R, Wehrli M. Applications of computational fluid dynamics for process engineering at Sulzer. Speedup J., 12(1): 43-51,1988

[3] Kusche H. Computational Fluid Dynamics of Dispersed Two-Phase Flows at High Phase Fractions. PhD Thesis, 2002. Imperial College of Science, Technology & Medicine

[4] Liu, Z., Feng, Y., Lei, G., Li, Y. "Thermal physical process in a liquid oxygen tank under different sloshing excitations". Int. Commun. Heat Mass. 117:104771. 2020. https://doi.org/10.1016/j.icheatmasstransfer.2020.104771

[5] Martinez-Carrascal J, González-Gutiérrez LM, "Experimental study of the liquid damping effects on a SDOF vertical sloshing tank". J. Fluid Struct. 100:103172. 2021. https://doi.org/10.1016/j.jfluidstructs.2020.103172

[6] Grossi E, Shabana A. "ANCF analysis of the crude oil sloshing in railroad vehicle systems". J. Sound Vib. 433:493-516. 2018. https://doi.org/10.1016/j.jsv.2018.06.035

[7] Fontanesi S, Cicalese G, De Pasquale G. "A methodology for the reduction of numerical diffusion in sloshing analyses through automated mesh adaptation". Energy Procedia. 81:856-865. 2015. https://doi.org/10.1016/j.egypro.2015.12.096

[8] Li Q, Dong F, Li K. "An interface-sharpening method with adaptive mesh refinement for volume-of-fluid simulations of two-phase compressible flows". Comput. Fluids. 210:104648. 2020. https://doi.org/10.1016/j.compfluid.2020.104648

[9] Akyildiz H, Unal E. "Experimental investigation of pressure distribution on a rectangular tank due to the liquid sloshing". Ocean Eng. 32(11-12):1503-1516. 2005. https://doi.org/10.1016/j.oceaneng.2004.11.006

Ringraziamenti

Sono passati quasi venti anni da quando mi sono laureato in Ingegneria Meccanica nel 2003 presso l' Università di Catania e fortunatamente ho avuto la possibilità, fin da subito, di fare ricerca applicata come 'motorista' presso la Direzione Motopropulsori di Ferrari GT.

Nel corso degli anni ho avuto il privilegio di conoscere tante persone di diversa estrazione ed esperienza con cui ho condiviso tante sfide tecniche e grazie alle quali ho imparato tanto. A loro, e sono davvero tanti, che hanno così arricchito il mio bagaglio tecnico ed umano vanno sicuramente i miei ringraziamenti.

Sono cresciuto nel gruppo di Simulazioni e Know How MTPR fino a diventarne il Responsabile ormai da circa 10 anni. Un sentito ringraziamento va ai miei diversi Responsabili che nel corso della mia carriera hanno creduto in me, mi hanno formato e sostenuto fino al raggiungimento di importanti traguardi.

Un sentito ringraziamento a tutto il gruppo di Simulazioni e Know How che ho ancora il privilegio di guidare. Grazie per affrontare le sfide con competenza, passione e dedizione. Senza di Voi, molti dei risultati di queste ricerche su cui avete contributo in modo rilevante non sarebbero stati raggiunti.

Nel mondo delle simulazioni non bisogna avere paura di affrontare temi molto complessi su cui inizialmente ci può essere tanto scetticismo o pressione sui risultati, spesso i maggiori critici non hanno mai fatto un calcolo e quindi non hanno idea della fatica e del duro lavoro che sta dietro alla costruzione di una metodologia di calcolo robusta. A coloro che sostengono in modo deciso lo sviluppo delle simulazioni, ne comprendono sia il potenziale che i limiti e valorizzano l'impegno ed il lavoro di ricerca vanno i miei più sentiti ringraziamenti.

Un grosso ringraziamento va agli Accademici delle varie Università italiane ed estere con cui ho l'onore di collaborare e molti dei quali sono diventati degli amici. Grazie mille per il supporto che abbiamo ricevuto in questi anni. Tra questi, con piacere, ringrazio molto l'amico e Prof. Stefano Fontanesi che mi ha dato la possibilità di rimettermi a studiare in 'modo serio' durante questo dottorato. Grazie Stefano anche per tutti i temi di ricerca e le metodologie che ci hai aiutato a sviluppare in tutti questi anni insieme al tuo competente gruppo.

Last but not the least, un Ringraziamento Speciale a mia moglie Daniela per la pazienza e la serenità che mi trasmette anche quando sono particolarmente stressato e stressante.. ed ai nostri bimbi Alice e Giulio che con la loro gioia e curiosità riescono sempre a farmi staccare e concentrarmi su altre cose decisamente importanti!